In Silico Voltage-Sensitive Dye Imaging: A Model-Based Approach for Bridging Scales of Cortical Activity

Thèse N° 9848

Taylor Howard NEWTON

2019

EPFL
ÉCOLE POLYTECHNIQUE
FÉDÉRALE DE LAUSANNE

"If you always do what interests you,
at least one person is pleased."

— Katharine Hepburn

To Clio, Quinlan, Silas, and Grace, in no particular order.

Acknowledgements

Acknowledgements

Abstract

An understanding of how microscale voltage fluctuations interact to shape mesoscale cortical information processing is lacking. Voltage-sensitive dye imaging (VSDI) is a powerful technique for interrogating membrane potential dynamics in assemblies of cortical neurons, but with effective resolution limits that can confound interpretation. To address this limitation, we developed an *in silico* model of VSDI in a detailed digital reconstruction of rodent neocortical microcircuitry. Using this model, we clarify and extend previous experimental findings regarding the cellular origins and spatiotemporal dynamics of VSDI signals. Furthermore, we test the capacity of VSD image sequences to discriminate between afferent thalamic inputs at various spatial locations to estimate a lower bound on the functional resolution of VSDI. In addition, we explore experimentally inaccessible circuit properties to show that during periods of spontaneous activity, membrane potential fluctuations are anticorrelated with population firing rates. This relationship is dependent on recurrent connectivity, which we demonstrate by manipulating network connections. Finally, we investigate how the reciprocity between population spiking and membrane potential is affected by long-range, extrinsic synaptic input by adding artificial excitatory synapses to a subpopulation of layer 5 neurons. Based on our findings, we suggest that the lag time of peak anticorrelation between the VSD signal and population firing rate reflects the degree of perturbing external influence on the local microcircuitry. Our approach reveals that VSDI is a richer source of information than previously appreciated and underscores the power of a bottom-up computational approach for relating scales of cortical processing.

Résumé

Expliquer le traitement de l'information à l'échelle du cortex à partir de la dynamique des potentiels d'actions à l'échelle des neurones reste un problème ouvert. Dans ce contexte, l'imagerie par colorant sensible au potentiel (VSDI) est un outil pertinent pour étudier la dynamique des potentiels électrochimiques de membrane à l'échelle de population de neurones. Cependant, ces techniques présentent des limites effectives de résolution rendant leurs résultats difficiles à interpréter. Pour outrepasser ces limitations, nous avons développé un modèle *in silico* de VSDI prenant place dans une reconstruction numérique détaillée de microcircuits néo-corticaux de rongeurs. En nous aidant de ce modèle, nous proposons une ré-interprétation des origines cellulaires des signaux VSDI et de leurs dynamiques spatio-temporelles. De plus, notre modèle nous permet de proposer une limite inférieure de réso-lution spatiale utile, obtenue en testant la capacité de séquence d'images VSD à discriminer entre des entrées thalamiques afférentes provenant de différents points de l'espace. Au-delà de ce problème d'interprétation, l'usage d'un modèle *in silico* nous permet d'explorer des propriétés difficilement inaccessibles par l'expérience. Par exemple, nous montrons que pen-dant les périodes d'activité spontanée, les fluctuations des potentiels membranaires sont corrélées négativement avec le taux d'activation des neurones. Cette anticorrélation dépend de la quantité de récurrence présente dans le réseau, ce que nous montrons en manipu-lant les connexions de façons choisies. Dans une dernière partie, nous étudions comment la relation directe entre le taux d'activité d'une population de neurones et le potentiel de membrane des neurones la composant est modifiée par la présence de signaux provenant de synapse de neurones externes à la population étudiée. Pour ce faire, des synapses exci-tatrices sont ajoutées artificiellement dans une sous-population de neurones de la couche V. Nos résultats montrent que le décalage temporel entre le signal VSD et l'activation de la population menant à l'anticorrélation la plus forte reflète le degré de perturbation induit par ces synapses extérieures. Notre étude prise dans son ensemble montre que la VSDI est une source d'information plus riche et pertinente que ce qui était accepté auparavant, de plus, notre étude souligne la puissance des simulations basées sur une approche biologique réductionniste pour comprendre les dynamiques prenantes place à l'échelle du néocortex.

Contents

Contents

List of Figures

List of Tables

1 Introduction

1.1 Motivation

Modern neuroscience strives to elucidate the principles that underlie the structure and function of the brain. A complete understanding of how the brain encodes and interprets sensory inputs, and transforms these signals into motor outputs (and also non-motor percepts) would revolutionize modern medicine, and provide deep insights into the foundational underpinnings of human and non-human animal behavior. The neocortex, a thin sheet of intricately folded neural tissue, is the newest brain structure in terms of evolutionary history (Rakic, 2009), and is implicated in a wide variety of processes, including sensory perception (Petersen and Crochet, 2013), motor planning and control (Li et al., 2015), learning and memory (Rioult-Pedotti et al., 2000), sleep (Sirota et al., 2003), attention (Sacchet et al., 2015), and executive function (Teffer and Semendeferi, 2012). Given its positioning as the outermost layer of the brain, and its significance for human behavior, the neocortex is a natural target for scientific inquiry. However, the organization of an adult human brain is prohibitively complex, with ~86 billion neurons (Azevedo et al., 2009), and on the order of 100-200 trillion synapses (Nguyen, 2010), all contained within a ~1200 cm^3 volume of tissue (Allen et al., 2002). The hurdles to understanding are not simply numerical, but also structural, as the brain is arranged into hierarchically organized, interrelated modules that span multiple orders of magnitude in time and space. At one end of the spatiotemporal spectrum are processes such as activity-dependent gene transcription (West and Greenberg, 2011), or microsecond "flicker" dynamics in ion channels (Schroeder, 2015). At the other extreme, functionally defined systems such as the default mode network, recruit multiple cortical regions, and are implicated in pathologies such as Alzheimer's disease that develop over a lifetime (Greicius et al., 2004). The bewildering interdependent network of genetic and epigenetic influences, signaling cascades, neural circuitry, and environmental inputs has confounded our best attempts at producing a holistic picture of how the brain operates. Indeed, it may be the case that, given the selective pressures under which the species evolved, humans are biologically incapable of reasoning fluidly about a system with so many multiscale nonlinear interactions. Alternatively, although a microprocessor presents with a hierarchical, complex structure, humans are quite capable

of understanding its operation using a scale-dependent, nested set of organizing rules (Jonas and Kording, 2017). Is the brain's complexity fundamentally irreducible, or is the field of neuroscience missing relatively tractable principles of organization? What level of detail and description is necessary for a meaningful understanding of the brain? While these questions have largely resisted classical experimental techniques to date, a complementary, simulation-based paradigm is emerging, fueled by advances in computing (Kambatla et al., 2014, Koomey et al., 2011, Muir et al., 2016, Olivier et al., 2016).

Simulations are comparatively low cost, high-throughput, and easily modified, permitting a great volume of experiments whose laboratory analogs would be challenging or impossible. However, the *key* advantage of (biophysical) simulation lies in its ability to bridge spatiotemporal scales, integrating over low-level details to provide a bottom-up picture of emergent phenomena (Gerstner et al., 2012). Provided access to high-quality laboratory data for constraining detailed biophysical models, and state-of-the art computational resources, we can imagine a possible approach to the questions above. The Blue Brain Project (BBP), launched in 2005 by the Ecole Polytechnique Fédérale de Lausanne's Brain Mind Institute (BMI), is just such an example. With the goal of reconstructing and simulating a biophysically detailed column of rat neocortical microcircuitry (hereafter referred to as the NMC model, or NMC) and ultimately the entire brain, the BBP aims to elucidate the mechanisms of neural computation, and establish a common framework for model building and data curation (Markram, 2006). However, the utility of a simulation is limited by the quality of data and assumptions that constrain it. Indeed, it has been shown that multilayer recurrent neural networks are capable of approximating any discrete-time or continuous-time dynamical system (Doya, 1993). This evinces the need for rigorous ties to experimental data, lest we are misled by success at replicating some biological effect or computation. Importantly, a guiding philosophical principle of the BBP is commitment to constraint by empirical data wherever possible. Thus, model parameters are not tuned to match simulation outputs to observations; rather, the reconstruction process is constrained using the best available data, and missing datapoints are inferred algorithmically with parsimonious assumptions (Reimann et al., 2015, Markram et al., 2015). In light of its scale, level of detail, and commitment to empirical data, the NMC model furnishes a unique opportunity to design simulations that interrogate the relationship between micro- and macroscale signals in cortex. We reasoned that to leverage this capacity, we could recreate a recording or imaging modality that summarizes population level activity through the aggregation of many sub-processes.

Voltage-sensitive dyes (VSD) are a class of extrinsic fluorescent probes that bind to cell membranes and exhibit shifts in their absorption or emission spectra as a function of transmembrane voltage (V_m) with excellent linearity in a range of $\pm$ 300 mV (Lippert et al., 2007, Ross et al., 1977, Grinvald and Hildesheim, 2004, Chemla and Chavane, 2010b, Ferezou et al., 2009, Lustig et al., 2013, Grinvald et al., 1999). Unlike other mesoscale [1] imaging modalities, which generally suffer from space-time tradeoffs in resolution, voltage-sensitive dye imaging

---

[1]The terminology "mesoscale" is used to designate an intermediate spatial scale situated between the micro- and macroscale, characterized by interconnected groups of tens to hundreds of thousands of neurons.

(VSDI) is capable of producing images reflecting subthreshold activity spanning the entire rodent neocortical surface (on the order of several cm^2), with good resolution in time (<1 μs) and space (<50 μm)(Chemla and Chavane, 2010b, Ferezou et al., 2006, Grinvald and Hildesheim, 2004, Shoham et al., 1999). However, the interpretation of VSDI is confounded by the fact that the superposed activity of many neurites is reflected in each image pixel. Indeed, a common concern is identifying which attributes of neural anatomy and physiology (e.g. layer, cell-type, dendrites vs. axons, pre- vs. postsynaptic activity) are the primary drivers of VSDI measurements (Civillico and Contreras, 2006, Ferezou et al., 2006, Lippert et al., 2007, Petersen et al., 2003a). Also, uneven dye penetration and blurring due to the absorption and scattering of photons in tissue, further complicate the interpretation of VSDI signals (Chemla and Chavane, 2010a, Grinvald and Hildesheim, 2004, Grinvald and Petersen, 2015). The inverse problem of inferring the relative importance of many inputs from a highly multiplexed output poses a challenge, but could be addressed given a model of VSDI with sufficient detail and biophysical fidelity. Thus, as a powerful mesoscale imaging modality with uncertain cellular origins, VSDI was a natural candidate for a simulation-based study, the results of which constitute this thesis. To build a biophysically plausible model of VSDI, we performed simulations of the NMC to obtain V$_m$ recordings of neural compartments under various experimental conditions, which we used in conjunction with Monte Carlo simulations of photon-tissue interactions and a physical model of tandem-lens microscope optics. We leveraged our model to bridge spatiotemporal scales, generating new insights into the emergent dynamics of VSDI signals as a function of cellular activity. The work presented here was dictated by the following core set of objectives:

1. Implementation of a biophysically detailed, bottom-up model of VSDI with the BBP's NMC model at its foundation (*in silico* VSDI).

2. Validation of mesoscale activity in the NMC using *in silico* VSDI through replication of *in vivo* findings.

3. Extension and refinement of current knowledge regarding the origin and interpretation of VSDI signals.

4. Discovery of novel network-level mechanisms implicated in cortical information processing.

1.2 Thesis Organization

This document is organized as follows:

- **Chapter 1 (Introduction)** A description of the high-level motivations for this project, enumeration of its objectives, and a brief survey of the literature with attention to the history of VSDI and previous attempts to model VSDI signals.

- **Chapter 2 (Modeling Part I: The Neocortical Microcircuit)** A technical overview of the

NMC model. Topics addressed pertaining to microcircuit reconstruction workflow include: single-cell anatomy, circuit composition and connectivity, cellular and synaptic physiology, and thalamocortical innervation. Also discussed is the emergence of a calcium-dependent network regime map, and the reproduction of *in vivo* experiments.

- **Chapter 3 (Modeling Part II: *in silico* VSDI)** A detailed account of the *in silico* VSDI signal calculation pipeline. We begin by enumerating underlying assumptions, and continue with a description of the "online" procedure for calculating the fluorescence signal. Roughly, this covers determination of the raw signal, voxelization of the tissue volume, formation of images, and post-processing. Also discussed are "offline" procedures that produce ancillary quantities required for fluorescence calculations, namely attenuation curves accounting for the physics of dye penetration and light transport, and a model of the optical microscope system.

- **Chapter 4 (Results)** A discussion of the insights generated by *in silico* VSDI experiments. We begin with results that confirm the high-level spatiotemporal dynamics of evoked responses, and increase confidence in the validity of the NMC as a model for mesoscale information processing. Next, we extend and refine current knowledge regarding the origin and interpretation of VSDI signals through a laminar and cell type-wise dissection of VSDI, and an analysis of sub- versus suprathreshold signal contributions. Also, we consider the classification performance of imaging pixels in a two-point discrimination task designed to assess the "functional" spatial resolution of VSDI. Finally, we present novel insights into the relationship between subthreshold V_m and population firing rates, with implications for a more nuanced interpretation of VSDI signals. In this context, we also examine how long-range inputs to the NMC could modulate synaptic conductances.

- **Chapter 5 (Concluding Remarks)** Extended commentary on aspects of the findings presented in the preceding chapter, with special attention paid to discrepancies between our results and those reported in literature, limitations of our model, and outlook for the future.

1.3 Review of VSDI and Related Techniques: An Historical Perspective

The spike-centric paradigm for neural information processing holds that "inputs", constituted by subthreshold V_m changes (largely in the form of postsynaptic potentials), and "outputs" in the form of action potentials (APs) elicited by these inputs, are the main currency of cortical signaling (Grinvald and Hildesheim, 2004). Therefore, a complete understanding of cortical function requires a technique that is: 1) able to simultaneously record from large numbers of neurons, 2) sensitive enough to resolve subthreshold potentials, and 3) fast enough to record spiking activity. VSDI stands out among mesoscale imaging modalities for its capacity to generate highly resolved image stacks (<50 μm in space, microsenconds in time) over an

impressive spatial extent (several cm^2) (Chemla and Chavane, 2010b, Ferezou et al., 2009, Grinvald and Hildesheim, 2004, Shoham et al., 1999). By comparison, the local field potential (LFP), which reflects a summation of extracellular transmembrane ionic currents, is influenced by a region with a radius of at least 250 μm (Xing et al., 2009), and possibly upwards of several millimeters (Kajikawa and Schroeder, 2011).

The development of VSDI technology began with optical recordings in the squid giant axon, at which time hundreds of candidate fluorescent probes were tested for potentiometric viability (Tasaki et al., 1968, Davila et al., 1973, Cohen et al., 1974). These experiments were followed by simultaneous recordings of multiple neurons in invertebrate ganglia using photodiode arrays (Grinvald et al., 1977), and population studies in mammalian hippocampal slices (Grinvald et al., 1982b) and salamander olfactory bulb (Orbach and Cohen, 1983). A natural step was the extension of the technique to *in vivo* measurements in mammalian cortex. However, there were significant hurdles to the adoption of VSDI for *in vivo* studies in cats and rodents, namely, corruption of the signal by a strong heartbeat- and respiration-related puslation artifact (up to ten times the optical signal (Shoham et al., 1999)), and limited penetration of the dye and excitation light into deeper layers (Grinvald and Hildesheim, 2004, Grinvald and Petersen, 2015). New classes of dyes, such as RH-414 (Grinvald et al., 1982a, Orbach et al., 1985), and later RH704 and RH795 (Grinvald et al., 1994, 1986, Kleinfeld and Delaney, 1996) overcame penetration issues by more effectively staining cortical tissue and improving signal-to-noise ratio (SNR), while pulsation artifacts were addressed by subtracting phase-aligned blank trials (Grinvald et al., 1984, Grinvald and Hildesheim, 2004, Petersen et al., 2003a). Subsequently, a new generation of blue VSDs (RH1691/2) was developed with absorption spectra away from the peak absorption wavelength of hemoglobin (Shoham et al., 1999), further mitigating the influence of heartbeat and respiration artifacts (Lippert et al., 2007, Civillico and Contreras, 2005), and even obviating the need for artifact correction in certain cases (Ferezou et al., 2006, Lippert et al., 2007, McVea et al., 2012, Mohajerani et al., 2010, 2013). Also, these dyes featured improved SNR, with the benefit of reduced need for multiple trial averages, thereby limiting exposure time and consequently photobleaching (Shoham et al., 1999). These advances were complemented by parallel progress in imaging technology, with the development of fast, high-resolution charge-coupled device (CCD) and complementary metal-oxide-semiconductor (CMOS) cameras, permitting image acquisition on the millisecond timescale (Shoham et al., 1999, Petersen et al., 2003a,b, Ferezou et al., 2006, 2007).

In previous decades, significant progress was made in mapping the functional architecture of the brain using intrinsic optical imaging (IOI), a modality based on activity-dependent changes in the intrinsic absorption and/or fluorescence properties of brain tissue (chiefly concentration of oxy- and deoxy-hemoglobin) (Grinvald et al., 1999). Studies combining IOI with cytochrome oxidase staining revealed the interdependent organization of ocular dominance columns, color preference blobs, and orientation selective "pinwheel" structures in the visual system (Bartfeld and Grinvald, 1992, Blasdel, 1992b,a, Frostig et al., 1990, Ts'o et al., 1990). However, IOI is limited by a slow time constant (on the order of seconds (Grin-

vald et al., 1986, 2016)), rendering it ill-suited for capturing temporal changes in ongoing activity. To this end, VSDI has added a dynamic component to the understanding of neural assemblies. Indeed, VSDI-based studies have clarified the role of feedforward thalamic inputs versus intracortical recurrent activity in shaping orientation selectivity (Sharon and Grinvald, 2002), and shown how orientation selective responses spread over the cortex as a function of stimulus shape and size (Chavane et al., 2011). In addition, VSDI has been used to elucidate the neuronal mechanisms underlying perceptual phenomena such as the line-motion (LM) illusion (Jancke et al., 2004), and to explain the observed variability of evoked responses in terms of ongoing spontaneous activity (Arieli et al., 1996). An especially salient observation made possible by mesoscale VSDI is the presence of repeating spatiotemporal motifs during spontaneous cortical activity. Multiple studies have shown that spontaneous depolarization tends to cycle through stereotyped spatiotemporal patterns closely resembling those evoked both by optogenetic activation and peripheral stimulation (Chan et al., 2015, McVea et al., 2012, Mohajerani et al., 2013, Tsodyks et al., 1999). VSDI has also been widely applied to the study of somatosensory computations in barrel cortex, where the somatotopic organization and spatiotemporal scale of activity is well suited to the technique. Such studies have produced important findings regarding the regulation of response dynamics by ongoing spontaneous activity (Petersen et al., 2003b), cortical state (Civillico and Contreras, 2012), behavior (Ferezou et al., 2006, 2007, Kyriakatos et al., 2017), and stimulus strength (Petersen et al., 2003a). Broadly put, VSDI has enabled the field to move beyond the static picture provided by staining and IOI, adding a dynamic dimension to the understanding of mesoscale cortical organization. Given its historical importance and continued relevance as a tool for studying the brain, VSDI stands to benefit from a detailed model capable of bridging its underlying cellular origins with the high-level signals measured in experiments.

1.4 Previous Models of Mesoscale VSDI

Previous efforts to formulate computational models of mesoscale imaging techniques exist and deserve mention here, with special attention paid to models of VSDI. Markounikau et al. (2010) describe a two layer neural field model of VSDI comprising an inhibitory and excitatory population coupled via a set of nonlinear integro-differential equations. The model was trained and tested on a visually evoked dataset recorded in V1, and was shown to generalize well to unseen stimuli. In addition, by replicating the LM illusion with only feedforward afferent input, the results raise the intriguing possibility that feedback from higher cortical areas is not necessary to produce the illusion of motion (Markounikau et al., 2010). However, the power of this conclusion is limited by the fact that LM illusion data was included in the training set. While a useful proof-of-concept for the notion that isolated local networks could in principle explain complex phenomena, the specter of overfitting reduces confidence that the model explains the observations. Further, even if these simulations successfully reproduced the VSDI correlates of an unseen (i.e. test set) perceptual illusion, it would be unclear whether other similarly idealized permutations of the model could also succeed. This

example underscores the disadvantages of high-level abstraction and parameter optimization in models of complex biological systems.

In another two layer construction, Sit and Miikkulainen (2007) propose a model of retina and V1 using laterally interconnected synergetically self-organizing maps (LISSOM), in which local receptive fields of retinal units feedforward onto laterally connected units in V1. They extended this framework to construct a model of VSDI signals using a weighted sum of presynaptic activity, with which they reproduced the orientation tuning curve and time course of VSDI data obtained in cat V2 (Sit and Miikkulainen, 2007). LISSOM has the advantage of being a purely unsupervised technique, averting the need for explicit parameter tuning. During training, each neuron applies a nonlinear transformation to the weighted sum of its afferent inputs, and propagates the result via reciprocal lateral interactions to its postsynaptic targets (Sirosh and Miikkulainen, 1994). After activity has settled, connection weights are updated according to a Hebbian plasticity rule (Sirosh and Miikkulainen, 1994). Sit and Miikkulainen (2007) extend the basic model by introducing a distance-dependent time delay to account for signal propagation between neural units. Although parsimonious in its assumptions and surprisingly predictive, such a model cannot be used to explore the consequences of more nuanced biological features, such as sub- and supralinear dendritic summation (Tran-Van-Minh et al., 2015), or calcium spikes in distal dendrites (Chua and Morrison, 2016). It is an open question as to whether such details are mere perturbations to, or important determinants of, dynamics at the mesoscale. A sufficiently detailed model would have the power to distinguish between these possibilities.

In another study, Zerlaut et al. (2018) apply a mean-field approach to model a network of adaptive exponential (AdEx) integrate-and-fire neurons, comprising regular-spiking (RS) excitatory and fast-spiking (FS) inhibitory populations. The mean-field master equation was constructed using a transfer function that maps stationary presynaptic firing rates to a stationary output rate (Zerlaut et al., 2018). This transfer function is semi-analytical in that it is expressed analytically, but includes terms that must be optimized based on the results of single-cell simulations. Impressively, their model not only predicted VSDI responses, but could also be used to infer biophysical parameters from spatiotemporal patterns in VSDI observations, specifically axonal conduction velocity and the spatial extent of lateral connectivity for both RS and FS populations (Zerlaut et al., 2018).

As stated previously, to better understand how and when reduced models are most informative, we assert the need for a *detailed* simulation of VSDI to ascertain how much information is lost through simplification. While our work is an unambiguous step in this direction, it is not the first example of such an attempt. Chemla and Chavane (2010a) also employ a bottom-up approach in a cortical microcircuit populated by 180 morphologically detailed neural reconstructions from Yale's NEURON Model DB database comprising four cell types (L2 small PCs, L4 spiny stellate cells, L5 PCs, and smooth stellate cells in all layers). Single neuron parameters were optimized to replicate RS and FS behavior, while network architecture, synaptic interactions, afferent thalamic input, background activity, and external intracortical

inputs were informed by data in the literature. Using this model, they decomposed the VSDI signal into its cellular constituents, confirming prior findings that excitatory dendritic sources in the superficial layers constitute most of the signal, but also calling attention to non-trivial contributions by inhibitory compartments and deeper layers (Chemla and Chavane, 2010a). Naturally, we were inspired by this work, and sought to expand upon it by exploiting the unprecedented scale and biological intricacy of the NMC model.

Finally, we highlight a computational model of the local field potential (LFP), which measures the extracellular potential induced by local ionic transmembrane currents, and like VSDI, reflects the joint activity of many neuronal compartments. This model was implemented by Reimann et al. (2013) in the same reconstruction of neocortical microcircuitry utilized in this work (the NMC). They found that LFP simulations using membranes with active conductances significantly outperformed those with only passive membranes at reproducing experimental findings in rat barrel cortex (Reimann et al., 2013). Their study sets a precedent for the use of the NMC to recreate mesoscale imaging techniques and produce insights that bridge spatial and temporal scales.

1.5   Statement of Relevance

This work aims to model VSDI signals with a level of detail and accuracy not previously possible, by capitalizing on an existing framework (the NMC), with the intent of: validating mesoscale network activity in the NMC, refining and extending state-of-the-art knowledge regarding the interpretation of VSDI, and contributing new insights to the field. As suggested by the preceding sketch of the history of mesoscale optical imaging in the brain, VSDI and related techniques have contributed importantly to an emerging picture of functional cortical organization. An understanding of the interplay between ongoing dynamics and external sensory inputs, the spatiotemporal structure of spontaneous activity, and functional connectivity between brain regions, owes much to the pioneering adoption of VSDs for *in vivo* imaging studies. Considering its seminal position in the canon of neuroscientific methods, VSDI merits a thorough evaluation of the origin and interpretation of the signals it generates. Such an understanding would serve to deepen and clarify existing knowledge, and suggest new avenues of inquiry for future research. Furthermore, a model sufficiently powerful to study VSDI by bridging cellular and network-level phenomena would also hold potential as a tool for new discoveries. The capacity to traverse levels of organization, and arbitrarily modify circuit structure and function to test hypotheses, would facilitate the observation of novel principles that would otherwise be impossible or difficult to detect. Last, a model of VSDI meeting the objectives enumerated above would reinforce the utility of simulation-based studies for imaging techniques generally. Future models of electroencephalography (EEG), calcium imaging, multielectrode arrays (MEA), magnetoencephalography (MEG), photoacoustic imaging, and functional magnetic resonance imaging (fMRI) have the potential to reveal unknown interdependencies and complementarities between different imaging modalities, and unlock profound, experimentally inaccessible insights into the dynamics of cortical processing.

2 Modeling Part I: The Neocortical Microcircuit

2.1 Reconstruction

2.1.1 Overview

In 2015, the BBP published the results of a ten year effort to build and simulate a biophysically detailed model of juvenile (P14) rat hindlimb somatosensory microcircuitry (the NMC model) (Markram et al., 2015): http://dx.doi.org/10.1016/j.cell.2015.09.029. The model comprises a connected network of ~31,000 neurons with 55 morphological types and 207 morpho-electrical types, arranged in a 0.29±0.01 mm^3 vertical column of tissue spanning cortical layers 1 through 6 (Fig. 2.1a). Connectivity in the network was determined algorithmically (see Section 2.1.3), and resulted in a total of ~37 million synapses distributed over~8 million connections. In addition, the model is furnished with thalamocortical innervation permitting the delivery of afferent stimuli. Simulating the model revealed an emergent spectrum of network regime states characterized by the presence or absence of regenerative activity. Moreover, simulations qualitatively reproduced the results of several *in vivo* experiments without the need for parameter tuning.

Contribution Statement: The following chapter summarizes material drawn from Markram et al. (2015). I contributed to this publication by analyzing the output of simulations run by Eilif B. Muller, and used the results to produce Figure 2.6 (Figures 18A1-4, and S19A-D in Markram et al. (2015)). I also assisted in writing the captions and text pertaining to those figures in the original manuscript.

2.1.2 Anatomy

Figure 2.2 illustrates our workflow for reconstruction. The process begins with *in vitro* whole-cell (WC) patch-clamp recordings performed in 300 μm thick cortical slices. Recorded cells were stained with biocytin and classified (n=2,052) into one of 55 morphological types (m-types) based on layer and anatomical characteristics of the axo-dendritic arborization. Among
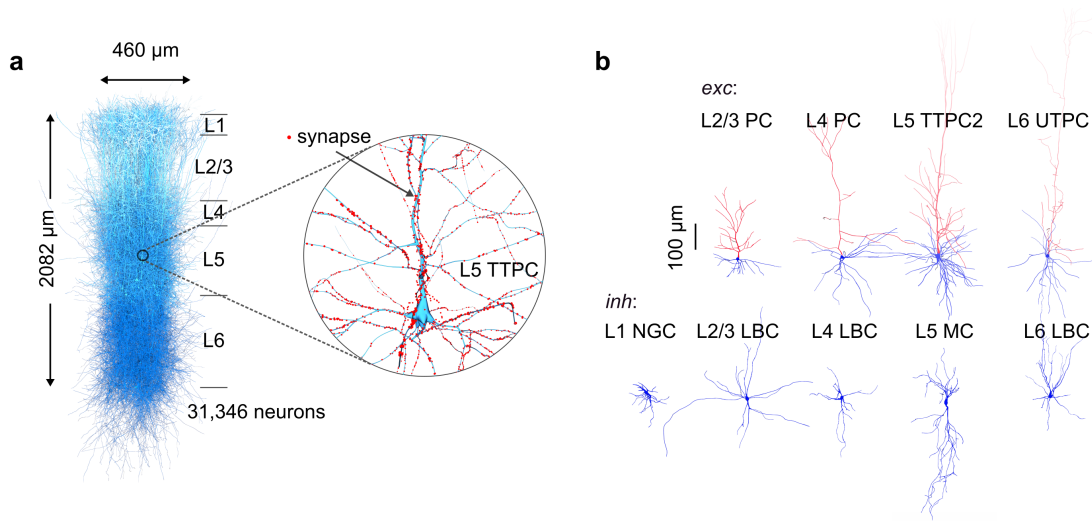
Figure 2.1 – **NMC Overview**

a, NMC reconstruction comprising 31,346 morphologically detailed neurons connected in a columnar unit. Inset: expanded view of two L5 PCs, with synapses highlighted in blue (UTPC -> TTPC) and green (TTPC -> UTPC). **b**, Exemplar excitatory (top) and inhibitory (bottom) cell types, vertically located according to their placement within their respective layers. Blue: axons. Red: dendrites.

labeled cells with an m-type classification, 1,009 were digitally reconstructed as 3D neural morphologies. The histological processing and slicing procedures tended to shrink tissue (increasing tortuosity) and truncate arborizations near the slice edges. Therefore reconstructions underwent repairs to correct for these artifacts: a digital "unraveling" to reduce toruosity, and a recovery process for arbors lost during slicing (Anwar et al., 2009). In order to populate the circuit with an adequate number of cells, reconstructions were cloned by injecting Gaussian-distributed noise into branch lengths and angles, preserving topological structure but generating morphologically distinct model neurons (Fig. 2.2a, 2.1b).

2.1.3 Placement and Connectivity

Circuit height, layer thicknesses, cell densities, excitatory/inhibitory (E/I) fractions, and m-type proportions per layer were determined experimentally. Measurements yielded an average cortical height of 2,082 $\pm$ 80 μm. Layer thicknesses and cell densities were established simultaneously by examining transitions in cell densities along the depth axis using an optical disector in NeuN-stained tissue sections. Staining for DAPI (all cells), NeuN (all neurons), and GABA (inhibitory neurons) provided estimates for the E/I fractions in each layer (overall: 87% to 13% E to I). M-type composition for each layer was inferred from the relative frequency of occurrence in the original sample of 2,052 neurons with m-type classifications (see Section 2.1.2). Horizontal dimensions in the circuit were imposed by placing cells in a cylindrical volume whose radius was incrementally expanded until dendritic saturation at the center achieved 95% of the asymptotic limit (r=210 μm). Finally, neurons were arranged
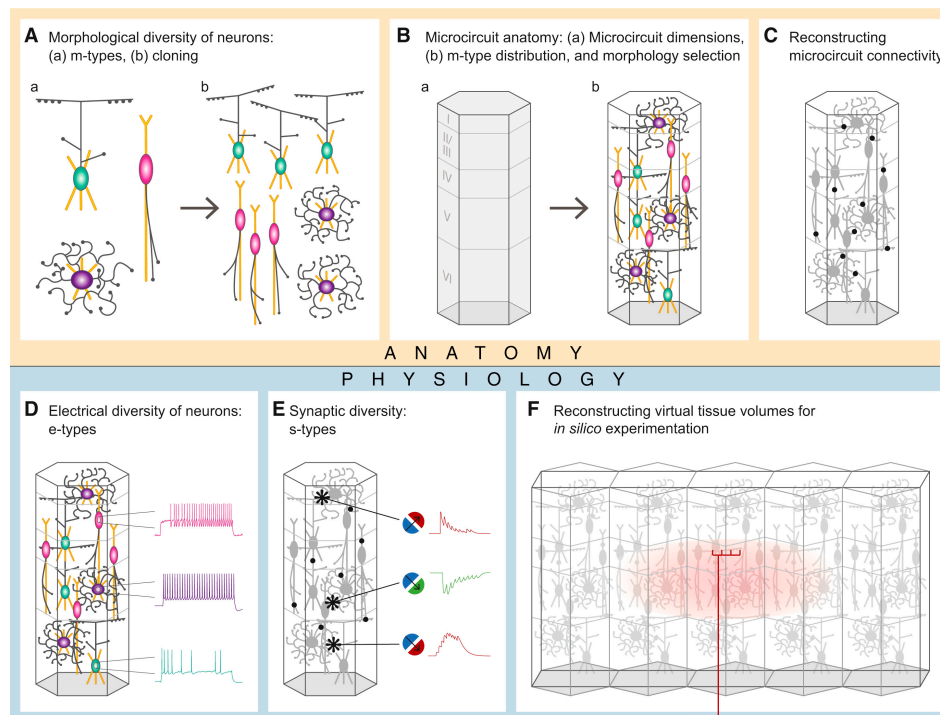
Figure 2.2 – **Workflow for Data-Driven Reconstruction of Neocortical Microcircuitry**

(A) Morphological diversity of neurons. (a) Identify the morphological diversity in the neocortical microcircuit (m-types). (b) Repair and then clone the various mtypes with statistical variations to enrich the number of exemplars. (B) Microcircuit anatomy. (a) Define the spatial dimensions of a unitary microcircuit. (b) Assemble individual neurons in 3D space according to the frequency of occurrence of each m-type per layer, selecting the appropriate m-type instance that satisfies laminar constraints on the axonal and dendritic distribution. (C) Reconstructing microcircuit connectivity. Derive the number and location of synaptic contacts formed between all neurons in the microcircuit, based on a series of synaptic connectivity rules. (D) Electrical diversity of neurons. Map and model the electrical types (e-types) of each m-type to account for the observed diversity of morpho-electrical subtypes (me-types). (E) Synaptic diversity of neurons. Map and model the diversity of synaptic types (s-types) observed between pre-post combinations of me-types, according to rules derived from synaptic physiology. (F) Reconstructing virtual tissue volumes. Apply the above strategy to reconstruct defined circuit volumes (microcircuits, slices, mesocircuits) for *in silico* experiments; insert synapses formed by thalamocortical fibers for stimulation experiments. *Figure 2.2 and corresponding caption from Markram et al. (2015), reprinted courtesy of Cell Press.*

into 310 narrow columnar clusters (minicolumns) within the larger microcircuit, where each cell's radial placement in the minicolumn was drawn from a zero-mean Gaussian distribution. These procedures yielded a tissue volume with biologically plausible distributions of neurons (Fig. 2.3; Fig. 2.2b), but no account of connectivity. To this end, network connectivity was reconstructed using an algorithm proposed by Reimann et al. (2015), in which viable synaptic connections are determined by "whittling away" the set of all possible synapses in a multi-stage pruning process (Fig. 2.2c). The algorithm proceeds as follows:

1. **Appositions** Potential synapse locations are identified by incidental "appositions", or locations where neural arbors happen to approach one another within a critical radius (<2.5 μm for excitatory synapses; <0.5 μm for inhibitory synapses). These locations are
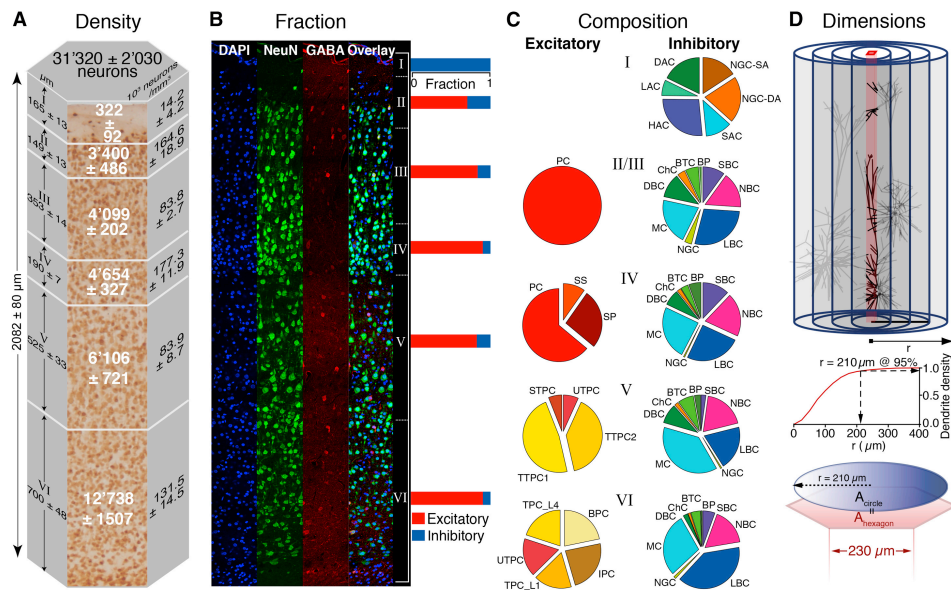
Figure 2.3 – **Neuron Densities and Composition and Microcircuit Dimensions**

(A) Neuron densities and numbers. Vertical thicknesses as determined by transitions in neuronal somata size and density in NeuN stained slices (six animals; mean ± SD). Neuron densities and numbers (six animals; mean ± SD). (B) Neuron fractions. Confocal block imaging of dual immunohistochemical labeling. DAPI labels all cells (blue). NeuN labels all neurons (green), GABA labels all GABAergic cells including glia (red), dual GABA and NeuN labels only GABAergic neurons (green). Bars to the right show fractions of excitatory (red) and inhibitory (blue) neurons in each layer. (C) m-type composition. Fractions of inhibitory (left) and excitatory (right) m-types per layer (n = 2052). (D) Dimensions. The horizontal dimension was defined as the smallest circle required to attain maximal dendritic volume at a central minicolumn (brown, top); cutoff radius, 95% of the plateau volume (r = 210 mm, middle). To allow tiling, the circle was transformed into a hexagon, preserving the area. *Figure 2.3 and corresponding caption from Markram et al. (2015), reprinted courtesy of Cell Press.*

2. **General Pruning** Step 1 yields an order of magnitude too many synapses in comparison to experimental data (Romand et al., 2011, Wang et al., 2002). Appositions are uniformly downsampled, thereby reducing their number, and truncating the right-hand tail of the distribution of appositions per connection.

3. **Multisynapse Pruning** Biological measurements indicate that neurons tend to form multisynapse connections (Markram et al., 1997, Deuchars et al., 1994, Frick et al., 2008, Wang et al., 2002). Therefore, pathways connected by too few appositions are removed, clipping the left-hand side of the distribution.

4. **Plasticity-Reserve Pruning** Finally, available evidence suggests that only a fraction of possible connections are active, with the remainder providing a synaptic reserve to accommodate plasticity-dependent rewiring (Chklovskii et al., 2004, Lamprecht and LeDoux, 2004, Le Bé and Markram, 2006). As such, a uniformly sampled fraction of multisynaptic connections are removed to produce the final distribution of synapses per connection.

a consequence of the arrangement of cells within the circuit as described above.
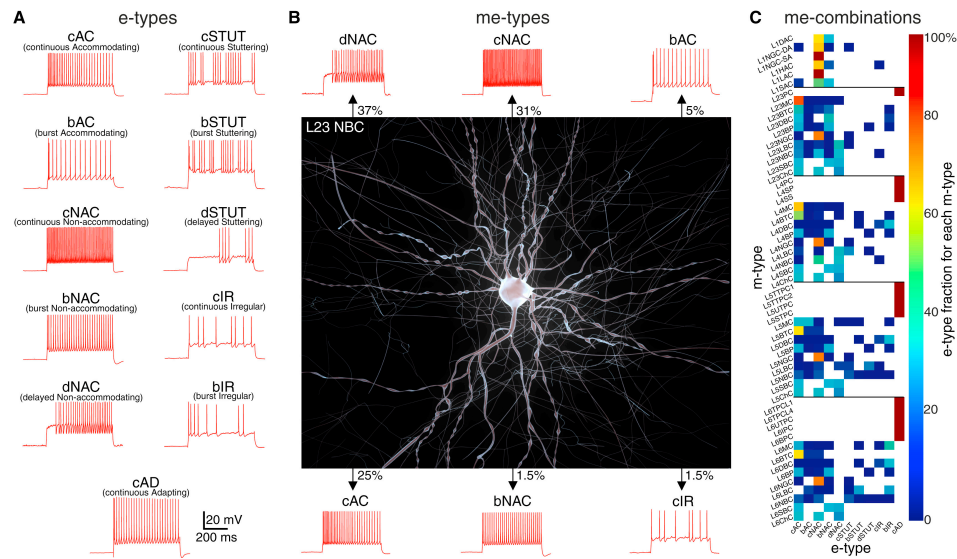
Figure 2.4 – **Table of Morpho-Electrical Neuron Types**

(A) e-types. Diverse firing patterns in response to depolarizing step current injections in neocortical neurons. c, continuous; d, delayed; b, bursting. AC, accommodating; NAC, non-accommodating; STUT, stuttering, IR, irregular; AD, adapting. (B) An exemplar neuron (L23NBC) with a diversity of e-types. Percentages indicate the relative frequency of e-type occurrence. (C) Fractions of e-types (11 e-types) recorded experimentally in each of the 55 m-types, making up 207 me-types. Solid lines indicate layer boundaries. *Figure 2.4 and corresponding caption from Markram et al. (2015), reprinted courtesy of Cell Press.*

2.1.4   Physiology

Single-Cell Physiology

Data from the electrophysiological recordings referred to in Section 2.1.2 were used to identify 11 electrical types (e-types) based on criteria proposed by the Petilla convention (Ascoli et al., 2008) (Fig. 2.2d; Fig. 2.4a). To map m-types to e-types, reconstructed morphologies were imported into the NEURON simulation environment (Hines and Carnevale, 1997), and a multiobjective optimization procedure (Druckmann et al., 2007) was used to attempt a fit of each individual morphology (already classified by m-type) to each e-type as a function of the spatial distribution of ion channel conductance densities over the surface of each cell. Thirteen classes of ion channels modeled according to the Hodgkin-Huxley formalism were drawn upon during optimization. The m-e combinations that yielded successful outcomes (n=207) are referred to as me-types (Fig. 2.4b,c).

Synaptic Physiology

Synaptic transmission at each synapse location identified in Section 2.1.3 was modeled with a stochastic, two state Markov process implementation of the Tsodyks-Markram dynamic synapse model (Tsodyks and Markram, 1997). Excitatory (AMPA, NMDA) and inhibitory (GABA$_A$, GABA$_B$) receptor kinetics (rise and decay time constants and reversal potentials) were parametrized using values taken from the literature, while synaptic conductances were opti-

mized to match experimentally measured postsynaptic potential (PSP) amplitudes. Synapses were classified broadly into one of three types (s-types): facilitating, depressing, or pseudo-linear. However, a difficulty lay in knowing which s-type to assign to each me-type-to-me-type pathway, given the sparsity of experimental data, and the overwhelming number of biologically plausible combinations (27,625). Thus, a short list of empirical rules for inferring s-type assignment was derived from prior publications, and applied to those connection pathways not already characterized in the literature (Fig. 2.2e). Finally, the spontaneous release of neurotransmitter was modeled as a stochastic miniature postsynaptic current (PSC). These events were implemented as independent Poisson processes with rates λ_{spont} derived from experimental measurements (Ling and Benardo, 1999, Simkus and Stricker, 2002).

2.1.5 Thalamocortical Innervation

Virtual thalamocortical (TC) innervation was instantiated in the model to permit the delivery of afferent stimuli. A depth-dependent bouton density profile for the ventral posteromedial nucleus (VPM), supplied by Meyer et al. (2010), was used to constrain the distribution of afferent TC synapses. Briefly, neurite segments at each depth were randomly selected to receive TC synaptic innervation at a rate proportional to the empirical bouton density profile. These putative synapses were pruned according to step 3 of the algorithm described in Section 2.1.3 using a known mean value for synapses per TC connection in L4. To map virtual TC fibers to synapses, each of the 310 minicolumns in the microcircuit was assigned a unique afferent TC projection fiber, and each synapse was assigned a TC fiber's minicolumn with a probability dependent on the radial distance between the synapse and the center of that minicolumn. TC synaptic physiology was determined using dynamic synaptic parameters sampled from estimated distributions available in the literature (Amitai, 2001, Gil et al., 1999).

2.2 Network Regime

Simulations of spontaneous activity were conducted at various concentrations of extracellular calcium ($[\text{Ca}^{2+}]_o$) and tonic depolarization (expressed as a percentage of rheobase for each cell), uncovering a map of network regimes transitioning between non-regenerative (asynchronous) activity and regenerative (synchronous bursting) activity for evoked (via TC stimulation) and spontaneous activity (Fig. 2.5d). Changes in $[\text{Ca}^{2+}]_o$ were emulated by s-type-dependent modifications in synaptic release probability in accordance with Gupta et al. (2000), Rozov et al. (2001), Silver et al. (2003). At higher levels of $[\text{Ca}^{2+}]_o$ (2 mM) the circuit exhibited oscillatory bursts (~1 Hz) similar to those observed in *in vitro* experiments (Amzica et al., 2002, Jones and Keep, 1988). Neural activity desynchronized as $[\text{Ca}^{2+}]_o$ was lowered, with a sharp inflection point near 1.25 mM, approximately consistent with estimates of *in vivo* $[\text{Ca}^{2+}]_o$ for awake conditions (~ 0.9-1.1 mM (Amzica et al., 2002, Jones and Keep, 1988)). In addition, varying the level of tonic depolarization shifted the state of the network (Fig. 2.5c,d), with increasing levels of depolarization reducing the $[\text{Ca}^{2+}]_o$ threshold at which the network

transitioned between any two of the four regimes. It may be the case that in biological cortex, a similar tension exists between sensitivity to excitation and degree of correlation among neurons. Increasing the E/I ratio would tend to amplify overall activity, thereby augmenting the capacity of cortical tissue to encode information. However, beyond a certain threshold
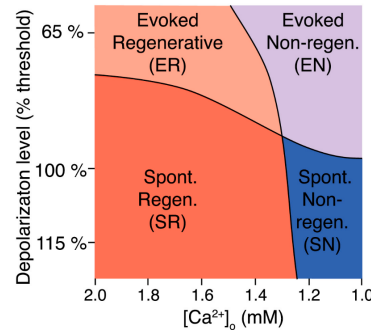
Figure 2.5 – **Regime Map**

Characterization of spontaneous and evoked activity under different levels of depolarization and $[Ca^{2+}]_o$. Schematic map showing the four activity regimes. Evoked regenerative, ER; spontaneous regenerative, SR; evoked non-regenerative, EN; spontaneous non-regenerative, SN. *Figure 2.5 and corresponding caption from Markram et al. (2015), reprinted courtesy of Cell Press.*

inhibition cannot keep pace with excitation, and the network would enter a regenerative state where cells are forced to fire in synchronous oscillatory bursts, increasing correlations, and therefore diminishing information encoding capacity (Beaman et al., 2017, Minces et al., 2017). Thus, the transition point between regenerative and non-regenerative activity ($[Ca^{2+}]_o$=1.25 mM, depol.=~100%) was used to approximate *in vivo* conditions in all simulations described in the following chapters of this thesis.

2.3   *in vivo* Reproductions

An effort was undertaken to reproduce the results of select *in vivo* studies using the NMC model as a test of its functional validity. Simulations were carried out at or near the inflection point between synchrony and asynchrony (see Section 2.2), with no ad hoc adjustments to model parameters. Four key results reported in the literature were targeted for replication:

1. Cell type-specific diversity of neuronal responses to single-whisker deflection (Reyes-Puerta et al., 2015).

2. Tight anticorrelation between excitatory and inhibitory postsynaptic currents (Beierlein et al., 2000, Okun and Lampl, 2008).

3. Temporally precise spike triplet motifs occurring with higher than chance probability during activated states (Luczak et al., 2007).

4. Specific proportions and response properties of neurons classified as either "soloists"

(uncorrelated with population activity) or "choristers" (correlated with population activity) (Okun et al., 2015).

We focus here on the third study above (Luczak et al., 2007), since: 1) it constitutes this author's principle contribution to the work of Markram et al. (2015), and 2) it sets a precedent for the use of the NMC model as a tool for the analysis of emergent population level cortical activity patterns. Sleep and quiet wakefulness are associated with cortical slow oscillations (~1 Hz) that alternate between periods of network silence ("down states"), and persistent spiking ("up states") (Luczak et al., 2007, Steriade et al., 1993b). Recording from a population of 50-200 L5 rodent somatosensory neural units using multisite microelectrodes, Luczak et al. (2007) show that individual neurons have a diversity of precise, stereotyped activity sequences that are initiated by up state onset. Noting that previous studies observed precisely repeated spike templates at the *population* level (Cossart et al., 2003, Mao et al., 2001, MacLean et al., 2005), they propose a simple explanation in terms of the stereotyped activity of individual neurons during up states. To this end, they undertake an analysis of spike triplets (previously described by Abeles and Gat (2001)), comparing spike time differences in the spike trains of trios of neurons.

Since the NMC model does not exhibit slow oscillatory behavior, we emulated up and down states by injecting each cell with cycles of alternating depolarizing and hyperpolarizing current. Following the approach of Luczak et al. (2007) as closely as possible, we randomly sampled L5 neurons (n=50) and generated all distinct combinations of three cells (trios). For each trio, we computed a collection of spike triplets, defined as the set of all pairs of interspike intervals (ISIs) $\{(t_3 - t_1, t_2 - t_1)_i\}$ (i indexes trio number) formed by selecting one spike from each spike train (see Fig. 2.6a1). We plotted these sets of spike triplets as a 2D count histogram, from which we extracted the "precisely repeating triplets", or those triplets occurring within ± 10 ms of the mode (Fig. 2.6a2). Correlating the ISIs of precisely repeating triplets with the time to first spike (up state onset latency) of the neurons in the associated trio, we observed that the neural latencies predicted the mode of the spike triplet patterns (Fig. 2.6a3). Finally, we considered the probability of observing a precisely repeating triplet structure as a function of time from up state onset. To ensure that results were not due to chance, we compared against two null hypotheses: 1) spike triplet probabilities such as those observed appear even under fully unstructured conditions (i.e., independent Poisson spiking), 2) higher spike triplet probabilities following up state onset appear merely as a result of increased firing rates (i.e., "common excitability"). In the first case, we randomly shuffled spikes in time, preserving spike numbers but destroying temporal structure. In the second, we randomly exchanged spikes between cells, preserving spike times and firing rates. Neither null hypothesis was able to account for the significant increase in precisely repeating triplet probabilities observed following up state onset (Fig. 2.6a4). The results of our analysis, and those described by Luczak et al. (2007), bolster credence in the proposition that repeating spike time templates observed at the population level are accounted for by the diverse but stereotyped, temporally precise responses of individual cells to up state initiation. Furthermore, the presence of such temporally precise sequential structures in the NMC suggests that they are a consequence of

local network dynamics, and also fosters confidence in the use of our microcircuit as a model of cortical physiology.

Encouraged by our success, we explored the further possibility that shifting the network away from its critical *in vivo*-like operating point (see setion 2.2) might suppress the emergence of precisely repeating spike triplets. To this end, we performed additional simulations under low $[Ca^{2+}]_o$ conditions ($[Ca^{2+}]_o$=1.1 mM), and repeated the analyses above (Fig. 2.6b2-b4). Indeed, we observed that a drop in $[Ca^{2+}]_o$ dispersed clustering in the spike triplet count histogram, abolished correlations between latency and ISI, and reduced triplet emergence probability to chance levels. This establishes that specific values of tissue parameters are a necessary condition for the emergence of sequential structures in spike timing, and argues in favor of the hypothesis that such structures are a local property of cortex. With increased confidence in the NMC model's predictive powers, and a deepened appreciation for its utility as a tool for making inferences about emergent phenomena, we proceeded to develop a VSDI simulation layer for the model, the methods and results of which are chronicled in the remaining chapters.

(a) $[Ca^{2+}]_o$ = 1.25 mM   (b) $[Ca^{2+}]_o$ = 1.1 mM
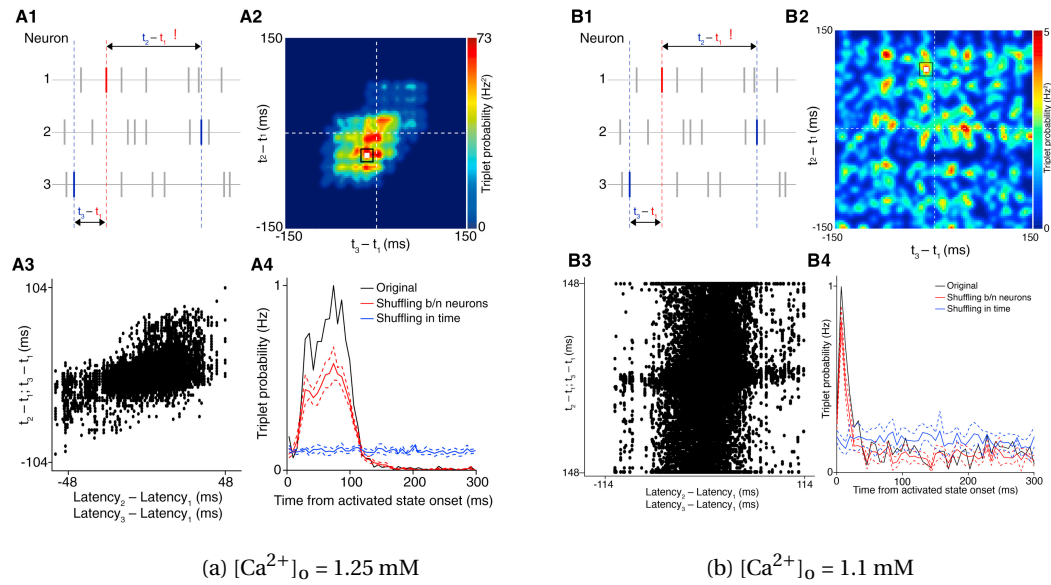
Figure 2.6 – **Repeating Spike Triplet Structure**

Precisely repeating triplet structures can be predicted from individual neural latencies under synchronous stimulation (20 thalamic fibers). Left: $[Ca^{2+}]_o$ = 1.25 mM, Right: $[Ca^{2+}]_o$ = 1.1 mM; cf. Luczak et al., 2007, Figure 5). (A1) Schematic depicting the structure of a spike triplet for a triad of neurons. (A2) Count matrix for a representative neuron triad. Black box indicates region containing precisely repeating triplets. White square signifies mode. (A3) Correlation between neural latency differences and triplet structures. (A4) Precisely repeating triplet probability peaks shortly after onset of activated state. This peak is significant when compared with two null hypotheses (independent Poisson model, blue curve; common excitability model, red curve). Dashed lines show standard deviation. (B1-B4) Same as for A1-A4, but with reduced extracellular calcium (1.1 mM). *Figure 2.6 and corresponding caption from Markram et al. (2015), reprinted courtesy of Cell Press.*
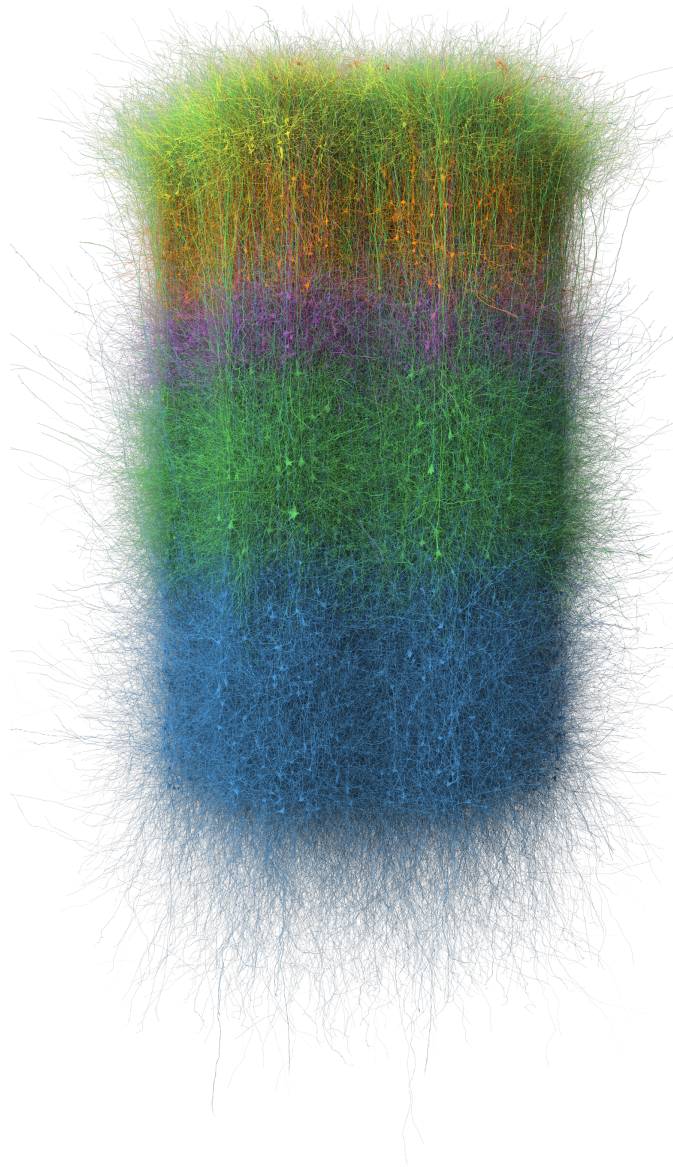
Figure 2.7 – **NMC Rendering**

A digital rendering of the NMC reconstruction. Hexagonal arrangement of seven individual columns depicted; "mosaic" configuration. 10% visibility (21,942 neurons rendered out of 219,422 total). *Image courtesy of BBP*.

3 Modeling Part II: *In Silico* VSDI

Here, we specify the methods (assumptions, algorithms, and hardware) used to construct an *in silico* model of VSDI.

3.1 Assumptions

Assembling a model necessarily entails making simplifying assumptions about the structure and interpretation of data that inform its parameters, and the rules governing the system in question. Premised on a description of the modeling pipeline wherein data constrain parameters which drive the model itself (data → parameters → model), we propose a categorization scheme for assumptions with the following three classes[1] :

- **Data Assumptions** Assumptions pertaining to the selection and interpretation of available data, or the inference of missing data points. Changes in data assumptions change model output, but do not cause conceptual alterations to the model.

- **Structuring Assumptions** Assumptions that dictate how data is organized and/or translated into model parameters. Generally, changes in these assumptions cause perturbations to the model, but leave its foundation intact.

- **Model Assumptions** Assumptions governing the form of the model itself. Variations at this level lead to a different model of a given system.

Using the scheme above, we detail the assumptions underlying our VSDI model:

---

[1]Conceptual classification scheme for modeling assumptions adapted from Reimann et al. (2019).

Table 3.1 – Table of Assumptions.

Data	1. Transverse dye diffusion is homogeneous and complete (i.e., tissue staining in $x - z$ plane is uniform).
	2. Voltage-sensitive probe is of type RH1691/2. This constrains: • depth-dependent dye penetration profile • λ_{peak} of excitation and emission light
	3. Voltage recordings in the circuit are stable after ∼1000 ms.
Structuring	1. Camera frame acquisition rate > simulation time step.
	2. Compartment voltage data is compressed into ∼1000 μm^3 voxels.
Model	1. Dye response is instantaneous.
	2. Dyes do not influence cellular physiology.[2]
	3. Imaging system consists of a tandem-lens epifluorescence macroscope (Ratzlaff and Grinvald, 1991).
	4. Beer-Lambert law approximates tissue-excitation light interactions.
	5. Tissue is a homogeneous, anisotropically scattering semi-infinite ($x - z$ dimension) medium.
	6. No pulsation artifacts.
	7. No photobleaching.
	8. No shot noise.
	9. VSD fluorescence $\propto$ changes in V_m.
	10. Dye application does not alter the optical properties of the tissue.
	11. Autofluorescence and background noise are constant and additive.
	12. Glial cell and other non-neuronal contributions are too slow or uncorrelated to be significant.
*Inherited	N.B. - As our model of VSDI rests atop a foundation supplied by the NMC model (see Chapter 2.1), the former accordingly inherits all assumptions native to the latter.

3.2 Calculating the Signal

The pipeline for producing VSDI datasets from compartmental simulation reports can be conceptually divided into three stages: 1) computation of a set of voxelized signal volumes, 2) compression of signal volumes into 2D images, and 3) post-processing. A detailed description of each stage in this pipeline follows below.
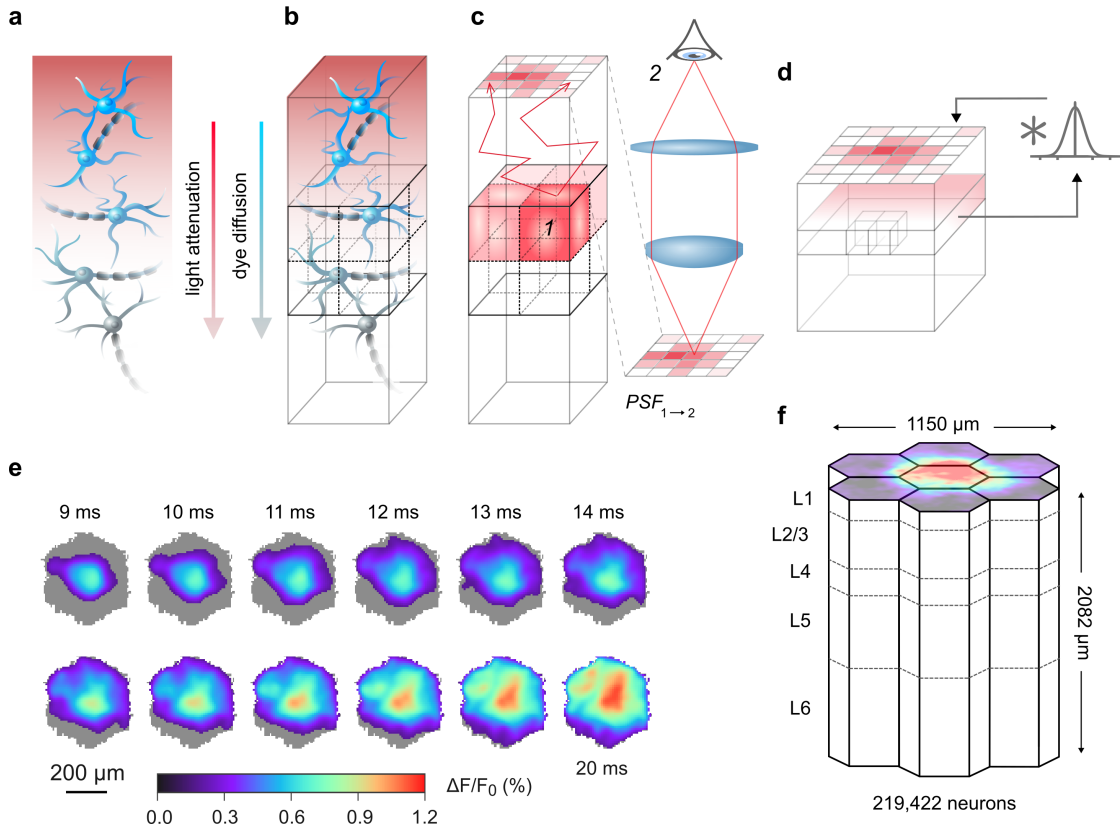
Figure 3.1 – *in silico* **VSDI Pipeline**

a-d, Schematic illustrating the *in silico* VSDI workflow. **a**, Neuron surface areas are scaled by prefactors accounting for dye diffusion and light transport in cortical tissue. **b**, Microcircuit volume is divided into voxels to facilitate calculations. **c**, Photons emitted from each voxel are scattered and absorbed throughout the tissue volume via Monte Carlo simulations. Photons reaching the cortical surface are propagated through a tandem-lens optical setup using ray transfer matrix analysis. Step **c** is performed once for a given circuit and optical setup to determine a depth-dependent point spread function (point spread from 1 to 2 in panel, i.e. from voxel to camera). **d**, Raw signals at each depth are convolved with their respective point spread function, and accumulated into a pixel array at the surface. **e**, Example VSDI image stack for 11 ms of spontaneous activity. Images were thresholded at 10% of peak response. **f**, Microcircuits were aggregated into a larger volume made of a central microcircuit column surrounding by six additional columns contacting each of the central column's hexagonal sides (the "mosaic"). This arrangement mitigates boundary effects within the central column, and provides a larger surface for the analysis of signal spread dynamics.

---

[2]This is a common implicit assumption in many VSD-based imaging studies. However, it's validity has been challenged by research that purports to show a potentiating effect on GABA receptors by dyes belonging to the blue oxonol family (Mennerick et al., 2010).

3.2.1 Voxelization

To begin, we assumed that the VSD signal emanating from a small section of neurite was linearly related to the product of its membrane surface area and V_m, since: 1) dyes are known to embed in cell membranes, and 2) fluorescence intensity is directly proportional to V_m (Berger et al., 2007, Ferezou et al., 2006, Gollnick et al., 2016, Grinvald and Hildesheim, 2004, Lippert et al., 2007, Petersen et al., 2003a,b). Our simulations rely on the NEURON simulation environment, which discretizes neural morphologies into small segments ("compartments") of connected equipotential cable (Hines and Carnevale, 1997). Capitalizing on the native data format, we calculated a raw VSD signal by multiplying the surface area and V_m of each compartment, and scaling this quantity as a function of cortical depth to account for the physics of dye diffusion and light transport (see Fig. 3.1a,b, and Section 3.3.1). To reduce data storage requirements, we enclosed the microcircuit in a bounding box of user specified dimensions, and divided this box into voxels, within which an aggregate signal was computed by summing the contributions of all compartments in that voxel (Fig. 3.1b,c). The (time-dependent) signal in each voxel can be expressed as:

$$v_{ijk}(t) = \sum_{r \in ijk} \alpha_r \Gamma(y_r) \cdot (\Delta V_m^r(t) + G_0) \tag{3.1}$$

where v_{ijk} denotes the value in the ijk^{th} voxel, α_r is the surface area of the rth compartment, $\Gamma(y_r)$ is the depth-dependent attenuation prefactor accounting for dye penetration and scattering/absorption of illumination light at depth y, ΔV_m^r is the change in membrane potential with respect to resting potential, and G_0 is a constant reflecting the combined contributions of background noise and autofluorescence (see Table 3.1). For a detailed derivation of $\Gamma(y_r)$, see Section 3.3.1. The value of G_0 was fixed by requiring that a 10 mV change in V_m correspond to a ~0.5% change in fluorescence over baseline ($\Delta F/F_0$), as reported by Ferezou et al. (2006), assuming an average resting potential of -65 mV (see Table 1).

To model the effects of scattering and absorption in the tissue, we used a Monte Carlo simulation-based approach (see Section 3.3.2) to compute an effective point spread function (PSF) for increasing depths along the axis perpendicular to the cortical surface (Fig. 3.1c). We used the PSF at each depth to determine the standard deviation of a Gaussian kernel, which we convolved with the horizontal data slice at that depth (Fig. 3.1d):

$$H_j = \begin{pmatrix} v_{0j0} & \cdots & v_{0jL} \\ \vdots & \ddots & \vdots \\ v_{Nj0} & \cdots & v_{NjL} \end{pmatrix} \tag{3.2}$$

$$\hat{H}_j(t) = H_j(t) * g(\sigma_j) \tag{3.3}$$

$$\hat{V} = \bigcup_j \hat{H}_j \tag{3.4}$$

H_j (Eq. 3.2) is a horizontal data slice at depth j, where $i \in \{0, \dots N\}$ and $k \in \{0, \dots L\}$. In Equation 3.3, $\hat{H}_j$ is the filtered data slice at depth j and g is a Gaussian kernel, with depth-dependent standard deviation σ_j. The union of all filtered slices yields the filtered data volume $\hat{V}$ (Eq. 3.4).

The parcellation of the microcircuit into voxels and implementation of Equations 3.1 through 3.4 above were carried out using EMSim (Electro-Magnetic Simulation Software). EMSim is a C++-based BBP proprietary software package, with a command line interface for calculating electromagnetic fields and other spatially distributed physical quantities.

3.2.2 Image Formation

Equation 3.4 provided the input to the next stage of computing VSDI data, wherein volumes were converted to image frames. To this end, each vertical (j-axis) column of voxels was accumulated into a single value, resulting in a two-dimensional matrix of pixels, which was stored as a single frame (Eq. 3.5) in a stack of images. VSDI signals were computed as the fractional change in fluorescence over resting intensity (Ferezou et al., 2007, 2009, Kleinfeld and Delaney, 1996, Orbach et al., 1985, Shoham et al., 1999). This gives raw and normalized signal intensities for each pixel in the image matrix:

$$F_{ik}(t) = \sum_j \hat{v}_{ijk}(t) \tag{3.5}$$

$$\text{VSD}_{ik}(t) = \frac{F_{ik}(t)}{F_{ik}^0} - 1 \tag{3.6}$$

where F_{ik}^0 is a baseline fluorescence image obtained by averaging the first 100 frames (50 ms of data sampled at 2000 Hz).

3.2.3 Post-processing

Fine, filamentous dendritic arbors belonging to neurons at the periphery of the circuit tend to extend out considerably past the bulk of soma-containing tissue. As a consequence, the bounding box circumscribing the circuit is large enough that some pixel coordinates (i, k) in Equation 3.5 above contain entries which reflect outlier contributions from single dendrites. To avoid issues with visualization, colormap normalization, and statistical errors, we removed any pixel whose corresponding vertical column of tissue did not contain a soma. To achieve this, we defined a somatic image mask as follows:

$$M_{ik} = \begin{cases} 1, & \text{if soma in } (i, k) \\ \text{NaN}, & \text{otherwise} \end{cases} \tag{3.7}$$

which was element-wise multiplied with equation 3.6, yielding:

$$[\text{VSD}_{ik}] = M_{ik} \cdot \text{VSD}_{ik} \tag{3.8}$$

Equation 3.8 yields a time-ordered collection of spatially distributed VSD images (Fig. 3.1e), which we computed for various permutations of microcircuit geometry (Fig. 3.1f) to probe population dynamics in the NMC model. For analyses requiring a spatial average, we compressed equation 3.8 into a one-dimensional quantity:

$$\text{VSD} = \frac{1}{\|M\|_0} \sum_{i,k} [\text{VSD}_{ik}] \tag{3.9}$$

where $\|M\|_0$ is the $L0$ norm of somatic mask M (i.e., the number of real, non-zero entries).

3.3 Offline Procedures

3.3.1 Signal Attenuation

The degree of signal attenuation due to uneven staining along the depth axis was interpolated from data measured in four mouse brains treated with RH1691 voltage-sensitive dye, flash-frozen and sliced into 20 μm thick cryosections (Ferezou et al., 2006). A depth-dependent saturation curve for VSD RH1691 (see Ferezou et al. (2006), Fig. 2L) was digitized using software written in MATLAB (MathWorks), and converted into a text file (Fig. 3.2).

As declared in Table 3.1, we assumed a Beer-Lambert law approximation for the attenuation of incoming illumination light in an epifluorescence configuration. The Beer-Lambert law states that for a single attenuating species in a non-scattering material sample with absorption

coefficient μ_a, light intensity (I) decays exponentially as a function of optical pathlength (l) (Baker et al., 2014, Taddeucci et al., 1996, Cheong et al., 1990):
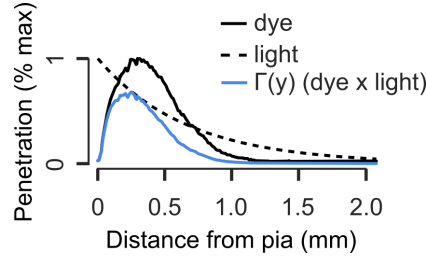
Figure 3.2 – **Attenuation Profiles**

Black line: Digitized dye penetration profile adapted from Ferezou et al. (2006). Dashed line: Beer-Lambert approximation for exponential attenuation of light intensity through tissue. Blue line: product of attenuation for dye and light ($\Gamma(y)$).

$$I(l) = I_0 e^{-\mu_a \cdot l} \tag{3.10}$$

However, this relationship breaks down under conditions of turbidity, i.e. in highly scattering media such as biological tissue, as scattering within the tissue tends to increase mean photon pathlength between the source and detector. Thus, a modified Beer-Lambert law (MBLL) was introduced, which captures the statistical increase in photon pathlength through a "differential pathlength factor" (DPF), defined as the ratio of the true mean pathlength to the geometrical source-detector separation (Bhatt et al., 2016, Al-Juboori et al., 2013, Dimofte et al., 2005, Baker et al., 2014). The optical density (OD), defined as the negative logarithm of the ratio of detected to incident light, is written (Bhatt et al., 2016):

$$\text{OD} = -\ln\left(\frac{I(l)}{I_0}\right) = \mu_a \cdot \text{DPF} \cdot l + G \tag{3.11}$$

where G is a factor accounting for measurement geometry. Equation 3.11 can be rewritten in terms of an effective exctinction coefficient, μ_{eff}:

$$I(l) = I_0 e^{-\mu_{\text{eff}} \cdot l} \tag{3.12}$$

$$\mu_{\text{eff}} = \sqrt{3\mu_a(\mu_s' + \mu_a)} \tag{3.13}$$

where $\mu_s' = \mu_s(1 - g)$ is the reduced coefficient of scattering. We note that μ_{eff} is also an implicit function of photon wavelength, λ. For a detailed derivation of Equation 3.13, see Bhatt et al. (2016), Al-Juboori et al. (2013). As reported values for the optical properties of biological tissues can vary substantially (Yaroslavsky et al., 2002, Johansson, 2010, Cheong

et al., 1990), and cf. (Mesradi et al., 2013, Azimipour et al., 2014), we used dual independent approaches to converge on a value for μ_{eff}. First, we attempted a semi-analytical estimate, wherein measurements for μ_a and μ_s' obtained at $\lambda \sim 630$ nm in rodent gray matter by Mesradi et al. (2013) were substituted into Equation 3.13 (630 nm is a typical illumination wavelength for RH1691/2 (Ferezou et al., 2006, Lustig et al., 2013, Lippert et al., 2007, Shoham et al., 1999, Mutoh et al., 2015)). We compared this to a value interpolated for $\lambda \sim 630$ nm from a study by Al-Juboori et al. (2013), in which μ_{eff} was acquired directly through an empirical fit to data measured in various brain regions in adult mouse. We settled on a value of 1.5 mm^{-1} since both approaches yielded a similar estimate. Finally, setting I_0 to 1, and multiplying equation 3.12 by an empirical dye saturation profile P(y) (Fig. 3.2, black line) determined a scaling prefactor $\Gamma(y)$ (Fig. 3.2, blue line) for each voxel in equation 3.1:

$$\Gamma(y) = P(y) e^{-\mu_{\text{eff}} \cdot y} \tag{3.14}$$

3.3.2   Point Spread Function

We calculated an empirical, depth-dependent point spread function (PSF) to account for blurring in the final image due to both scattering of emitted fluorescence photons in cortical gray matter, and also optical distortions caused by out-of-plane signal. Our method for calculating the PSF consisted of two steps: first, we used a Monte Carlo (MC) simulation-based approach to model the scattering and absorption of photons emitted from a point source within the tissue volume; second, we used ray transfer matrix analysis to trace the trajectories of those photons through a tandem-lens optical system onto a sensor at the image plane.

Cortical tissue is known to be a highly scattering, turbid medium (Gysbrechts et al., 2014, Azimipour et al., 2014) (see Section 3.3.1). Accurate modeling of the light propagation in this tissue is possible through MC simulations of photon transport, which we carried out using a proprietary library built on an open-source framework for physical rendering, the Physically-Based Rendering Toolkit (PBRT) (Pharr et al., 2016). We extended the PBRT framework to simulate photon interactions with highly turbid media using forward MC simulations based on an algorithm proposed by Abdellah et al. (2017). In this framework, virtual photons are emitted at a specified location, rate, and angle within the tissue. Each photon is propagated in a straight line from the origin until the stochastic occurrence of either a scattering or absorption event. The intensity of the fluorescence signal that reaches the detector is computed with the following Monte Carlo estimator:

$$I(\mathbf{x}', \omega') = \frac{1}{N} \sum_{i=1}^{N} \frac{I(\mathbf{x}_0^i, \lambda)}{p(\mathbf{x}_0^i)} \prod_{j=1}^{M} \frac{\mu_s' \phi(\mathbf{x}_j, \omega_j, \omega_{j+1}, \lambda) \tau(\mathbf{x}_j, \mathbf{x}_{j-1}, \lambda)}{p(\omega_j) p(t_j)} \;, \quad \text{where} \quad (3.15)$$

$$\tau(\mathbf{x}_j, \mathbf{x}_{j-1}, \lambda) = e^{-\int_0^{\|\mathbf{x}_j - \mathbf{x}_{j-1}\|} \mu_t \mathrm{d}t} \;, \quad \text{and} \quad (3.16)$$

$$\mu_t = \mu_s + \mu_a \quad (3.17)$$

For a detailed explanation of the terms in Equation 3.17, see Table 4 in the Appendix. To determine the PSF, we moved an isotropically radiating point source of 10^8 photons through a semi-infinite (lateral extent) volume of tissue beginning at the bottom of the microcircuit in increasing increments of 50 μm, and allowed each photon to scatter until it was either absorbed, or exited the cortical surface. Coefficients of reduced scattering and absorption at ~665 nm (typical peak emission wavelength for RH1691/2 (Ferezou et al., 2006, Lustig et al., 2013, Lippert et al., 2007, Shoham et al., 1999, Mutoh et al., 2015)) were taken to be 4 mm^{-1} and 0.4 mm^{-1}, respectively, interpolated from optical measurements made in rat gray matter for wavelengths of light spanning 450 to 700 nm (Mesradi et al., 2013) (see also Section 3.3.1 and Appendix, Table 2). Refraction of photons at the tissue-air interface was calculated using the vector formulation of Snell's law (Greve, 2004):

$$\mathbf{t} = \frac{n_1}{n_2}\mathbf{l} + \left(\frac{n_1}{n_2}\cos\theta_1 + \sqrt{1 - \sin^2(\theta_2)} \right)\mathbf{n} \quad (3.18)$$

which relates the angles of incidence and refraction (θ_1 and θ_2, respectively) for a beam of light crossing a boundary between two isotropic media with refractive indices n_1 and n_2. In the formula above, $\mathbf{l}$ is a unit vector indicating the direction of incident light, $\mathbf{n}$ is the surface normal vector, and $\mathbf{t}$ is a unit vector indicating direction of egress.

Using ray transfer matrix analysis, photons emanating from the tissue surface were propagated through an optical system modeled after a tandem-lens epifluorescence macroscope (low magnification, high field-of-view) setup first proposed by Ratzlaff and Grinvald (1991), and subsequently used in several VSDI studies (Ferezou et al., 2006; Petersen et al., 2003a, 2003c). The system consists of two compound lenses (modeled using the thin lens approximation) set to infinite focus and placed face-to-face (Ratzlaff and Grinvald, 1991), dictating the

relationship between input and output rays according to:

$$
\begin{pmatrix} r' \\ \theta' \end{pmatrix} = \overbrace{\begin{pmatrix} 1 & f_2 \\ 0 & 1 \end{pmatrix}}^{\mathbf{L}_2\text{(below: } \mathbf{T}_2)} \begin{pmatrix} 1 & 0 \\ -\frac{1}{f_2} & 1 \end{pmatrix} \underbrace{\begin{pmatrix} 1 & p \\ 0 & 1 \end{pmatrix}}_{\mathbf{T}_1} \overbrace{\begin{pmatrix} 1 & 0 \\ -\frac{1}{f_1} & 1 \end{pmatrix}}^{\mathbf{L}_1} \begin{pmatrix} r \\ \theta \end{pmatrix} \tag{3.19}
$$

where r is the radial distance from the central axis of each lens and θ is the approach angle with respect to this axis, $\mathbf{L}_1$, $\mathbf{L}_2$ are transfer matrices for the objective and tube lenses, respectively (with focal lengths f_1 and f_2) and $\mathbf{T}_1$, $\mathbf{T}_2$ represent translations from objective lens to tube lens, and tube lens to detector, respectively.
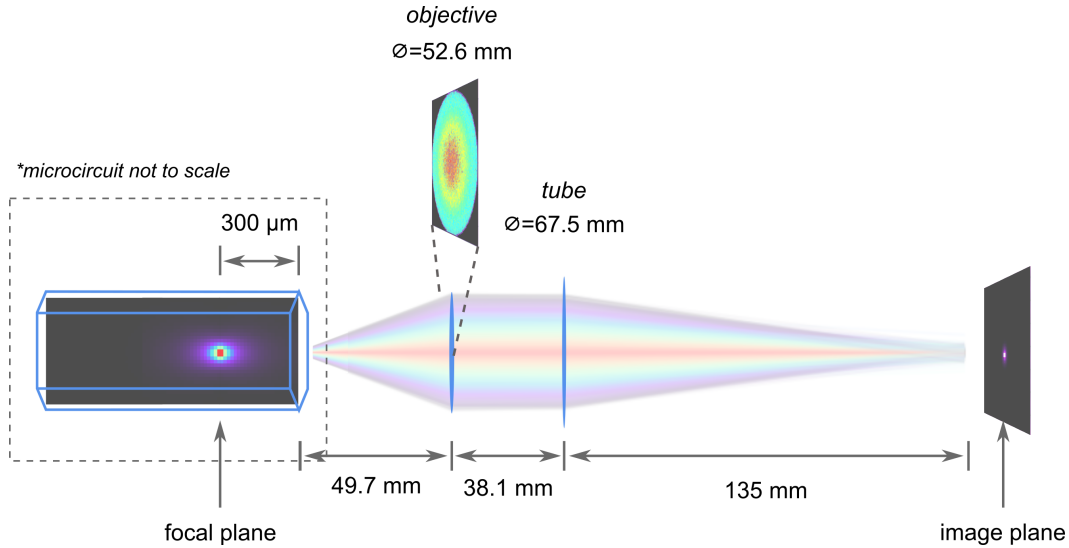
Figure 3.3 – **Tandem-Lens Optical System**

Fluorescence imaging was modeled assuming a tandem-lens "macroscope" optical system. The working distance was adjusted to result in a focal plane 300 μm below the pial surface, given the diameters and separation of the objective and tube lenses.

The parameter p in term $\mathbf{T}_1$ is the "infinity space pathlength", or the distance between the lenses, and is determined from the focal lengths and f-numbers ($f/$) of the two lenses, and numerical aperture (NA) of the objective lens (Edmund Optics):

$$
\text{NA} = \frac{1}{2 f_1 /} \tag{3.20}
$$

$$
p = \left(\frac{f_2}{f_2 /} - \frac{f_1}{f_1 /} \right) \cdot \frac{f_2}{2 f_1 \text{NA}} \tag{3.21}
$$

Optical parameters (focal lengths, f-numbers and working distance) were taken from Petersen et al. (2003a) (see Appendix, Table 2), resulting in a focal plane ~300 μm below the pia. The point source produced a sunburst image pattern on the detector array for each depth, to which a two-dimensional Gaussian surface was fit using nonlinear optimization (see Appendix for Python code). From these surfaces, we extracted the average spatial standard deviation, and fit the resulting array of values to a decaying exponential function to determine a depth-dependent PSF for the entire tissue-lens system. The standard deviations extracted from our PSF determined the spatial kernel widths for convolution of data slices with a Gaussian filter $g(\sigma)$ (Eq. 3.3).

3.4   Hardware

A 2-rack Intel supercomputer using dual socket, 2.3GHz, 18 core Xeon SkyLake 6140 CPUs, with a total of 120 nodes, 348 GB of memory, and 46 TB of DRAM was used to run the simulations and carry out analysis.

4 Results

4.1 Evoked VSDI Response Dynamics

In the following sections, we explore several aspects of mesoscale dynamics in the NMC in response to TC stimulation using *in silico* VSDI. Where possible, we compare our findings to the results of analagous *in vivo* experiments.

4.1.1 Individual NMC Responses

Chapter 2.1 describes the process of reconstructing a rodent neocortical microcircuit informed by experimental data. This process was probabilistic in that key parameters were sampled from statistical distributions, and furthermore, multiple datasets were used to constrain these distributions. In particular, layer height and cell density data from five different rats were used to construct individual realizations of the NMC (Bio-1-5), and also pooled to build an "average" NMC (Bio-M) (Markram et al., 2015). Furthermore, each version of the model was instantiated seven times, giving a total of 42 instances of the NMC. It was shown that Bio-1-5 and Bio-M have distinct functional properties, including variance in delay to first spike following TC stimulation, sensitivity to differences in stimulus location, and critical value of $[Ca^{2+}]_o$ (Markram et al., 2015). We were interested to test how differences among individuals in response to TC stimulation might bear on *in silico* VSDI measurements. Consistent with previous findings, we saw that at *in vivo*-like $[Ca^{2+}]_o$ (1.25 mM), Bio-1-5 were each slightly more or slightly less "critical", as indicated by the presence or absence of a small regenerative second peak following the initial response (supercritical: Bio-2, Bio-3, Bio-M; subcritical: Bio-1, Bio-4, Bio-5) (Fig. 4.1a). Time to peak (22.9 ± 0.6 ms) was consistent, indicating uniformity of feedforward network dynamics. In contrast, the magnitude of peak fluorescence (1.65 ± 0.14 %) was somewhat more variable, likely reflecting variability in baseline activity due to differences in cell densities and location on the synchrony-asynchrony spectrum. We also quantified the fractional composition of each microcircuit by numbers of neurons according to layer and cell type (Fig. 4.1b). An analysis of the deviations of these values between microcircuits revealed that numbers of L1 and L4 inhibitory cells were most subject to variation (Fig. 4.1c).

The size of the L4 inhibitory population has significant implications for modulating response dynamics, as L4 is strongly innervated by VPM projection fibers (Markram et al., 2015), and inhibitory cells in that layer are thus situated as "first responders" to sudden increases in activity. Suggestively, the three microcircuits whose L4 inhibitory populations are largest (relative to the mean) are the same that display a regenerative peak in response to stimulation (Fig. 4.1, red text). However, we leave clarification of the precise mechanism underlying this phenomenon to future work.
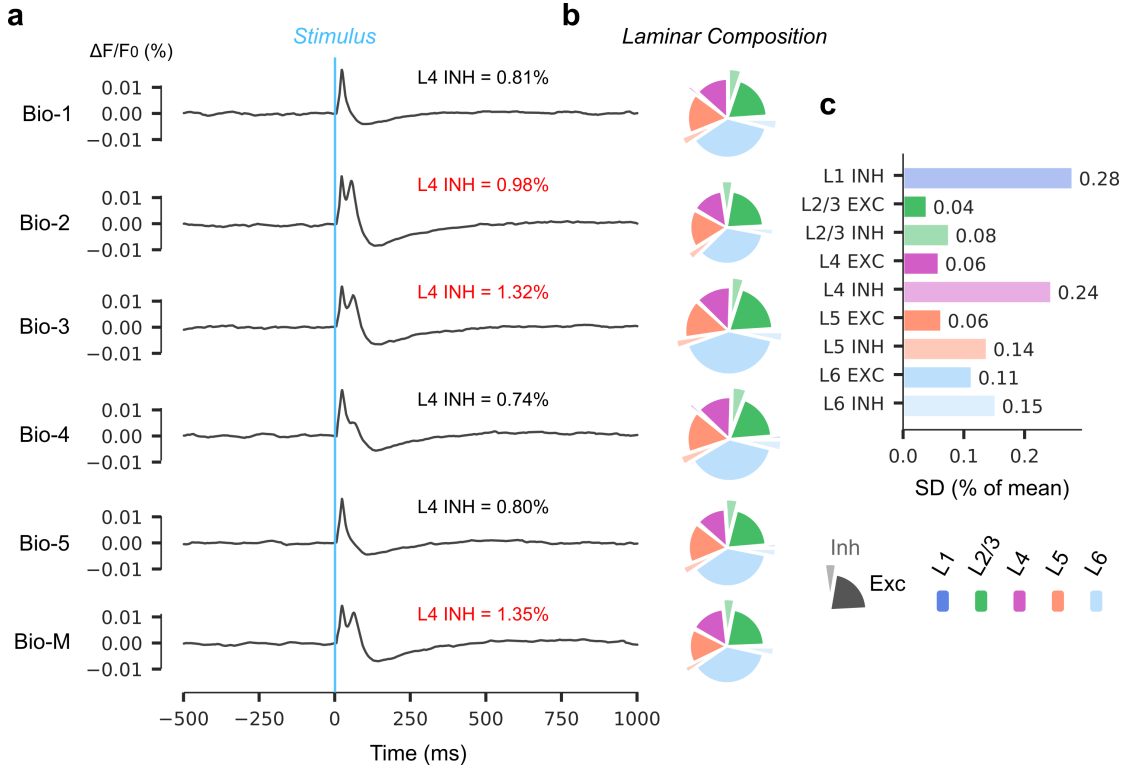
Figure 4.1 – **Individual NMC Responses**

a, Spatially averaged VSDI data for Bio-1-5 and Bio-M, $[Ca^{2+}]_o = 1.25$ mM. Vertical blue line indicates stimulus. Text indicates percent deviation from mean in L4 inhibitory populations (black: subcritical response; red: supercritical response). **b**, Number of cells by layer (color) and cell type (standard or exploded pie slices) for each individual microcircuit. Radius of each pie plot is proportional to the total number of neurons. **c**, Standard deviations (percent deviation from mean) for numbers of neurons by layer and cell type.

4.1.2 Transverse View VSDI Dynamics

Propagating waves of activity are thought to be implicated in the representation and integration of information in cortex (Borgdorff et al., 2007, Contreras and Llinás, 2001, Ferezou et al., 2006, 2007, Lustig et al., 2013, Petersen and Sakmann, 2001). Activity spread dynamics are commonly characterized by measuring the wavefront velocity (phase velocity) and aspect ratio of the propagating wavefront, the spatial extent and timecourse of cortical activation, and the dependence of these quantities on stimulus strength (cf. Fehérvári et al. (2015)).

To quantify the similarity between the evoked response dynamics of our model and those reported in literature, we conducted a series of whisker flick-like trials and examined the resulting spread of activity. Our stimulation protocol consisted of a single pulse of activity in 60 contiguous TC fibers emanating from a virtual VPM, and projecting to the geometric center of a concentric arrangement of 7 NMCs (the "mosaic", Fig. 3.1f) which provided a larger surface area for the analysis of spatially distributed signals. We observed a radially expanding pattern of activation centered around the location of stimulus delivery, which expanded to fill the entire surface over the course of several 10s of milliseconds, reaching peak fluorescence at ~57 ms post-stimulus (Fig. 4.2a,b). Note that time to peak was delayed with respect to a single NMC column (Fig. 4.1), implying that response dynamics are sensitive to circuit size. The peak was immediately followed by a period of declining activity characterized by increasing hyperpolarization, which undershot baseline fluorescence, reaching a minimum at 170 ms, and gradually recovering to within 10% of baseline after ~510 ms. To quantify the temporal persistence of the signal, we calculated the half width duration (decay time to 50% of signal peak, 88 ms). The time to peak and half width duration compared favorably to the findings of Ferezou et al. (2006), who report values of ~45 ms, and 86 ± 69 ms, respectively (Fig. 4.2b). We also considered the relationship between the instantaneous firing rate (3 ms bins) and the VSDI signal in a 100 ms post-stimulus window (Fig. 4.2c,d). Our simulations indicate that peak AP firing occurred ~7 ms *prior* to peak VSD fluorescence, contrary to the intuition that increased mean V_m precipitates population spiking. This result is supported by two experiments in ferret visual cortex using simultaneous VSDI and multiunit recordings (Eriksson et al., 2008, Roland et al., 2006), and at least one study in rat barrel cortex wherein single-cell APs occurred slightly prior to peak local VSD fluorescence (Petersen et al., 2003a).

Notably, a differing VSDI activity timecourse was observed at the stimulus delivery location relative to the mosaic periphery (Fig. 4.2g). At peripheral points along the x- and z-axes (+540 μm and +460 μm, respectively), the rising and falling phases of the fluorescence response were almost identical to the spatial mean. In contrast, signal recorded at the stimulus location exhibited an initial transient within the first 12 ms of stimulus onset, and then gradually rose to peak fluorescence. This response pattern (initially confined, expanding thereafter) was also visible in the spatial profile of activation over time as an initially sharp peak, which gradually rose and then flattened into a plateau (Fig. 4.2f). *in vivo* measurements of the optical response to evoked activity exhibit a similar ativity pattern wherein VSDI signals saturate in a locally confined region near the stimulation site within the first 10-20 ms, and subsequently expand in the transverse plane (Civillico and Contreras, 2006, Fehérvári et al., 2015, Petersen, 2007, Petersen et al., 2003a). Fehérvári et al. (2015) report similar fluorescence dynamics in an *in vivo* VSDI study of mouse primary visual cortex (V1). In particular, they find that in a localized region around the site of an applied 50 μA current impulse, fluorescence rapidly increases within ~10 ms, before saturating and then expanding laterally. They propose that the initial peak primarily reflects monosynaptic excitatory postsynaptic potentials (EPSPs), which are followed by the propagation of disynaptic activity at greater latencies. This explanation is consistent with our finding that the first response occurs locally and quickly plateaus, since it
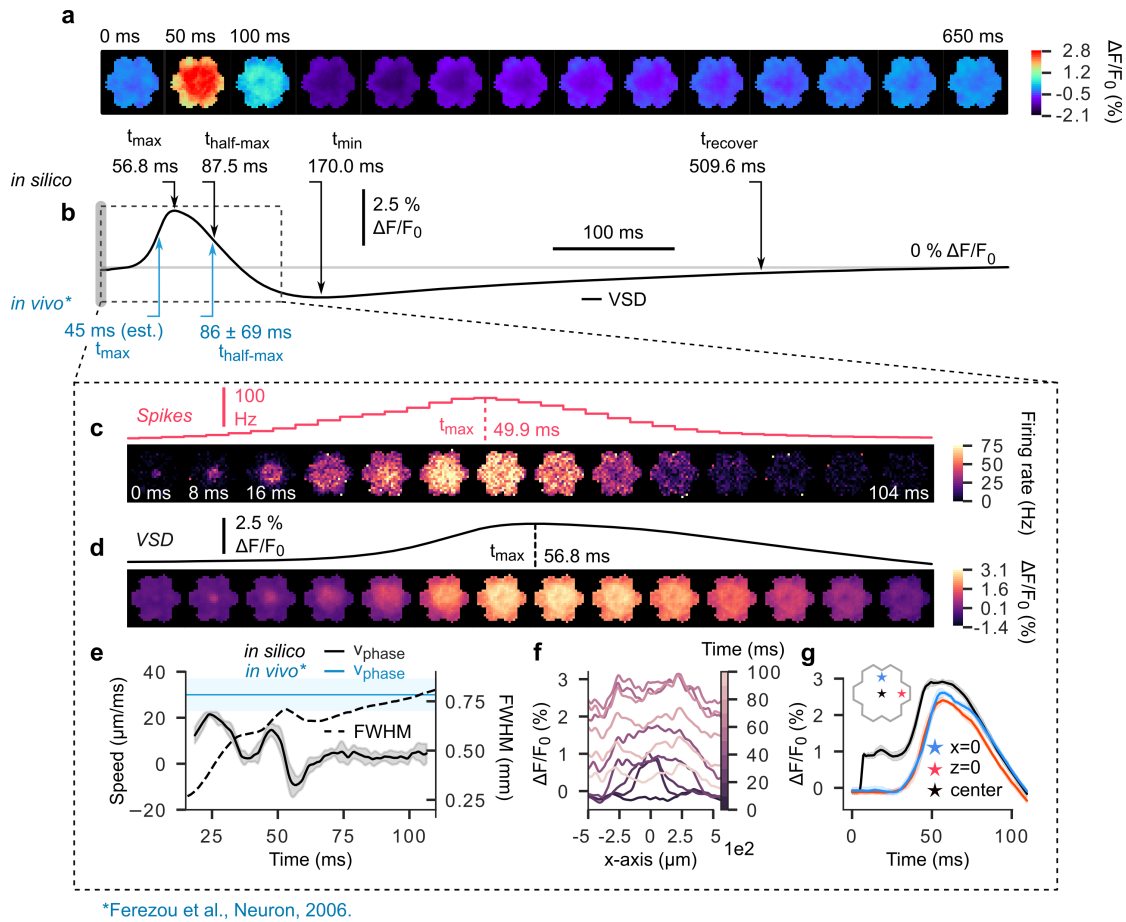
Figure 4.2 – **Evoked VSDI Response Dynamics**

a, 650 milliseconds of simulated stimulus-evoked VSDI signals in the mosaic. The stimulus consists of a single, coincident pulse of activity in 60 contiguous thalamic projection fibers innervating the center of the interior microcircuit (delivered at t=0 ms). **b**, Timecourse of spatially averaged VSDI signal in **a**. Upper arrows (black) indicate points of interest along the curve. From left to right: peak latency, half width duration (time to decay to 50% of signal peak), time of signal minimum, recovery time (earliest time after minimum for amplitude to stably decay to within 10% of baseline). Bottom arrows (blue) indicate *in vivo* values for peak latency and half width duration reported in literature. **c**, Top: PSTH of spiking activity for time window (dashed box) indicated in **b** (3 ms bins). Bottom: pixel-wise PSTH (mean firing rate of all cells under each pixel) over same time window (8 ms bins). **d**, Top: expanded view of time window (dashed box) indicated in **b**, detailing ascending and descending phases of stimulus-evoked spatially averaged VSDI signal. Bottom: same as above, but for spatially extended VSDI signal, where each frame was computed by averaging activity in 8 ms intervals. **e**, Activity wavefront propagation velocity (solid line, left axis), and wavefront size (full width at half maximum, dashed line, right axis). Blue horizontal line and shaded region show *in vivo* measurements of stimulus-evoked wavefront propagation velocity reported in literature. Solid blue line: mean value, shaded blue region: measurement range. **f**, Spatiotemporal evolution of VSDI signal along the *x*-axis (*z*=0, i.e. a horizontal line across the surface of the mosaic). Lightening hue represents passage of time. **g**, Timecourse of VSDI activation at specific locations on the cortical surface. Blue star: circuit periphery along the *z*-axis. Red star: circuit periphery along the *x*-axis. Black star: circuit center.

is likely due to feedforward PSPs evoked by direct TC innervation at the center of the NMC. Subsequent activity spread would occur only following a monosynaptic delay, as the targets of TC projections propagate the signal to their postsynaptic partners.

In order to characterize the propagation velocity of the evoked activity wavefront, we fit each image frame to a two-dimensional Gaussian surface and measured the change in the full width at half maximum (FWHM) over time[1] (Fig. 4.2e). We found that activity wavefronts underwent two sequential bursts of expansion prior to peak VSD fluorescence, reaching a peak velocity of ~20 μm/ms. Subsequently, the wavefront entered a period of contraction (-10 μm/ms) near the VSDI signal peak, before gradually returning to baseline (fluctuations near zero). *In vivo* VSDI experiments have documented wavefront propagation speeds within an order of magnitude of those reported above. For example, Petersen et al. (2003a) use a Gaussian fit of the cross-sectional profile of VSD images to estimate that whisker deflection-evoked waves in urethane or halothane anesthetized rodent barrel cortex propagate along barrel rows at a speed of ~60 μm/ms, and barrel arcs at ~33 μm/ms. Table 4.1 summarizes cortical wavefront propagation velocities reported in literature. We note that in comparison to average signal transmission speeds reported in literature, the wavefront phase velocities calculated here are relatively low. We speculate that this may be due in part to slicing of medium-range (intracortical) axons during the morphology reconstruction process. It is well known that extended axonal arbors are at risk of slicing during histological processing, and efforts were made to repair severed arbors using statistical methods (Markram et al., 2015). However, it is unlikely that such repairs would fully correct for slicing artifacts, leaving open the possibility that significant numbers of medium range connections are missing. If true, it would tend to decrease wavefront propagation speeds, as signal transmission would be forced to proceed strictly through short-range connections. Another factor for consideration is the choice of wavefront quantification method. Several of the *in vivo* studies reported in Table 4.1 use amplitude thresholding to calculate a wavefront progagation speed. In this method, VSDI pixels that do not cross an arbitrarily specified threshold (usually some percentage of peak fluorescence) are excluded from analysis. Calculation of phase velocity proceeds as the number of pixels advanced in a particular direction per unit time at the boundary of the thresholded response. Thus, wavefront velocity calculated in this way is sensitive to threshold selection. In addition, thresholding is subject to contamination by shifts in centroid location. Lustig et al. (2013) report that the centroid of VSDI response (the "center of gravity", loosely speaking), can shift over time by as much as 1.2 mm in only 11.2 ms, meaning that advancement of pixels at the boundary may be artificially boosted or inhibited by a global displacement of responding pixels. The movement of response centroids and arbitrary selection of thresholds would tend to increase the variance of reported phase velocities, making consensus, and therefore precise corroboration using *in silico* VSDI, more difficult.

---

[1]FWHM: distance between two points symmetrically distributed about Gaussian peak, such that surface is 50% of peak at those points.

Table 4.1 – Wavefront Propagation Velocities

study	min., max. speed	wavefront quantifica- tion	experiment protocol	anesthesia	brain region	animal
Petersen et al. (2003a)	33 (barrel arc), 60 (barrel row) μm/ms	Gaussian fit (cross-sectional)	whisker deflection (*in vivo*)	urethane/ halothane	barrel cortex	rat P21-P28
Fehérvári et al. (2015)	47±12, 66±15 μm/ms	amplitude threshold (50% peak)	50 μA current injection (*in vivo*)	urethane	visual cortex	mouse P56-P140
Ferezou et al. (2006)	27±7 (urethane), 30±7 (awake) μm/ms	amplitude threshold (50% peak)	spontaneous (*in vivo*)	urethane or isoflurane or none	barrel cortex	mouse
Lippert et al. (2007)	200±100 μm/ms	—	whisker deflection (*in vivo*)	isoflurane	barrel cortex	rat
Petersen et al. (2003b)	<10, >100 μm/ms	amplitude threshold (50% peak)	spontaneous (*in vivo*)	urethane or ketamine/ xylazine or halothane	barrel cortex	rat/mouse P21-P35
Contreras and Llinás (2001)	181±44 (L2/3), 217±53 (L5) μm/ms	—	white matter stimulation, 1-5 V, 100 μs (*in vitro*)	sodium pen-tobarbital	visual/ somatosen-sory cortex	guinea pig
Chavane et al. (2011)	90 μm/ms	2D Gaussian fit	sinusoidal luminance gratings (*in vivo*)	althesin and pancuro-nium bromide	visual cortex	cat
Civillico and Contreras (2005)	30 (single whisker), 196 μm/ms (mult. whiskers)	amplitude threshold (2x SD of baseline per pixel)	whisker deflection (*in vivo*)	ketamine-xylazine	barrel cortex	mouse
NMC	**-10, 20 μm/ms**	**2D Gaussian fit**	**whisker deflection (*in silico*)**	**—**	**somato-sensory cortex**	**rat**

4.1.3 Sagittal View VSDI Dynamics

In addition to the standard transverse surface view, we imaged sagittal ($x - y$ plane, Fig. 4.3a) tissue slices with *in silico* VSDI to investigate the laminar dynamics of stimulus-evoked activity in the NMC. For this analysis, we assumed rotational symmetry about the y-axis, which nullifies considerations regarding dye and light penetration (since columns of tissue perpendicular to the imaging plane are homogeneous). We saw that the earliest response had a high aspect ratio and vertical orientation, and occurred primarily in L5, but extended into L6 and the bottom of L4 (Fig. 4.3c). By 40 ms post-stimulus, a clear peak of activity localized in L5 began to emerge, and gradually expand. From this point on, the response continued to increase in overall area and magnitude, reaching the bottom of L2/3, but also developing a strong horizontal orientation at the y-position depth of peak response. By 60 ms, the signal began to decay, proceeding in a uniform fashion until only a lateral patch of activity remained in L5. This dynamical pattern is summarized in Fig. 4.3b, which illustrates the time evolution of a vertical line bisecting each sagittal image frame (i.e., "linescan"), showing the simultaneous early response onset in L4 through L6, and L5's delayed decay. Experimental evidence from recordings in rodent barrel cortex also confirms near simultaneous activation of neurons in L4 through L6 in response to whisker stimulation (Kock et al., 2007), contrary to earlier claims that electrical activity originates in L4 and subsequently spreads to other layers in a predetermined sequence.

Finally, we were interested to compare the timecourse of the cross-sectional VSDI response to spiking activity in the central column (MC2), where the stimulating TC fibers innervate the circuit (Fig. 4.3d). We hypothesized that the relatively shorter time to peak evident in VSDI simulations of individual NMCs (Fig. 4.1a) may reflect local dynamics that are washed out by a larger circuit area. Indeed, spike rates in MC2 exhibited a double peak not apparent in the VSDI response, and at a time prior to maximal fluorescence (~18 ms vs. ~57 ms). This indicates that as activity expands to cells in peripheral columns, V_m fluctuations in dendritic processes reaching back into the central column obscure local dynamics and prolong overall fluorescence.

4.2 Signal Constituents

VSDI signals are linearly proportional to the product of local V_m and membrane surface area (see Section 3.2). Moreover, signals originating from neurites located in deeper layers are significantly more attenuated than those emanating from superficial layers due to uneven dye penetration and light-tissue interactions (see discussion in Section 3.3.1 and Fig. 3.2). It follows that the morphology, location, and orientation of a given cell affect the magnitude of its contribution to the optical response. To better understand these influences, we analyzed the fractional contributions of cortical layers and cell types to the overall VSDI signal, which we calculated as follows:
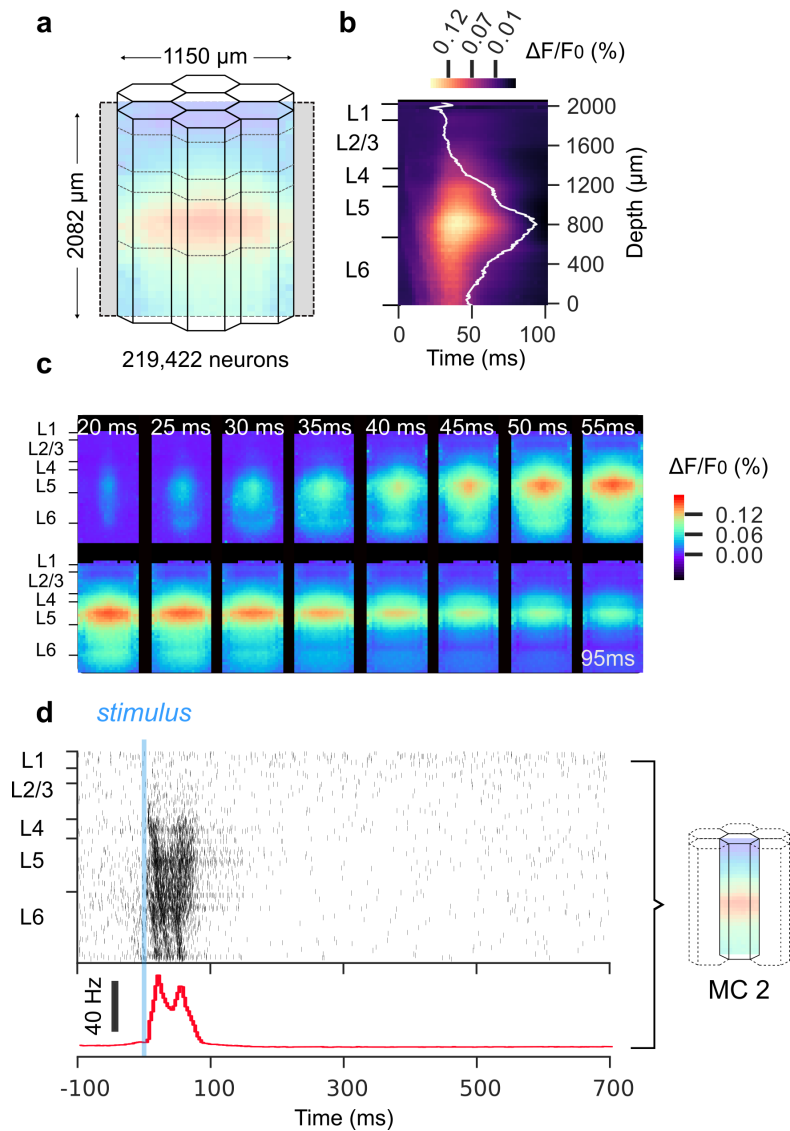
Figure 4.3 – **Sagittal Slice VSDI**

a, Mosaic configuration of NMC model (7 concentric columns), with sagittal imaging plane (indicated in gray) bisecting the volume along the y-axis (depth). **b**, Linescan of cross-sectional VSDI activity: matrix of time series data for a vertical line through the center of the imaging plane. White line overlay is sum of each matrix row (i.e. the integral over time for each depth). **c**, VSDI data for a sagittal slice through the mosaic in 5 ms intervals (20-95 ms post-stimulus). **d**, Top: raster plot of 2000 randomly sampled cells in the central column (MC2). Bottom: same data as above, but in time histogram format.

$$\left[v_{ijk}(t) \right]_{S_x} = \left[\sum_{r \in ijk} \alpha_r \Gamma(y_r) \cdot (\Delta V_m^r(t) + G_0) \right]_{S_x} \tag{4.1}$$

$$\left[\frac{\Delta F_{ik}(t)}{F_{ik}^0} \right]_{S_x} = \frac{\sum_j \left[\hat{v}_{ijk}(t) \right]_{S_x}}{F_{ik}^0} - 1 \tag{4.2}$$

where the notation $[\cdots]_{S_x}$ indicates restriction to only the neurites of cells belonging to subset x (i.e. a given layer or cell type). Note that on the right hand side of Equation 4.2, the denominator F_{ik}^0 is computed without restriction. Also, convolution with a Gaussian kernel is implied between Equations 4.1 and 4.2 (by the presence of the hat on the term $\hat{v}_{ijk}$), in analogy with Equations 3.2 and 3.3.

4.2.1 Outsize and Differentiated Roles for Layers 2/3 and 5

In agreement with previously reported results (Ferezou et al., 2006, Gollnick et al., 2016, Lippert et al., 2007, Petersen et al., 2003a), we found that >90% of the raw fluorescence originated within 500 μm of the pial surface (Fig. 4.5b). Furthermore, we found that neurites belonging to L2/3 and L5 neurons monopolized the "effective surface area" (i.e., the quantity that results from multiplying the original surface area of each neurite by a depth-dependent scale factor accounting for dye penetration and light transport), contributing 44.9% and 43.7% of the total, respectively. As predicted by the distribution of effective surface area, L2/3 and L5 also constituted the bulk of the VSDI total (47.8% and 37.6%, respectively, n = 10 trials) during spontaneous activity (Fig. 4.5c,d). Cross-correlation revealed mutual positive correlations between all layers and the VSDI total (Fig. 4.5e). However, during evoked activity, L5 contributed upwards of 67% of the signal whereas L2/3 neurites constituted 19% (Fig. 4.5f,g). That L2/3 contributed nearly 20% of the evoked signal highlights the strength of the suppression of activity in deeper layers by VSD imaging physics; results of sagittal VSDI simulations indicated that even at peak response, L2/3 was vastly overshadowed by L4 through L6 (Fig. 4.3b). Thus, incomplete staining of L4-L6 and the optical opacity of cortical tissue modulates the balance of laminar contributions to the measured signal. Furthermore, given the difference between L2/3 and L5 in pairwise correlation strengths apparent in Figure 4.4b, VSDI measurements reflect an admixture of correlated, homogeneous responses from L5 neurons, and a diversity of both weakly correlated and anticorrelated responses in L2/3. The consequences are manifest in Figure 4.5f, where L5 underwent strong depolarization in the post-stimulus window while L2/3 tended to hyerpolarize, indicating differential, layer-specific roles during stimulus response. Analysis of the correlations between fractional VSDI signals also supports this conclusion, showing anticorrelated activity between superficial and deep layers (Fig. 4.5h).
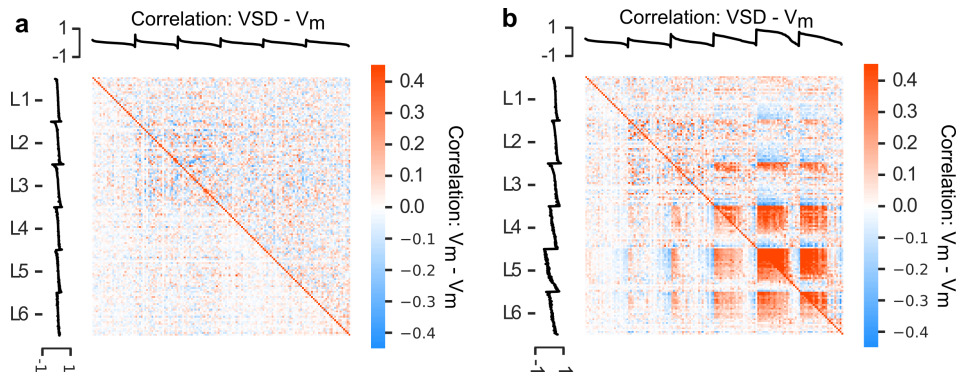
Figure 4.4 – **Pairwise V$_m$ Correlations**

a, Pairwise V$_m$ correlations between neurons (300 per layer) for spontaneous network activity. Upper triangle: correlations computed using thresholded traces (-55 mV). Lower triangle: correlations computed on raw traces including spikes. Top and left margins: V$_m$-VSDI correlations for each cell, sorted by strength within each layer (filtered and unfiltered, respectively). **b**, Same as in **a**, but for evoked activity (single stimulus, 60 contiguous TC fibers at NMC center)

4.2.2 Missing Inhibitory Signals During Evoked Activity

We also decomposed VSD fluorescence into excitatory and inhibitory fractions. For evoked trials, the excitatory component of the signal (>90%) underwent large deflections in the post-stimulus window, far outweighing inhibitory contributions (<10%) (Fig. 4.5i). Indeed, the inhibitory fraction remained small throughout both pre- and post-stimulus periods. This observation ran counter to expectation, as it is known that excitatory activity in healthy neocortex quickly recruits a mitigating inhibitory response, preventing runaway excitation (Fino and Yuste, 2011, Isaacson and Scanziani, 2011, Kapfer et al., 2007, Silberberg and Markram, 2007). We therefore analyzed the timecourse of mean membrane potential changes in the inhibitory populations of each layer, revealing that those in superficial layers were significantly hyperpolarized following stimulation, while those in deep layers were significantly depolarized (Fig. 4.5j,k). Since the dendrites of inhibitory cells tend to be spatially confined (see Fig. 2.1b), those located in deeper layers are unlikely to contribute appreciably to the VSDI signal as their morphologies do not extend to a height reachable by the dye and excitation light. Therefore, the VSDI signal only "sees" the contributions of hyperpolarized superficial inhibitory neurons.

4.3 Impacts of Sub- and Suprathreshold Neural Activity on VSDI Signals

It is thought that APs are too brief and too asynchronous to contribute substantially to the VSDI signal, despite causing large transient fluctuations in V$_m$ (Berger et al., 2007, Civillico and Contreras, 2012, Ferezou et al., 2006, Petersen et al., 2003b,a). This conclusion is partly based on simultaneous VSDI and single-cell patch-clamp recordings, of which spike-triggered averaging exposes the absence of individual AP waveforms from the VSDI signal (Ferezou

Figure 4.5 – **Signal Contributions by Layer and Cell Type**

a-b, Surface area contributions for each layer by depth. **a**, Microcircuit, for reference respecting relative layer positions and axis orientation. **b**, Left: raw (unscaled) neurite surface area profiles by depth for each layer (20 μm bins). Middle: depth-dependent scaling prefactors accounting for dye diffusion (solid black line) and light penetration (dashed black line). Solid blue line indicates product. Right: effective surface area profiles by depth for each layer (raw surface area b scaled by product of light attenuation and dye diffusion prefactors (solid blue line, middle panel), 20 μm bins). **c**, Spatially averaged VSDI signal (black) with fractional contribution of each layer (colored) for 1.5 seconds of spontaneous activity. **d**, Boxplot of fractional layer-wise contribution data in **c**, illustrating overall spread and polarity of each layer's contributions. **e**, Correlation matrix for all traces in **d**. **f**, Spatially averaged VSDI signal (black) with fractional contribution of each layer (colored) for 500 ms of evoked activity. Plot begins at -50 ms, stimulus delivered at 0 ms (dashed line). **g**, Same as in **c**, but for evoked activity. **h**, Same as in **d**, but for evoked activity. **i**, Fractional contributions of excitatory and inhibitory populations to overall VSDI signal, shown over a 50 ms second window spanning 25 ms pre- and 25 ms post-stimulus. **j**, Mean membrane potentials computed for inhibitory cell populations in each layer, plotted over the same time window as in **i**. **k**, Boxplots depicting the difference between pre- and post-stimulus membrane potentials for inhibitory cell populations in each layer. Boxplots in each panel were calculated using the 25 ms pre- and post-stimulus periods referred to in **i** and **j**, ******: $p < 0.0001$, paired sample t-test.
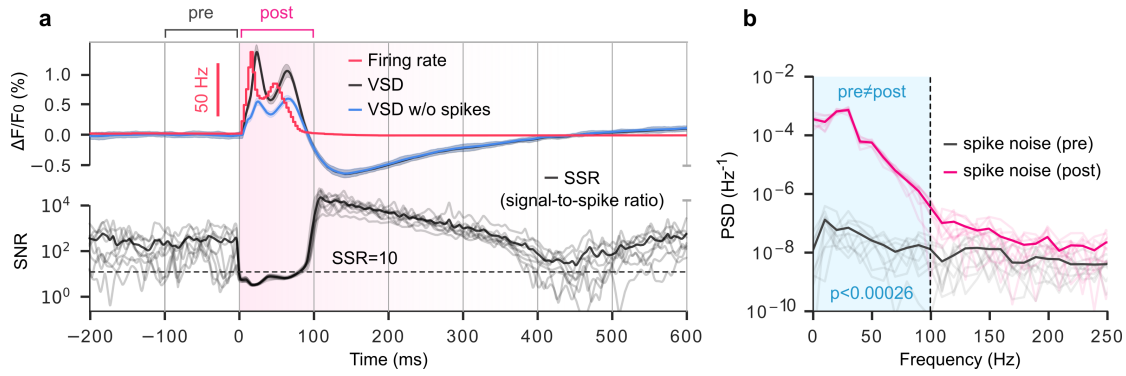
Figure 4.6 – **Detectability of Spiking Activity**

a, Top: Firing rate (red), VSDI (black), and VSDI computed excluding spikes (membrane potentials thresholded at -55 mV, blue) for 200 ms of spontaneous activity followed by 600 ms of evoked activity. Bottom: Signal-to-spike ratio (SSR). Dashed black line: signal-to-spike ratio = 10. **b**, Power spectral density of spike noise computed for 100 ms pre-stimulus window (black), and 100 ms post-stimulus window (magenta). Blue shaded box indicates frequencies for which pre- and post-stimulus SSR are significantly different. Dashed black line indicates frequency at which pre-stimulus noise and post-stimulus SSR are no longer meaningfully different (paired t-test, significance threshold = 0.01, adjusted to 2.6×10^{-4} for multiple comparisons using Holm-Bonferroni correction).

et al., 2006). However, such experiments leave open the possibility that large *volleys* of spiking activity occurring within a narrow time window could still have a measurable influence. To isolate the effects of spiking on the optical response, we ran our VSDI pipeline on spike-filtered (-55 mV threshold) neurite compartment voltage data and compared with unfiltered data (Fig. 4.6a, top). Assuming the null hypothesis that VSDI primarily reflects subthreshold activity, we considered any difference between the raw and spike-filtered signals as "noise" due to spikes. This allowed us to calculate a signal-to-spike ratio (SSR), defined in analogy to the signal-to-noise ratio (SNR), as the squared quotient of the root mean square amplitudes of the unfiltered signal and spiking component. That is:

$$A = \sqrt{\frac{1}{\Delta t} \int_{t_0}^{t_1} \text{VSD}^2(t)\, dt} \tag{4.3}$$

$$\text{SSR} \triangleq \left(\frac{A_{\text{raw}}}{A_{\text{raw-filt}}} \right)^2 \tag{4.4}$$

which we represented as a continuous variable by binning into 40 ms intervals with overlapping windows. Conservatively, we estimate that typical VSDI experiments have an SNR of 10 (Civillico and Contreras, 2005, Grinvald et al., 1999, Jin et al., 2002, Lippert et al., 2007, Tsau et al., 1996, Zhou et al., 2007). Therefore, when SSR is less than 10 (i.e., less than the empirical SNR of typical experiments), the component of the VSDI signal due to spikes is larger than contamination due to other noise sources, and in principle could be detected. Although SSR did dip slightly below our estimated detectability threshold during the post-stimulus window, this

is unlikely to be meaningful in most laboratory settings. However, in cases where exceptionally high SNR is achieved, information regarding the spiking component of the VSDI signal may become relevant. Therefore, we sought to understand how the frequency content of "spike noise" is affected by stimulation (Fig. 4.6b). A power spectral density analysis of "spike noise" immediately pre- and post-stimulus showed that the frequency content differs significantly only below ~100 Hz, with lower frequencies exhibiting greater divergence. Measurements sensitive enough to detect a spiking contribution to the VSDI signal therefore would only contain spike-related information below this frequency cutoff and would be dominated by low frequency components. We are careful to distinguish here between the contributions of individual spikes, which are not detectable in mesoscale recordings as reported previously, and the aggregate influence of population spiking, which adds a small DC offset (and low frequency oscillations) to the VSDI signal, as described above.
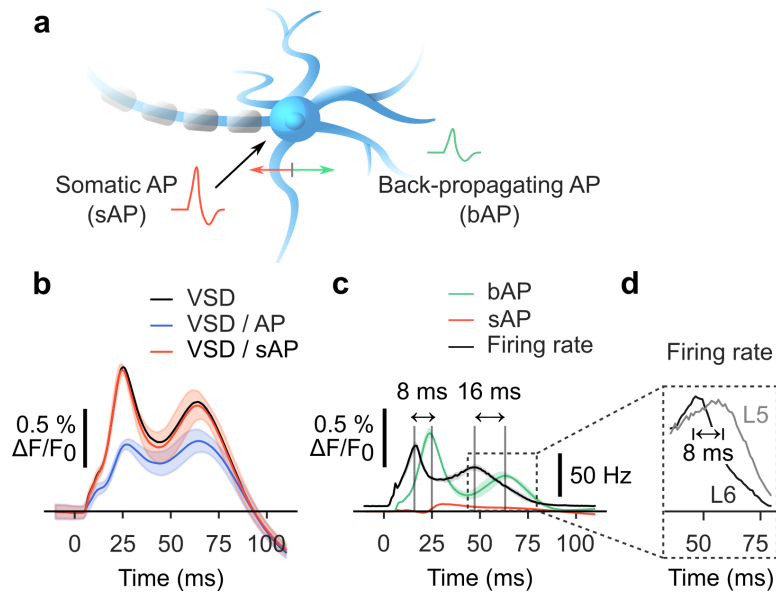
Figure 4.7 – **Forward- and Backward-Propagating Action Potentials**

a, Schematic illustrating forward- and backward-propagating APs. Red: APs occurring at the soma/axon initial segment (sAP). Green: back-propagating APs occurring in dendritic arbors (bAP). **b**, Time domain comparison of filtered VSDI signals. Black: full signal, no filtration. Blue: VSDI signal computed with thresholded V_m (-55 mV), all spikes excluded. Red: VSDI signal computed with thresholded V_m (-55 mV), only spikes in somatic compartments excluded. **c**, Comparison of VSDI signal contributions by bAP (green) and sAP (red), with firing rate overlay (black). **d**, L6 and L5 mean firing rates during time window in dashed box in **c**.

A detailed account of the cellular sources of the spike-associated VSDI signal fraction was also made possible using *in silico* VSDI. It is well known that APs initiated at the axon initial segment (AIS) don't only propagate orthodromically along the axon towards postsynaptic targets, but also back up through the dendritic arbor (Stuart and Sakmann, 1994, Gulledge et al., 2005) where they are thought to play a role in mediating synaptic integration (Grewe et al., 2010, Koester and Sakmann, 1998) and plasticity (Colbert, 2001, Kuczewski et al., 2008). Thus, spike waveforms influencing the VSDI signal are potentially of either (or both) somatic or dendritic

origin. To assess the relative contributions of these AP types to the spike-associated VSDI fraction, we computed a VSDI signal based on four versions of the V_m simulation output: 1) full, unadulterated V_m data, 2) spike-filtered V_m data (all-compartments), 3) somatic spike-filtered V_m data (somatic compartments only), and 4) dendritic spike-filtered V_m data (dendritic compartments only). Unsurprisingly given their limited surface area, somatic compartments add relatively little to the overall signal, as demonstrated by the correspondence between the black (VSDI) and red (VSDI without somatic spikes) curves in Figure 4.7b. Moreover, we note that there is a delay between the L5 firing rate and the back-propagating AP (bAP)-related component of the VSDI signal, which manifests as an 8 ms lag for the first, and a 16 ms lag for the second set of peaks (Fig. 4.7c). An 8 ms delay is consistent with a study by Larkum et al. (1999), in which a multielectrode recording protocol was used to investigate the effects of current injections on dendritic Ca^{2+}-dependent APs in L5 PCs in P28-P58 rat somatosensory cortex. Na^+-APs were evoked with threshold injection of current at the soma, and followed by paired current injection at a dendritic site near the apical tuft (700 μm from the soma). It was found that a delay of 7 ms between the two injections of current was optimal for eliciting a dendritic Ca^{2+}-AP (Larkum et al., 1999), which we interpret to represent an estimate for the time constant associated with back-propagation of APs through the apical tuft. Regarding the second delay of 16 ms, we speculate that the second activity peak is the result of a bottom-up cascade of activity beginning in L6 and L5, and propagating upwards through the NMC column (Fig. 4.3d, spike raster). Since L6 makes almost no fractional contribution to VSD fluoresence (see Section 4.2), the lag is doubled to account for a monosynaptic delay to L5 followed by back-propagation up the apical trunks of L5 cells. Comparing the spike rate time histograms of neurons in L6 and L5 showed that the second post-stimulus peak in L6 precedes that in L5 by ~8 ms (Fig. 4.7d).

4.4   VSDI Two-Point Discrimination

It is important to precisely articulate what is meant by "resolution" in the context of VSDI, where the term may be afflicted by conceptual overload. For example, the classical definition of lateral optical resolution refers to the minimum separation between two point sources of light for which their "Airy disks" (disk-like diffraction patterns) can be distinguished (Wilson, 2016). This distance is a function of the refractive index of the media surrounding the points, the wavelength of photons being imaged, and the size of the aperture through which the light passes. Alternatively, in a digital system, one may loosely refer to the "resolution" as the number of pixels on a detector's surface. In the case of VSDI, even assuming infinitely precise spatiotemporal resolution in the imaging system, one must still confront the fundamentally confounded nature of the signal itself. Since VSDI pixels are the sum of electrical activity in many neural compartments, what would it mean to "distinguish" between point sources? Even a point-like source of signal would contain information from hundreds of cells, and be scattered as it passed through out-of-plane tissue. Here, we propose a complementary, functional definition of resolution based on a two-point discrimination task. Specifically, we

consider the capacity of VSDI to distinguish between two spatially displaced presentations of an otherwise identical point-like stimulus. This definition of resolution therefore includes all forms of information loss in our VSDI model at once, and suggests an upper bound on the spatial information content of laboratory VSDI experiments (or a lower bound on "functional" resolution). We proceeded by simulating multiple trials (n=25) of localized, point-like stimula-
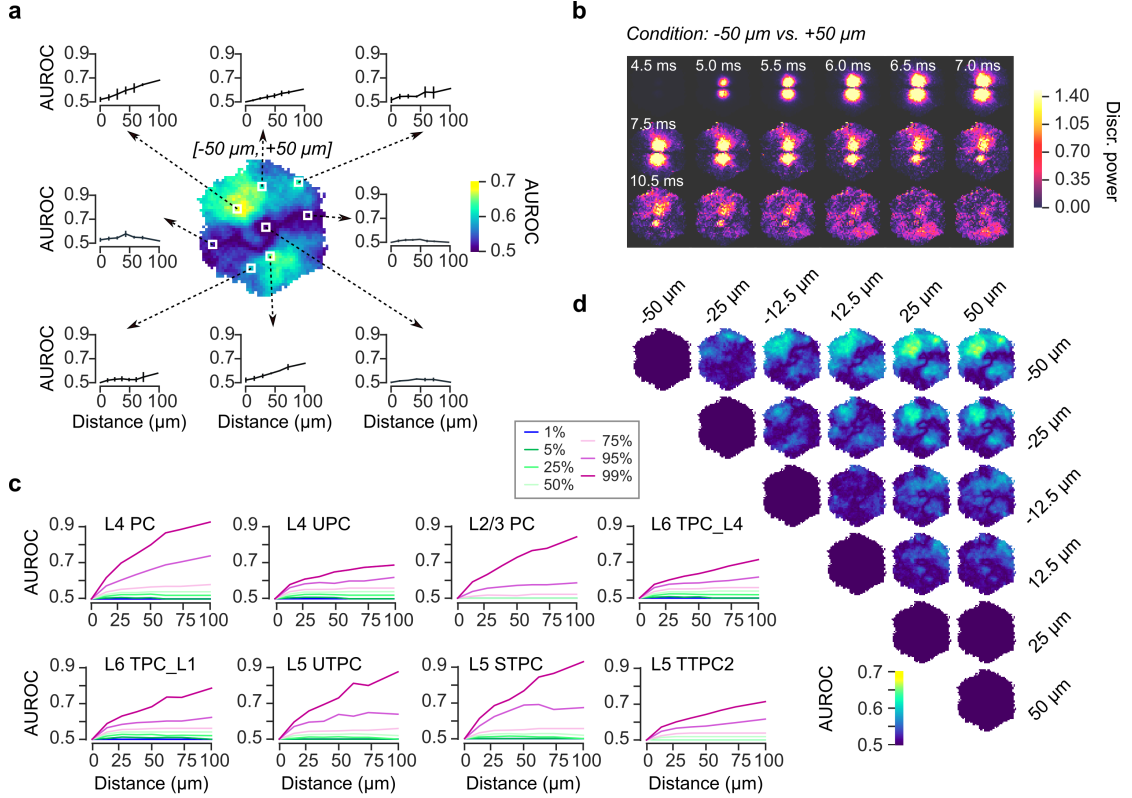
Figure 4.8 – **VSDI Two-Point Discrimination.**

Receiver operating characteristic (ROC) analysis and discrimination power of VSDI pixels. ROC was computed by varying the significance threshold for rejection of the null hypothesis that the two pools of time series data for a given pixel (corresponding to two stimulus locations) were drawn from the same distribution. **a**, Center: Summary map of VSDI two-point discrimination for the condition (-50 μm,+50 μm), i.e. 100 μm separation between stimuli. Pixel values correspond to mean AUROC scores. Surrounding plots: AUROC score as a function of increasing stimulus separation at several pixel locations indicated by white boxes. Final value in plots (100 μm) corresponds to color of associated pixel on map. **b**, Individual movie frames for condition (-50 μm,+50 μm); pixels are the negative log p-value of the null hypothesis that the respective values for the two stimulus locations come from the same distribution ("discrimination power"). **c**, AUROC scores computed using spike trains of cells in various neuron subpopulations as a function of increasing stimulus separation. Colors in legend indicate percentile of discrimination capacity within each subpopulation. **d**, Matrix of AUROC score maps for each combination of stimulus locations.

tion in the NMC (one AP delivered to 5 adjacent TC projection fibers), for increasing distances from the geometrical center, repeated fives times at intervals of 50 ms. Stimuli were delivered to locations at -50 μm, -25 μm, -12.5 μm, 12.5 μm, 25 μm, and 50 μm along the z-axis (vertical axis when NMC's surface is viewed from above). Next, we calculated the VSDI image stacks corresponding to each stimulus condition, and computed several metrics for comparing the

discrimination power of indidivdual VSDI pixels.

To obtain a time-resolved measure of the capacity to distinguish between stimuli, for each combination of two stimuli, for each VSDI pixel, and for each timestep, we used a Wilcoxon rank sum test to compute the p-value of the null hypothesis that the data (pooled over n=25 trials) associated with the different stimulus positions came from the same distribution. Building on this calculation, we defined the "discrimination power" of a given pixel for a particular stimulus pairing as the negative common logarithm of the p-value of the null hypothesis stated above. For example, Figure 4.8b illustrates a map of discrimination power for the first ~13 ms following stimulation, comparing delivery at z=-50 μm and z=+50 μm. Two salient spots of high discrimination at $\pm$ 50 μm emerge at 5 ms post stimulus, and gradually fade by 13 ms, coinciding with the initial appearance and subsequent dispersal of activity in the underlying VSDI datasets. As expected, pixels directly above innervating TC fibers exhibit the strongest discrimination power in the milliseconds immediately following stimulation, since activity is localized to these points in that time window. Furthermore, a horizontal band of low discrimination power is visible along the axis of symmetry dividing the two stimulus locations, since pixels there undergo a similar activity trajectory for either stimulus condition.

In addition, we carried out a receiver operating characterstic (ROC) analysis as a complementary, time-compressed means of quantifying discrimination performance. The ROC curve of a binary classifier is the plot of true positive rates (TPR) against false positive rates (FPR) as a function of classification threshold. Often, the definite integral of the this curve (area under the reciever operating characteristic- AUROC) is calculated, producing a condensed one-dimensional index (Altman and Bland, 1994). To this end, we computed p-values for each VSDI pixel and time step in the manner described above, and observed how varying the significance threshold altered the proportion of total true positive rejections of the null hypothesis for a given stimulus pairing. As there were 25 trials per stimulus location, we formed all $\binom{50}{2}$ combinations of time series data in each pixel, and evaluated whether the p-value produced by comparing the two pools of VSD fluorescence data for any given combination of trials was above or below the significance threshold in consideration. Since each of the $\binom{50}{2}$ pairings comprised either two trials from different stimulus locations, or two from the same location, p-value-based rejection of the null hypothesis corresponded to either a true positive, or false positive result, respectively. Thus, we were able to associate each pixel to a TPR and FPR for each significance threshold. Finally, integrating the ROC curves thus produced yielded AUROC scores for each pixel (Fig. 4.8a,d). Unsurprisingly, this analysis showed that greater separation between stimulus locations generated increasingly differentiated AUROC maps (Fig. 4.8d). Inspection of individual pixels (Fig. 4.8a) further demonstrated a spatially distributed diversity of responses to the presentation of stimuli at different locations. Intriguingly, an interlocking whirl of regions with high and low AUROC was apparent at the center of many discrimination maps, with an increasing trend towards prominence for larger stimulus separations (Fig. 4.8d). Additionally, the strongest pixel predictors of stimulus location were not located directly over the TC input (as was the case for discrimination power), but rather towards the periphery of the NMC surface. This indicates that a temporally resolved measure

of discrimination (Fig. 4.8b) fails to fully capture the ongoing dynamics of neural interactions that ultimately shape a differentiated response to one stimulus location or another. While in the milliseconds following stimulation it is logical that a strong local response dominates any difference between responses to presentations of different stimuli, as the response spreads over time, an integrated measure of discrimination (AUROC) reveals that pixels further from the stimulus location play a larger role, likely due to anisotropies in the spatial arrangement of, and connectivity among neurons.
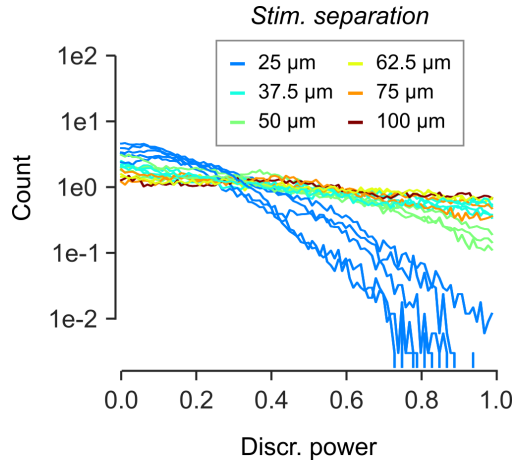
Figure 4.9 – **Discrimination Power Count Histogram**

Pixelwise count histogram of discrimination power for varying stimulus separation distances. Each distance is depicted with multiple curves since several distinct combinations of stimulus location correspond to the same separation interval.

For reference, we also computed AUROC scores using spike trains in various neural m-types (see Section 2.1). Our classification method in this case considered whether the spike count for each neuron in the 250 ms post-stimulus window crossed an empirically determined threshold, but was otherwise identical to procedures already described. Additionally, we created a stratified set of discrimination capacities within each subpopulation by sorting individual cells of that m-type into discrimination percentiles. Our results show that the spiking activity of most neurons in all subpopulations considered is insufficient for discriminating between stimulus locations, even at separations up to 100 μm (Fig. 4.8c). However, at around the 95th percentile, neurons in each population exhibit a sudden and dramatic improvement in discrimination capacity, implying that a small handful of cells are chiefly responsible for the statistically meaningful differences in spiking activity between stimulus locations. This implies that individual VSDI pixels better capture the relevant differences between various stimulus configurations than spike rates in populations of cells, since the activity of rare, high discrimination capacity individuals would be washed out in the aggregate. Also, it highlights the importance of subthreshold activity in shaping the cortical response to afferent inputs.

Last, we plotted a count histogram of pixels by discrimination power for a range of stimulus separations (Fig. 4.9). We note that several distinct combinations of stimulus positions result

in the same separation interval, giving rise to multiple curves per inter-stimulus distance. Immediately, one observes that there is a paucity of high discrimination power pixels for a stimulus separation of 25 μm, and a marked jump in power to the next separation. We interpret this finding as a rough measure of spatial resolution in the previously described sense of functional capacity to discriminate between distinct stimulus positions. Thus, we assert that *in silico* VSDI has a "functional resolution" greater than 25 μm, and predict that this statement also holds true *in vivo*, since our model is an idealization, and likely captures fewer sources of noise than are present in a laboratory setting.

4.5   VSDI Signals Anticorrelate with Population Firing Rate

In light of the unanticipated observation that spiking activity precedes VSDI deflections during evoked activity (Fig. 4.2c,d), and the interpretation of VSDI as a measure of subthreshold V_m, we were motivated to inspect the relationship between population firing rates and mean V_m in simulations of spontaneous activity. Surprisingly, this revealed a strong inverse association (Pearson correlation coefficient of -0.86, R^2 value of -0.83) between the two at a temporal lag of ~23 ms, with spikes preceding V_m (Fig. 4.10a,b). The relationship between the VSDI signal and spiking exhibited a similar, albeit weaker trend, as expected in view of the correspondence between mean V_m and VSD fluorescence (Fig. 4.10c). Thus, we sought an interpretable explanation for this phenomenon in terms of population dynamics. To this end, mean-field theory was a natural choice as it provides an analytical framework for understanding the dynamics of neural populations, where each population is represented in aggregate as a single unit (Muller et al., 2007, Rudolph et al., 2004, Zerlaut et al., 2018). Since VSDI reports a summary of V_m across many neurons, we began by considering the relationship between mean V_m and conductance. Following the approach of Dorn and Ringach (2003), Kuhn et al. (2004), Muller et al. (2007), and Zerlaut et al. (2018), the membrane potential of a leaky integrate-and-fire neuron evolves according to:

$$C_m \frac{dV_m}{dt} = g_e (E_e - V_m) + g_i (E_i - V_m) + g_l (E_l - V_m) - I_{\text{clamp}} \tag{4.5}$$

$$\frac{dg_e}{dt} = -\frac{1}{\tau_e} g_e + q_e S_e(t) \tag{4.6}$$

$$\frac{dg_i}{dt} = -\frac{1}{\tau_i} g_i + q_i S_i(t) \tag{4.7}$$

where C_m is membrane capacitance, g_e, g_i, and g_l are excitatory (AMPA and NMDA), inhibitory (GABA) synaptic conductance, and leak conductance, respectively, E_e, E_i, and E_l are the respective reversal potentials, τ_e and τ_i are the excitatory and inhibitory time constants, q_e and q_i are the quantal synaptic conductance increases, and S_e and S_i are presynaptic spike trains (Dorn and Ringach, 2003, Kuhn et al., 2004, Muller et al., 2007, Zerlaut et al., 2018). The

term I_{clamp} represents a depolarizing current injected at the soma to compensate for missing external inputs to the NMC (Markram et al., 2015).

Equation 4.5 above may be rearranged to yield an "effective" membrane potential (V_{eff}), which approximates the population mean as a function of synaptic bombardement (Rudolph et al., 2004, Zerlaut et al., 2018):

$$V_{\text{eff}} = \frac{g_e E_e + g_i E_i + g_l E_l - I_{\text{clamp}}}{\sum_k g_k} \tag{4.8}$$

Substituting this quantity into equation 4.5 and rearranging, we obtain:

$$\tau_{\text{eff}} \frac{dV_m}{dt} = V_{\text{eff}} - V_m \tag{4.9}$$

$$\tau_{\text{eff}} = \frac{C_m}{\sum_k g_k} \tag{4.10}$$

We note that equation 4.9 has the form of an RC low-pass filter, with a cutoff frequency given by $\frac{1}{\tau_{\text{eff}}}$. Therefore we expect V_{eff} to be a reasonable approximation of V_m, provided that the frequency of characteristic fluctuations in V_{eff} don't exceed $1/\tau_{\text{eff}}$. Intuitively, V_{eff} may be thought of as a noisy short-term prediction of V_m. If one imagines a scenario in which conductances are static, V_{eff} is the value V_m will eventually converge to by exponential relaxation dynamics. The above equations hold true both for a single neuron, and on average across a population of neurons. Furthermore, if S_e and S_i are inhomogeneous Poisson processes, then in expectation, these terms in equations 4.6 and 4.7 are replaced with time-varying mean firing rates ν_e and ν_i (Muller et al., 2007). Thus, in expectation:

$$\langle V_{\text{eff}} \rangle = \frac{\langle g_e \rangle E_e + \langle g_i \rangle E_i + \langle g_l \rangle E_l - \langle I_{\text{clamp}} \rangle}{\sum_k \langle g_k \rangle} \tag{4.11}$$

$$\frac{d \langle g_e \rangle}{dt} = -\frac{1}{\tau_e} \langle g_e \rangle + q_e \nu_e \tag{4.12}$$

$$\frac{d \langle g_i \rangle}{dt} = -\frac{1}{\tau_i} \langle g_i \rangle + q_i \nu_i \tag{4.13}$$

We proceeded in the calculation of V_{eff} by isolating firing rates in excitatory and inhibitory subpopulations; numerical integration of equations 4.12 and 4.13 allowed us to analytically relate mean firing rates to V_{eff}. Experimental evidence supports the notion that excitatory and inhibitory synaptic currents are tightly balanced in healthy cortical tissue both in the resting state and during sensory processing (Denève and Machens, 2016, Sengupta et al., 2013, Zhou and Yu, 2018). Tight balance of synaptic currents implies that: 1) excitatory and inhibitory firing rates fluctuate synchronously, and 2) inhibitory conductances are greater

than excitatory (Sengupta et al., 2013). Consistent with this view, we observed that excitatory and inhibitory firing rates (and thus also excitatory and inhibitory conductances) were highly correlated (Fig. 4.10d). Additionally, inhibitory conductances were larger than excitatory both in terms of mean and variance, with a $\langle g_i \rangle$ to $\langle g_e \rangle$ ratio of ~9. Despite the
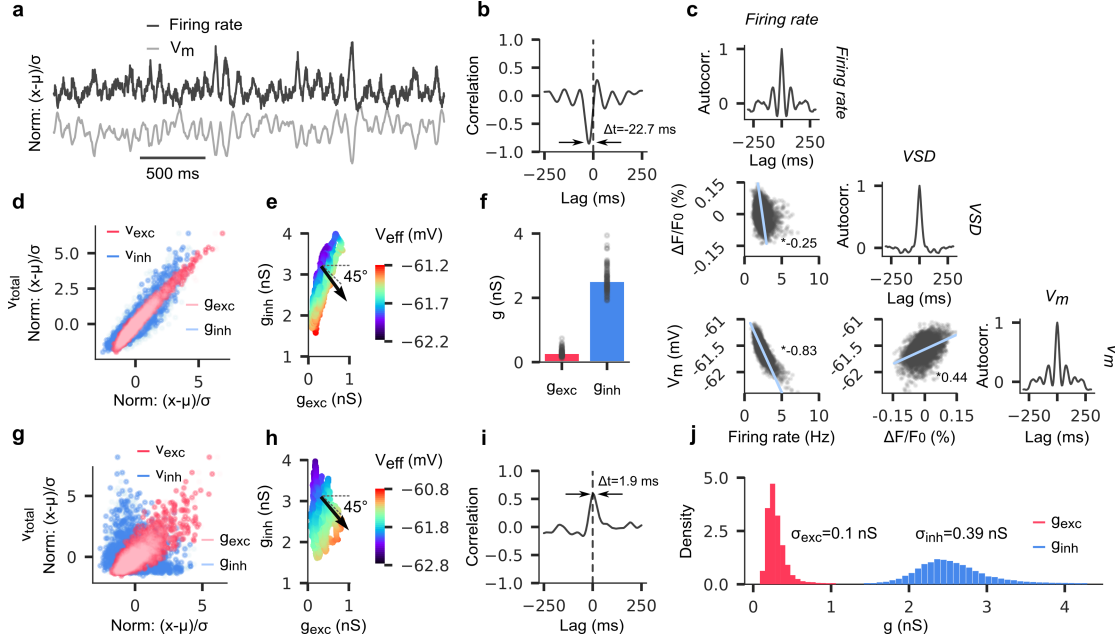
Figure 4.10 – **Mean V_m Anticorrelates with Population Firing Rate**

a, Population firing rate (top, dark gray) and mean membrane potential (bottom, light gray); normalized units. Time-shifted by 22.7 ms to align signals at peak correlation. **b** Cross-correlogram of population firing rate and mean membrane potential. **c**, Lower triangular scatter plot matrix depicting correlations between firing rate, VSDI, and membrane potential. Starred values indicate R-squared values for linear fit. Diagonal shows autocorrelation. **d**, Scatter plot of inhibitory and excitatory conductances and firing rates (light blue, pink, blue, red, respectively) against population firing rate; normalized units. **e**, Scatter plot of excitatory vs. inhibitory conductances. Color reflects corresponding mean-field-predicted membrane potential at each point in plot. Black arrow indicates directional gradient (increasing membrane potential). **f**, Bar plot of mean excitatory and inhibitory conductance values, with individual data points overlaid in black. **g**, Same as in **d**, but for decoupled network (i.e., each cell receives only pre-recorded synaptic inputs, and does not influence the network with its output). **h**, Same as in **e**, but for decoupled network. **i**, Cross-correlogram of population firing rate and mean membrane potential for decoupled network. **j**, Histogram of conductance values in **f**. Normalized so that AUC = 1 for both cell type populations.

preponderance of inhibitory conductance, we determined that V_{eff} was affected roughly in equal proportion per unit change in either conductance type (Fig. 4.10e). Therefore, given its much higher variance, change in inhibitory conductance was the primary driver of V_m fluctuations. Finally, since network balance requires high correlation between $\langle g_e \rangle$ and $\langle g_i \rangle$, it follows that mean V_m, and by extension the VSDI signal, anticorrelate with total firing rate. Next, to confirm our supposition that network balance is a requirement for the aforementioned effect, we performed a series of simulations of spontaneous activity in which network connections (and thus recurrent connectivity) were disabled (Fig. 4.11).
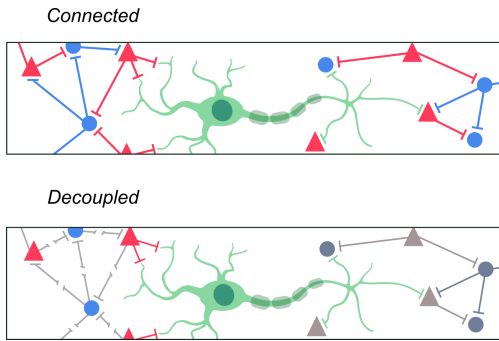
Figure 4.11 – **Connected vs. Decoupled Networks**

Top: schematic illustrating a normally connected network (red triangles: inhibitory cells, blue circles: excitatory cells), as seen from the perspective of a single, representative neuron (green) embedded in the network. Bottom: same as above, but for a neuron embedded in a decoupled network, where each cell receives prerecorded synaptic inputs (and no other inputs), and does not influence the network with its output.

Instead, each neuron was fed excitatory and inhibitory input spike trains recorded from previous simulations of the same microcircuit. Importantly, the excitatory and inhibitory inputs were derived from simulations with different random seeds, abolishing the coupling between excitation and inhibition (Fig. 4.10g), but preserving the distributions of $\langle g_e \rangle$ and $\langle g_i \rangle$, and therefore also their relationship to V_m (Fig. 4.10h); indeed, $\langle g_i \rangle$ remained tightly anticorrelated with V_m. However, the removal of recurrent network connections led to a reversal of the relationship between spiking output and V_m (Fig. 4.10i), as spikes in each neuron were no longer correlated with presynaptic inputs. Therefore, we conclude that VSDI potentially contains important and underappreciated information regarding population firing rates in balanced networks.

4.6 Extrinsic Synaptic Inputs Decrease the Synaptic Conductance Ratio

In biological cortex, cellular assemblies are subject to extensive innervation by intracortical and thalamocortical projections, and by long-range projections emanating from white matter tracts (DeFelipe et al., 2002, Gil et al., 1999, Kawaguchi, 2017, Tomioka et al., 2005). Estimates of synapse counts in rat hindlimb somatosensory cortex have been reported as high as 18,000 per neuron (DeFelipe et al., 2002). Because placement of synapses in our microcircuit is constrained by the anatomical apposition of dendrites and axons (Markram et al., 2015, Reimann et al., 2015), only the formation of local synapses (~1,145 synapses per neuron, on average) is possible. Thus, each neuron in the NMC receives a tonic injection of depolarizing current (I_{clamp}) at its soma to compensate for missing excitatory inputs. This current is the sum of a DC component, which was computed as a percentage of rheobase (the minimal step current required to depolarize the cell to AP threshold), and a Gaussian noise component of small amplitude (Markram et al., 2015). Expressed as a percentage of rheobase, I_{clamp} is held constant over the entire circuit, though absolute amplitudes vary for each neuron. As a consequence, average conductance values are more than one order of magnitude smaller than those reported *in vivo* ($g_i = 70.67 \pm 45.23$ nS, $g_e = 22.02 \pm 37.41$ nS, $g_i/g_e = 14.05 \pm 12.36$, as measured in ketamine-xylazine anesthetized feline cortex during brainstem stimulation (Rudolph et al., 2005); cf. Fig. 4.12f), with concomitant reductions in variance. We were curious to understand how the injection of current could affect the results
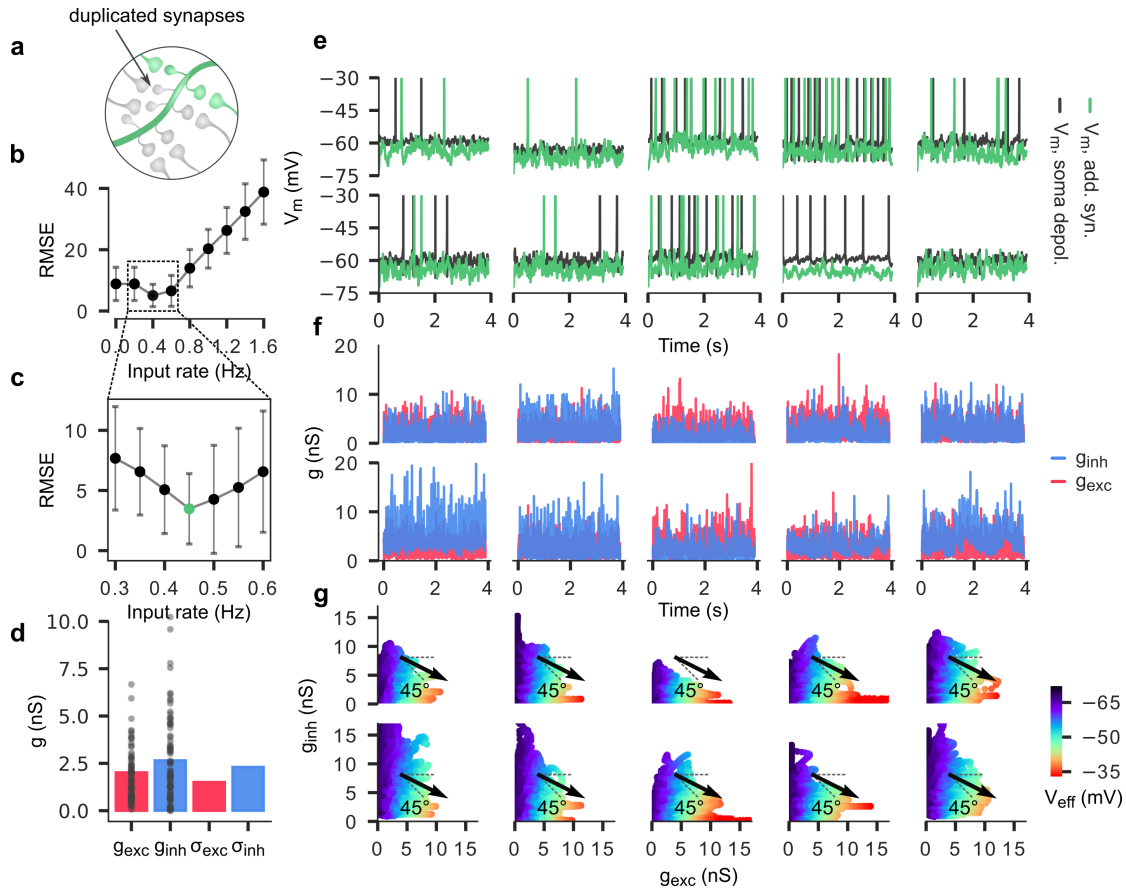
Figure 4.12 – **Effects of Long-Range Excitatory Synaptic Inputs**

a, Schematic showing duplication of excitatory synapses. Five identical, spatially co-located copies of each excitatory synapse were added to 10 randomly selected L5 PCs in the microcircuit. **b**, Simulated Poisson inputs were generated at different Poisson rates to evoke postsynaptic spiking. Poisson rates of the added synapses were varied to minimize the RMSE in the difference between the spiking rate of the target postsynaptic cell with and without additional synapses (but with somatic depolarization). **c**, Expanded view of **b**, for input Poisson rates between 0.3 and 0.6 Hz. Minimal RMSE indicated in green (0.45 Hz). **d**, Mean excitatory and inhibitory synaptic conductances and conductance standard deviations for all 10 neurons (pooled) for 4 seconds of spontaneous activity. **e**, Voltage trace overlays for each of the 10 neurons for 4 seconds of spontaneous activity. Green: added synapses (0.45 Hz), no somatic depolarization. Black: somatic depolarization, no additional synapses. **f**, Excitatory and inhibitory conductances (red and blue, respectively) for each of the 10 neurons for 4 seconds of spontaneous activity with added synapses at 0.45 Hz. **g**, Scatter plot of excitatory vs. inhibitory synaptic conductances. Color reflects corresponding mean-field-predicted effective membrane potential at each point in plot. Black arrow indicates directional gradient (increasing membrane potential).

of the previous section, and network dynamics more broadly. To this end, we attempted to replicate naturalistic conditions through the simulation of additional synaptic inputs. Assuming that most inhibitory connections occur locally (< 500 μm) (Fino and Yuste, 2011, Karnani et al., 2014, McDonald and Burkhalter, 1993), we duplicated existing excitatory synapses (5x per synapse, Fig. 4.12a) on a small handful of L5 PCs (n=10), and set I_{clamp} to zero. Since it is known that neurons form multisynapse connections (Deuchars et al., 1994, Frick et al., 2008, Markram et al., 1997, Silberberg and Markram, 2007, Silver et al., 2003, Wang et al., 2002), duplicated synapses for each neuron were randomly partitioned into groups that received identical input, representing a single connection. Group size was drawn from the distribution of synapses per connection for that cell type. Synaptic inputs consisted of spike trains generated by a homogeneous Poisson process with rate λ_{ext}, which we varied incrementally until the root-mean-square error between the number of spikes in a 4 second interval in the new (added synapses) and old (somatic depolarization) simulations was minimized (Fig. 4.12b,c). We observed that for additional Poisson inputs at the optimal rate (0.45 Hz), mean excitatory conductance increased by a factor of ~7, while inhibitory conductances remained largely unchanged (~5% increase). However, conductance standard deviation changed considerably for both excitatory and inhibitory channels, increasing by a factor of 14.3 and 5.8, respectively (Fig. 4.12d). We also examined the relative influence of excitatory and inhibitory conductances in determining V_m fluctuations and found that the increased variance in g_e corresponded to relatively more influence than g_i on the trajectory of V_m (Fig. 4.12g). However, the addition of synapses did not alter the previous observation that a unit change in either g_e or g_i affected V_m equally. In summary, a five-fold increase in excitatory synapses with Poisson inputs in the absence of somatic depolarization tended to increase the mean of g_e and its influence on V_m, and dramatically increased the variance of both g_e and g_i.

5 Discussion

We constructed a bottom-up, biophysically detailed model of VSDI in a digital reconstruction of rodent neocortical microcircuitry to relate cellular anatomy and physiology to membrane potentials at the mesoscale, and to seek novel insights regarding the dynamics of cortical processing. As a first step, we considered VSDI measurements of evoked responses in our model, and found that they were qualitatively and quantitatively similar to analogous experiments *in vivo*. Next, we used our model to deconstruct the VSDI signal into laminar and cell type contributions, revealing context-dependent, differentiated roles for layers 2/3 and 5. We also examined the influence of spiking activity, and found that while individual spikes are not reflected in VSDI data, large volleys of semi-synchronous spikes could slightly affect measurements. In addition, a two-point discrimination test of "functional" resolution showed that cortical VSDI is unlikely to be able to resolve point-like inputs separated by less than 25 μm. Furthermore, our model led us to the surprising observation that the VSDI signal is anticorrelated with population firing rate, peaking at a lag of ~23 ms. Using a mean-field approach, we discovered that this is due to the predominance of inhibitory conductances, which are coupled to population spiking via recurrent connections. Finally, we considered the effects of including additional excitatory synapses to compensate for missing non-local innervation, and found that a Poisson model of spiking inputs led to increased variance in values of conductance. Several details pertaining to the above results merit further discussion.

5.1 What's in a Voxel?: Dissecting the Neuropil and the Role of Axons

In Section 4.2, we calculated a depth-dependent profile of the total surface area contributed by neurites belonging to cells in each cortical layer. Quantifying surface area in this way allowed us to predict which layers (i.e. neuron populations grouped by soma location) were most and least important in driving VSDI fluctuations (Fig. 4.5b). Similarly, one might inquire how surface area is distributed among the various neurite types (soma, axon, dendrite) throughout the neuropil (the axons, dendrites, soma, and glial cell processes that constitute the neural

tissue), specifically with regards to presence of axonal arbors[1]. Though each reconstructed morphology in the NMC contains the full complement of axonal, dendritic and somatic compartments, non-axon initial segment (AIS) axonal compartments are excluded at simulation runtime to conserve resources. This is possible since axo-axonal connections are thought to be mediated by: 1) Chandelier cells which form synapses exclusively on the AIS (Somogyi, 1977, Woodruff et al., 2010), and 2) somatostatin-expressing cells which innervate somata, dendrites, spines, and the AIS (Gonchar et al., 2002), implying that non-AIS intracortical axonal arbors merely propagate signal from one point in space to another with relatively minimal disturbance. Thus, AP waveforms originating in the AIS may be broadcast to axon terminals following a suitable delay calculated from axonal path length and known conduction velocities.
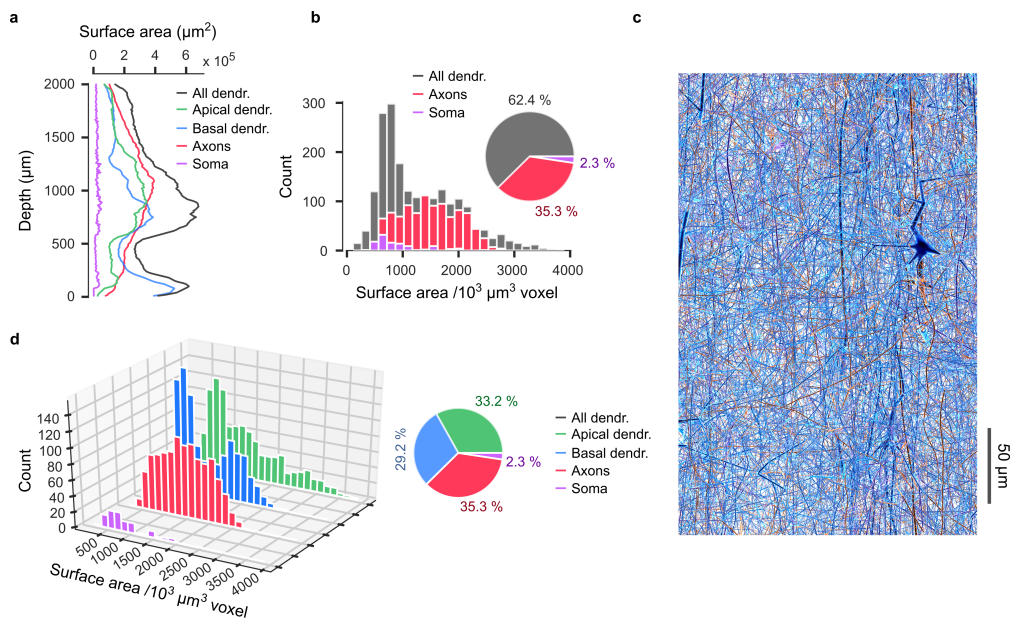
Figure 5.1 – **Neuropil Composition**

a, Distribution of surface area by depth for somatic, axonal, and dendritic compartments. Total Surface area calculated by summing in 10 μm increments along the y-axis. **b**, Count histogram of surface area by compartment type for 1000 randomly sampled 10^3 μm^3 voxels throughout the NMC. Inset: pie chart showing percentages of surface area by compartment type over all voxels sampled. **c**, Visualization of a 200 x 300 μm section of neuropil. *Image courtesy of BBP.* **d**, Same as in **b**, but with a distinction made between apical and basal dendritic compartments.

However, the exclusion of axonal compartments could curtail the accuracy of our VSDI model, since they are a potentially relevant source of signal. To address such concerns, we characterized the composition of the neural tissue within each voxel (1000 μm^3 cube of tissue; see Section 3.2.1) in terms of the surface area contributed by axonal, somatic, and dendritic compartments (Fig. 5.1). We found that axonal compartments constitute a non-negligible

---

[1]N.B. The version of the NMC utilized here does not contain glia. See Section 5.6 for a discussion of the influence of glial activity on VSDI signals.

fraction of the neuropil, representing ~35 % of the total membrane surface area (Fig. 5.1b,d), with a peak at the boundary between layers 4 and 5 (Fig. 5.1a). However, this concern must be viewed in light of two important countervailing considerations. First, electron microscopy (EM) serial reconstructions have revealed substantial, although patchy, myelination along the axonal arbors of both GABAergic and pyramidal neurons in the neocortex (Tomassy et al., 2014, Micheva et al.). In particular, Tomassy et al. (2014) find that up to 60 % of the reconstructed axons of L5 and L6 PCs may be myelinated. Since the presence of myelin sheathing would prevent voltage-sensitive probes from binding to the cell membrane, these compartments would not contribute to the VSDI signal. Second, in contrast to dendritic processes in which PSPs constantly occur as a result of synaptic bombardment, axons beyond the AIS do not receive synaptic input. Thus, each axonal compartment sees only a brief deflection in V_m as an AP waveform travels along the cable. Since it is well established empirically that APs do not contribute to VSDI signals (Berger et al., 2007, Civillico and Contreras, 2012, Ferezou et al., 2006, Petersen et al., 2003a,b), and since neocortical axons carry mostly or only AP-related information, it follows that axons, in spite of their nontrivial total surface area, are likely of little consequence in shaping VSDI measurements. This claim awaits definitive confirmation in future modeling studies that explicitly represent axonal compartments in the calculation of *in silico* VSDI signals.

5.2 Lack of Correlated Activity Between VSDI Signals and Single-Unit Activity

A point of disagreement between our results and those described in literature is the degree to which VSD recordings are correlated with simultaneous WC patch-clamp recordings in L2/3 (Fig. 4.4). Several *in vivo* studies have reported a high correlation between VSD fluorescence and the V_m of single neurons in L2/3 rodent barrel cortex (Berger et al., 2007, Ferezou et al., 2006, Petersen et al., 2003b,a). However, due to the technical challenges associated with simultaneously performing VSDI and WC recordings in live animals, these studies used anesthesia or *in vitro* slice preparations to establish the correspondence between V_m and VSDI traces. It has been shown that anesthetic agents increase cortical synchrony and pairwise neural correlations (Antkowiak, 2002, Greenberg et al., 2008, Kreuzer et al., 2010, Murphy et al., 2011). Of particular relevance, Greenberg et al. (2008) found that correlated AP firing in pairs and populations of L2/3 neurons in rat visual cortex increased significantly during anesthesia as compared to the awake state. Therefore, the disparity between the strength of VSDI-V_m correlations observed *in vivo* and those extracted from our simulations may be at least partly explained by differences in cortical state. Since VSDI signals reflect an average over V_m deflections in a large number of neuronal processes mostly situated in L2/3, anesthesia-induced synchrony among L2/3 neurons would tend to increase the correlation between any given L2/3 neuron and the population mean. Our model does not consider the effects of anesthesia, nor do we observe the emergence of oscillatory cortical states. Thus, both pairwise and population neural correlations remain relatively weak during spontaneous activity (Fig.4.4a), resulting in

a lower correspondence between VSD fluorescence and measurements of V_m in individual neurons.

5.3 Changes in Spiking Activity Precede Deflections in Mean Membrane Potential

We showed that spikes precede V_m fluctuations during both spontaneous and evoked activity (see Fig. 4.2c,d; Fig. 4.6a; Fig. 4.10b), confirming several studies including one in rat barrel cortex (Petersen et al., 2003a), and two others in ferret visual cortex (Eriksson et al., 2008, Roland et al., 2006). A reasonable expectation may be that, on the contrary, increases in VSD fluorescence should precede increased spike firing, since membrane depolarization would tend to bring neurons closer to threshold, making APs more likely. However, as suggested by Eriksson et al. (2008), since each cell contacts many postsynaptic partners (452 ± 272 in our microcircuit), any given AP will elicit PSPs in hundreds to thousands of other cells, meaning that a mere handful of spikes can significantly impact mean V_m in a population. Of course, spike initiation requires membrane depolarization, but only a fraction of the population is active at once (~26% at evoked response peak, and ~0.4% during baseline; 2 ms bins). Therefore, V_m changes associated with spike firing are outweighed by downstream PSPs, with a monosynaptic delay. We found a 6.9 ms delay between peak spiking and subthreshold response to stimulation (Fig. 4.2c,d), and a 22.7 ms delay during spontaneous activity (Fig. 4.10b). Monosynaptic signal transmission reportedly requires between 6 and 14 ms in cortex (González-Burgos et al., 2000), suggesting that deflections in mean V_m primarily reflect monosynaptic activity in the first case (evoked), and disynaptic inhibition in the second (spontaneous). Indeed, this conclusion is supported by the reversal of sign in the correlation between V_m and firing rate in the putatively disynaptic, spontaneous case. Furthermore, uncoupling the network, thereby disabling recurrent disynaptic connections, abolished the temporal lag and inverse relationship between spiking and mean V_m (Fig. 4.10i), creating a situation in which increased membrane potential merely potentiates APs. Thus, VSDI may primarily report either monosynaptic excitation or disynaptic inhibition depending on the presence or absence of external inputs (n.b. external inputs still ultimately recruit an inhibitory response, which is reflected in the VSDI signal; see Section 5.5). That this aspect of VSDI measurements could have been missed in previous research begs explanation. First, simultaneously performing VSDI measurements and population spike recordings is a technical challenge, and has only been attempted in a handful of studies (e.g., (Chen et al., 2012, Eriksson et al., 2008, Roland et al., 2006)). Moreover, the lag between VSDI signals and spike firing, in addition to any extracortical noise sources, would tend to obscure the immediate observation of a correlation. Last, VSDI signals are imperfect proxies of mean V_m since they are heavily biased towards contributions of neurites within L2/3 (Fig. 4.2b).

5.4 Influence of Cortical State on Network Dynamics

Regenerative activity in the microcircuit is sensitive to the level of $[Ca^{2+}]_o$ and amount of tonic depolarization. As demonstrated by Markram et al. (2015), increasing tonic depolarization has the effect of pushing cells closer to AP threshold, while decreasing $[Ca^{2+}]_o$ (within the physiological range, 1-2 mM) tends to shift the excitatory-inhibitory balance in favor of inhibition. Varying these two parameters, they observed the emergence of four distinct regimes in the behavior of the microcircuit, characterized by the presence or absence of regenerative activity for either spontaneous or evoked conditions. Furthermore, within each regime, varying $[Ca^{2+}]_o$ moved the network along a spectrum between synchrony (high $[Ca^{2+}]_o$) and asynchrony (low $[Ca^{2+}]_o$). It is well established that *in vivo* concentrations of extracellular ions are maintained within relatively narrow physiological ranges by tightly regulated homeostatic pathways, and that alterations in these concentrations affect network dynamics (Barreto and Cressman, 2011, Ding et al., 2016, Gleichmann and Mattson, 2010, Henn et al., 1972, Kraio and Nicholson, 1978, Rasmussen et al., 2017). We theorize that a spectrum of network regimes similar to those observed in our network could also be present in biological cortex, and that under normal physiological conditions, the network sits at or near the transition point between regimes. This could serve to maximize sensitivity subject to the constraint of avoiding runaway excitation, thereby optimizing the potential of cortical tissue to encode sensory stimuli. Furthermore, it is known from *in vivo* recordings that cortical neurons in awake animals exhibit low input resistances, relatively depolarized membrane potentials (~-60 mV), and significant V_m fluctuations (Destexhe, 2010, 2007, Destexhe et al., 2003). Collectively, these properties are referred to as the "high-conductance state", since they are a consequence of synaptic bombardment causing mean conductances to exceed resting conductance (Destexhe, 2007). High-conductance states are thought to play an important role in determining neural response properties, with consequences for computation (Destexhe, 2010, 2007, Destexhe et al., 2003). Independent and convergent lines of evidence suggest that the critical transition point in our model (somatic depolarization at ~100% and $[Ca^{2+}]_o$ = 1.25 mM) is most analogous to quiet-wakefulness, with some high-conductance state properties.

Comparing the time to peak and half width duration of our evoked VSDI response to those obtained in a similar study of mouse barrel cortex (Fig. 4.2b) reveals a strong correspondence in the temporal profile of cortical activation for awake animals (half width: 86 ± 69 ms), but not anesthetized (37 ± 8 ms) (Ferezou et al., 2006). Furthermore, the dominance of inhibitory conductances, relatively depolarized membrane potentials, and significant V_m fluctuations argue for a high-conductance-like state, which is associated with wakefulness (Destexhe, 2010, 2007, Destexhe et al., 2003). Finally, the slow-wave oscillations typically observed during sleep and anesthesia are not present in our model, though this may be a result of missing thalamocortical interactions or neuromodulation, rather than a local property of the tissue (Contreras and Steriade, 1996, Contreras et al., 1997, Mena-Segovia et al., 2008, Murphy et al., 2011, Steriade, 2000). Thus, we propose that the results of our model are best interpreted as representing an *in vivo*-like quiet-wakeful state. We note at least one major caveat to the above

interpretation, namely that values of synaptic conductances are significantly lower than those estimated from *in vivo* recordings in the awake state. Since high conductances in dendritic arbors are known to affect the integrative properties of neurons (Destexhe, 2007, Destexhe et al., 2003), this discrepancy is likely to affect network dynamics. However, we leave a detailed analysis of the consequences for future research.

5.5 VSDI-Firing Rate Anticorrelation Lag Time: An Index of Locality?

As described previously (see Section 4.5 and Fig. 4.10), firing rate anticorrelates with mean V_m in the NMC at the assembly level during spontaneous activity. We demonstrated that this relationship is dependent on network balance enforced through recurrent connectivity, whereby increases in excitation quickly recruiting a proportional inhibitory response through recurrent connections. However, this observation was made in the context of spontaneous activity in an isolated local network, suggesting that a relaxation of these conditions could moderate the phenomenon. To this end, we attempted to replicate the effects of extrinsic (non-local) synaptic inputs in Section 4.6 and assessed changes in the mean, standard deviation, and ratio of g_e and g_i. Added extrinsic synapses were excitatory, since long-range corticocortical inputs are understood to be primarily glutamatergic, while inhibition tends to be confined locally (Roland et al., 2006, 2014, Roland, 2017). Sue to resource constraints, we were restricted to NMC simulations with additional extrinsic inputs at a mere handful of synapses in the network, and were thus unable to evaluate alterations to the relationship between mean V_m and population firing rate as a function of long-range input statistics. However, our preliminary results indicate a shift in the ratio of g_i and g_e in individual neurons, implying that extrinsic inputs can influence local network properties. Indeed, Roland (2017) suggest that network balance is a local property that is tightly maintained during spontaneous activity, but which may be temporarily disrupted by a quick succession of excitatory APs from non-local cortical regions. For sufficiently powerful inputs, local inhibitory neurons cannot fully compensate for increased excitatory activity, and additional inhibitory cells must be recruited to prevent runaway excitation (Roland, 2017, Huys et al., 2016, Dehghani et al., 2016). Recruiting additional inhibition introduces a delay between peaks in inhibitory and excitatory firing, relaxing the tight balance of activity in the network (Roland, 2017). Thus, we propose that the inverse relationship between VSDI signals and population firing rate revealed by our model provides an "index of locality", i.e. an increased delay in the peak anticorrelation between VSDI and population spiking represents a stronger perturbing extrinsic influence. Mechanistically, the delay between firing rate and VSDI fluctuations reflects the time required after a spike is fired for recurrently connected inhibitory neurons to respond by hyperpolarizing the V_m of the spiking cells. Thus, we predict that stronger cortical stimuli will produce greater lags for peak anticorrelation between VSD fluorescence and population firing rates in experiments where these data are collected concomitantly. We note that such inputs will also induce a *positive* correlation between spike rates and VSDI with a shorter temporal delay, prior

to the recruitment of a compensatory inhibitory response. Currently, the bulk of evidence for network balance has been drawn from correlations in the membrane potentials of nearby cells with similar orientation tuning, and measurements of conductance ratios over time in individual cells (Denève and Machens, 2016). Our proposal for the novel use of VSDI data to determine a locality index would add confirmatory evidence for the balance of inhibition and excitation at the *network* level, while simultaneously providing a metric for evaluating the degree of influence of non-local activity on local microcircuitry.
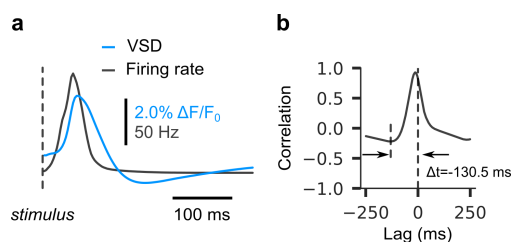

Figure 5.2 – **VSDI vs. Firing Rate for Evoked Activity**

a, VSDI activity (blue line) and population firing rate (black line) in a 350 ms post-stimulus time window (averaged over n=10 trials). Dashed horizontal line indicates stimulus onset. **b**, Cross-correlogram of traces in a (VSD vs. firing rate) for lags spanning the interval [-250 ms, 250 ms]. Time lag associated with anticorrelation peak (-130.5 ms) framed by horizontal arrows.

At least one study by Chen et al. (2012) has examined the relationship between spiking activity and VSDI in awake, unanesthetized animals. Specifically, they scrutinized the position and orientation tuning of cortical neurons in primate V1 using both single-unit electrophysiology and VSDI. From these measurements, they developed a mathematical model to relate spike rates and VSDI (and their respective tuning curves) using a power law formulation (Chen et al., 2012). This model asserts a positive, albeit nonlinear, relationship between spike rates and VSDI signals. Superficially, the observation of a positive association between spike rates and VSDI appears to contradict our claim that the two are anticorrelated. However, the apparent tension could be resolved in consideration of the strong visual stimulation (producing spiking in excess of 100 Hz) used by Chen et al. (2012) to evoke a cortical response. Figure 5.2 illustrates the interdependence between VSDI and spiking in the NMC under *evoked* (as opposed to spontaneous) conditions. As discussed above, strong extrinsic input initially depolarizes neural membranes, potentiating an increase in spiking. This manifests as a positive peak in the plot of cross-correlation between V_m and spike rate. However, several milliseconds later, the recruitment of compensatory activity in inhibitory units produces a negative peak at a negative latency in the cross-correlogram. By contrast, during spontaneous conditions, in the absence of an external driving force, the secondary effects of inhibitory feedback are more pronounced in the VSDI signature.

5.6   Limitations and Outlook

Concerning the validity of the *in silico* model of VSDI presented here, we propose the consideration of three conceptual layers: 1) whether the biophysical model of VSDI, i.e. the calculations linking cellular activity to measured fluorescence, reasonably approximate reality, 2) whether the composition and architecture of the tissue itself is biologically plausible, 3) whether the simulations are *functionally* representative of biological neocortex.

On the first account, we assert that the excellent linearity and fast kinetics of VSDs (Lippert et al., 2007) greatly simplify their analytical relationship to V_m. Regarding the second concern, a significant caveat is the absence of several important structural details from the version of the NMC used here, including glial cells, vasculature, and long-range intracortical axons (Markram et al., 2015). The presence or absence of these entities could influence the magnitude and timecourse of VSD fluorescence, irrespective of the validity of broad trends in the activity of the network. However, in the case of glia, the slow timescale of response (3-4 ms (Schummers et al., 2008)) and small amplitude of V_m deflections (1-7 mV (Kelly and Essen, 1974)) make it unlikely that they contribute meaningfully to VSDI signals. As regards vasculature, since our *in silico* VSDI pipeline already accounts for the bulk optical properties of cortical tissue (Section 3.3), their effects have, in principle, been accounted for. With respect to the third concern above, several details that are likely to influence network dynamics, including gap junctions, multivesicular release, neuromodulation, and synaptic plasticity, are not present in this version of the NMC (Markram et al., 2015). In addition, we note several caveats conerning the comparison of our *in silico* stimulation protocol to whisker deflection experiments. First, as a model of hindlimb somatosensory cortex, the NMC lacks the unique cytoarchitecture and anatomical organization that characterize barrel cortex (Schlaggar and O'Leary, 1994, Simons et al., 1984), despite our comparisons to such studies (see Section 4.1). Furthermore, the NMC excludes the trigeminal and thalamic nuclei, and therefore does not exhibit sensory processing delays (and VSDI response latencies) or the modulation of cortical dynamics by TC feedback. Previous experiments have shown that cortical activation patterns depend on stimulus strength, with a tendency for excitation evoked by weak stimuli to remain confined to a single barrel (Berger et al., 2007, Fehérvári et al., 2015, Gollnick et al., 2016, Petersen et al., 2003a). In our model, TC projection fibers innervating the geometrical center of the microcircuit fire a simultaneous AP, a construction that does not capture the full complexity of afferent TC signaling nor permit modification of the stimulus strength in a biologically plausible way. In addition, experiments in the sensorimotor cortex of rodents are typically conducted under conditions of either anesthesia, quiet-wakefulness, or active whisking (Berger et al., 2007, Civillico and Contreras, 2012, 2006, Ferezou et al., 2006, Petersen and Sakmann, 2001, Petersen et al., 2003a,b). As a precise account of the effects of these states on cortical physiology requires more sophistication than our model currently provides, our results cannot reproduce state-dependent differences. Indeed, experiments have implicated reciprocal TC pathways (Bazhenov et al., 2002, Hughes et al., 2002, Steriade et al., 1993a) and intracortical interactions (Timofeev et al., 2000) in the emergence of slow wave activity. It

is known that cortical oscillations interact with sensory responses to produce differentiated VSDI signals (Petersen et al., 2003a). Thus, an in silico account of the effects of brain state on VSDI measurements awaits future iterations of the NMC that include TC feedback and corticocortical interactions.

Despite these shortcomings, the NMC exhibits surprisingly realistic activity, reproducing experimentally known cell type-specific responses to stimulation, network balance through coupling of inhibitory and excitatory populations, and repeating spike triplet motifs during activated states (see Section 2.3). In addition, our *in silico* model of VSDI recapitulates the spatiotemporal dynamics of experimental VSDI measurements (Section 4.1), bolstering our confidence in the NMC as a model of cortical information processing. A fully integrated theory of the brain, in which observed activity must be understood as the result of interdependent interactions between scales and subsystems, implies that breaking or neglecting any dependency would result in meaningless outputs. However, the successes of the NMC demonstrate that this is not strictly the case, and show that an iterative, reductionist approach to simulation neuroscience is possible, whereby complex phenomena are modeled bottom-up from available data, with refinements and improvements added over successive generations. Future versions of BBP brain models that extend well beyond the mircocircuit scale are forthcoming. An anatomically complete reconstruction of the somatosensory cortex (and ultimately the entire neocortex) featuring biologically appropriate macro- and micro-connectivity (Reimann et al., 2019) will help to resolve questions concerning the effects of missing long- and mid-range inputs. Additionally, a model of neuromodulatory dynamics, the effects of which are known to be implicated in the transitions between, and maintenance of, cortical states (Colangelo et al., 2019), will support an investigation of state-dependent VSDI responses. Finally, a full account of the neuro-glia-vasculature ensemble will facilitate confirmation of the minimal role of glia in shaping the VSDI signal, and also pave the way for future models of imaging techniques such as fMRI that rely on blood-oxygen-level-dependent (BOLD) signals.

5.7   Key Findings and Concluding Remarks

This research demonstrates the utility of bottom-up biophysical modeling for refining knowledge of the relationships between spatial and temporal scales of cortical signaling. *in silico* VSDI allowed us to both augment the understanding of the origins of VSDI signals, and to probe dynamics in the NMC to uncover new insights regarding the use and interpretation of VSDI. These advances were made possible by engaging the power of our model to bridge mesoscale phenomena and the cellular processes from which they emerge. Our efforts furnished the following key results:

- **Spatiotemporal Dynamics**

    1. The spatiotemporal dynamics of evoked VSDI responses to afferent TC stimulation recapitulate *in vivo* findings. Specifically, the peak phase velocity of propagating

activity waves (20 μm/ms), time to peak (57 ms), and half width duration (88 ms) of spatially averaged VSDI signals, agree with experimentally reported values within an order of magnitude.

2. Peak AP firing occurs *prior* to peak VSD fluorescence during evoked activity, with a delay of ~7 ms. This lag is a consequence of dense connectivity, wherein a single AP causes V_m polarization in hundreds or thousands of postsynaptic cells.

3. VSDI activity at the site of stimulation quickly saturates in a confined region, expanding outward after a delay, likely due to initial monosynaptic excitation followed by disynaptic activation at greater latencies.

4. V_m depolarization occurs with near simultaneity in L4 through L6 immediately following stimulation, opposing prior claims that activity originates in L4 and spreads to the other layers in sequence.

- **Cellular Origins**

  1. Neurites belonging to L5 cells contribute a significant fraction (~40%) of the VSDI signal during spontaneous activity, due to extensive arborization in the superficial layers. Most of the remainder (~50%) derives from L2/3 neurites.

  2. L5 cells respond with highly synchronous depolarization following stimulation, whereas L2/3 exhibits a greater diversity of responses, with net hyperpolarization. These trends are reflected in their contributions to the VSDI signal, with depolarized L5 neurites constituting >67% of the total, and hyperpolarized L2/3 neurites making up ~19%.

- **Sub- and Suprathreshold Contributions**

  1. APs are too brief and asynchronous to contribute meaningfully to VSDI fluctuations, unless imaged with exceptional SNR ($\gg$10) during periods of synchronous activity in mesoscale neural populations. The spike-related signal component is band-limited to <100 Hz.

  2. Any spiking contributions to the VSDI signal are due to back-propagating APs, which require ~7 ms to ascend the apical trunk and diffuse through apical dendritic arborizations.

- **Two-Point Discrimination**

  1. For VSDI image frames in close temporal proximity to stimulus onset, pixels nearest the location of stimulus delivery are the best discriminators between two spatially separated presentations of otherwise identical stimuli.

  2. For time-collapsed VSDI data, pixels towards the periphery are the best discriminators of stimulus location due to the asymmetrical evolution of activity for stimuli displaced from the geometrical center of the NMC.

3. Only a small minority of individual cells ($\geq 95^{\text{th}}$ percentile) exhibit spiking activity sufficient to discriminate between stimulus locations.

4. Simulations indicate that for separations <25 μm, *in silico* VSDI is unable to resolve differences in stimulus location, establishing a likely lower bound for the functional resolution of laboratory VSDI.

- **VSDI & Population Spiking**

    1. Mean V_m (and by extension VSDI) and population firing rates anticorrelate with a peak delay of ~23 ms during spontaneous activity.

    2. Anticorrelation between subthreshold activity and spiking is dependent on recurrent connectivity, and is a consequence of network balance.

    3. VSDI likely reflects primarily monosynaptic excitation during evoked activity, and disynaptic inhibition during spontaneous activity.

    4. Simulation of additional extrinsic synaptic inputs with presynaptic Poisson spike trains caused increases in mean g_e and the standard deviation of g_e and g_i in individual neurons.

    5. We propose an interpretation of the lag time associated with the negative peak of the cross-correlation of VSDI and firing rate as an index of locality, representing the degree to which local microcircuitry is perturbed by external inputs. We predict that paired recordings of VSDI and population spiking will corroborate this relationship experimentally.

Returning to the question posed in Section 1.1: is the brain's complexity fundamentally irreducible, or are there relatively tractable principles of organization that can be understood using a reductionist scientific approach? It may be that the arguably limited success of contemporary neuroscientific techniques to provide a holistic, interpretable explanation of the brain lies not in its impenetrable organizing principles, but rather the ill-suited nature of these techniques to the task at hand. The brain is a delicate tissue, and the spatiotemporal scales on which it operates are prohibitive. Thus, an historical deficit of apropos experimental methods reflects the physical limitations challenging their construction. As computing power continues to grow, and costs to decline, simulations are an increasingly attractive tool in the suite of available techniques for studying the brain. Unlike their traditional counterparts, simulations provide unfettered access to all spatiotemporal scales in a model, thereby allowing advances that relate emergent phenomena across scales. We have endeavored here to provide insights of both theoretical and practical value to experimental researchers and also the simulation neuroscience community, using a biophysically detailed model with the power to bridge scales of cortical processing. However, we predict that the use of simulations to study the brain is yet in its infancy, and will occupy a position of increasing importance in the toolkit of neuroscientists in the years to come. This work represents a small step in that direction.

Appendix

Parameter and Symbol Tables

Table 1 – VSDI Calculation Parameters

dim, res	1000 μm, 100	Dimensions and pixel resolution of detector.
μ_{eff}	1.5 mm^{-1}	Effective modified Beer-Lambert law extinction coefficient.
G_0	250	Autofluorescence and noise calibration term.
V_m^0	-65 mV	Resting membrane potential.
f_s	2000 Hz	Sampling frequency for VSD measurements.
t_{start}, t_{end}	1000 ms, 1050 ms	Start and stop times for calculation of baseline fluorescence.

Appendix

<div align="center">Table 2 – Imaging System Parameters</div>

λ_a, λ_e	630 nm, 665 nm	Peak RH1691/2 absorption and emission wavelengths, respectively.
μ_s'	4 mm^{-1}	Reduced scattering coefficient.
μ_a	0.4 mm^{-1}	Absorption coefficient.
n_1, n_2	1.0, 1.37	Refractive indices for air and rodent cortical tissue (Binding et al., 2011), respectively.
g	0.88	Anisotropy coefficient.
f_1, f_2	50 mm, 135 nm	Focal lengths of objective and tube lenses, respectively.
$f_1/$, $f_2/$	0.95, 2.0	F-numbers of objective and tube lenses, respectively.
D_1, D_2	52.6 mm, 67.5 mm	Diameters of objective and tube lenses, respectively.
NA$_1$	0.526	Numerical aperture of objective lens.
P	38.1 mm	Infinity space pathlength.
WD	49.7 mm	Working distance of objective lens.

Table 3 – Mean Field Parameters

E_e, E_i	-1.6 mV, -86.6 mV	Excitatory and inhibitory reversal potentials, respectively.
q_e, q_i	0.84 nS, 0.85 nS	Excitatory and inhibitory quantal conductance increments, respectively.
τ_e, τ_i	1.7 ms, 8.4 ms	Excitatory and inhibitory synatpic time constants, respectively.
g_l	44.4 nS	Passive (leak) conductance.
E_l	-62.7 mV	Passive (leak) reversal potential.
C_m	190.7 pF	Total membrane capacitance.
$\langle I_{\text{clamp}} \rangle$	-98.1 pA	Mean injected somatic depolarizing current.
f_{char}	13.96 Hz	Characteristic frequency of oscillations in spontaneous mean V_m.

Table 4 – Definitions of Terms for Equations 3.15 - 3.17

λ	Wavelength of photons.
μ_s'	Reduced scattering coefficient.
μ_s	Scattering coefficient.
μ_a	Absorption coefficient.
$\mathbf{x}', \mathbf{x}_j^i$	Detector pixel location, and position of ith photon after jth event, respectively.
ω', ω_j^i	Angle of incoming light to detector pixel, and direction of ith photon after jth event, respectively.
$I(\mathbf{x}', \omega')$	Intensity of light at detector pixel location $\mathbf{x}'$ with incoming angle ω'.
$I(\mathbf{x}_0^i, \lambda)$	Intensity of the ith emitted photon at location $\mathbf{x}_0^i$ with wavelength λ.
$p(\mathbf{x}_0^i)$	Probability of emission of ith photon at location $\mathbf{x}_0^i$.
$\phi(\mathbf{x}_j, \omega_j, \omega_{j+1}, \lambda)$	Phase function determining probability distribution of scattering angles.
$\tau(\mathbf{x}_j, \mathbf{x}_{j-1}, \lambda)$	Transmittance between two scattering events at points $\mathbf{x}_j$ and $\mathbf{x}_{j-1}$.
$p(\omega_j)$	Probability of new direction ω_j after scattering.
$p(t_j)$	Probability of travelling distance t_j after scattering.

Algorithms

Algorithm 1: 2D Gaussian Fit

 input :A surface arr of size $n \times m$
 output:A 2D Gaussian fit

 /* compute 2D surface   */
1 **Function** 2DGauss(h, x, y, σ_x, σ_y)**:**

2   **return** $h \cdot \exp -\frac{1}{2}\left[\left(\frac{x}{\sigma_x}\right)^2 + \left(\frac{y}{\sigma_y}\right)^2\right]$

 /* compute first-order moments of arr   */
3 **Function** Moments(arr)**:**
4   total $\leftarrow$ sum of entries in arr
5 $x_0 \leftarrow \frac{1}{\text{total}} \sum (\{\text{row of arr}\} \times \{\text{row index}\})$ // 1st moment in x
6 $y_0 \leftarrow \frac{1}{\text{total}} \sum (\{\text{col of arr}\} \times \{\text{col index}\})$ // 1st moment in y
7   r $\leftarrow$ row of arr at index int(x)
8   c $\leftarrow$ column of arr at index int(y)
9 $\sigma_x \leftarrow \sqrt{\sum |(r - \text{index of r}) \times r|^2 / \sum r}$
10 $\sigma_y \leftarrow \sqrt{\sum |(c - \text{index of c}) \times c|^2 / \sum c}$
11   h $\leftarrow$ max of arr
12   **return** x_0, y_0, h, σ_x, σ_y

 /* compute 2D surface   */
13 **Function** Fitgauss(arr)**:**
14 x_0, y_0, h, σ_x, σ_y $\leftarrow$ Moments(arr)
15   x $\leftarrow$ $n \times m$ matrix of row indices
16   y $\leftarrow$ $n \times m$ matrix of column indices
17   **def** err_fn *(*x, y, arr*)***:**
18   return 2DGauss(x-x_0, y-y_0, h, σ_x, σ_y) - arr
19   **return** LeastSq(err_fn, x, y, arr)   // least-squares fit using
   scipy.optimize

 /* main routine   */
20 **Function** Main(arr)**:**
21   params = Fitgauss(arr)

Bibliography

Marwan Abdellah, Ahmet Bilgili, Stefan Eilemann, Julian Shillcock, Henry Markram, and Felix Schürmann. Bio-physically plausible visualization of highly scattering fluorescent neocortical models for in silico experimentation. *BMC Bioinformatics*, 18(2):62, February 2017. ISSN 1471-2105. doi: 10.1186/s12859-016-1444-4. URL https://doi.org/10.1186/s12859-016-1444-4.

M. Abeles and I. Gat. Detecting precise firing sequences in experimental data. *Journal of Neuroscience Methods*, 107(1):141–154, May 2001. ISSN 0165-0270. doi: 10.1016/S0165-0270(01)00364-8. URL http://www.sciencedirect.com/science/article/pii/S0165027001003648.

Saif I. Al-Juboori, Anna Dondzillo, Elizabeth A. Stubblefield, Gidon Felsen, Tim C. Lei, and Achim Klug. Light Scattering Properties Vary across Different Regions of the Adult Mouse Brain. *PLoS ONE*, 8(7), July 2013. ISSN 1932-6203. doi: 10.1371/journal.pone.0067626. URL https://www.ncbi.nlm.nih.gov/pmc/articles/PMC3706487/.

John S. Allen, Hanna Damasio, and Thomas J. Grabowski. Normal neuroanatomical variation in the human brain: An MRI-volumetric study. *American Journal of Physical Anthropology*, 118(4):341–358, 2002. ISSN 1096-8644. doi: 10.1002/ajpa.10092. URL https://onlinelibrary.wiley.com/doi/abs/10.1002/ajpa.10092.

D. G. Altman and J. M. Bland. Diagnostic tests 3: receiver operating characteristic plots. *BMJ : British Medical Journal*, 309(6948):188, July 1994. ISSN 0959-8138. URL https://www.ncbi.nlm.nih.gov/pmc/articles/PMC2540706/.

Y. Amitai. Thalamocortical synaptic connections: Efficacy, modulation, inhibition and plasticity. *Reviews in the Neurosciences*, 12(2):159–173, 2001.

Florin Amzica, Marcello Massimini, and Alfredo Manfridi. Spatial buffering during slow and paroxysmal sleep oscillations in cortical networks of glial cells in vivo. *The Journal of Neuroscience: The Official Journal of the Society for Neuroscience*, 22(3):1042–1053, February 2002. ISSN 1529-2401.

B Antkowiak. In vitro networks: cortical mechanisms of anaesthetic action. *British Journal of Anaesthesia*, 89(1):102–111, July 2002. ISSN 0007-0912. doi: 10.1093/bja/aef154. URL http://www.sciencedirect.com/science/article/pii/S0007091217375943.

73

Bibliography

Haroon Anwar, Imad Riachi, Sean Hill, Felix Schürmann, and Henry Markram. *An Approach to Capturing Neuron Morphological Diversity*. The MIT Press, September 2009. ISBN 978-0-262-25872-2. URL https://mitpress.universitypressscholarship.com/view/10.7551/mitpress/9780262013277.001.0001/upso-9780262013277-chapter-10.

Amos Arieli, Alexander Sterkin, Amiram Grinvald, and Ad Aertsen. Dynamics of Ongoing Activity: Explanation of the Large Variability in Evoked Cortical Responses. *Science*, 273 (5283):1868–1871, September 1996. ISSN 0036-8075, 1095-9203. doi: 10.1126/science.273. 5283.1868. URL https://science.sciencemag.org/content/273/5283/1868.

G.A. Ascoli, L. Alonso-Nanclares, S.A. Anderson, G. Barrionuevo, R. Benavides-Piccione, A. Burkhalter, G. Buzsáki, B. Cauli, J. DeFelipe, A. Fairén, D. Feldmeyer, G. Fishell, Y. Fregnac, T.F. Freund, D. Gardner, E.P. Gardner, J.H. Goldberg, M. Helmstaedter, S. Hestrin, F. Karube, Z.F. Kisvárday, B. Lambolez, D.A. Lewis, O. Marin, H. Markram, A. Mũoz, A. Packer, C.C.H. Petersen, K.S. Rockland, J. Rossier, B. Rudy, P. Somogyi, J.F. Staiger, G. Tamas, A.M. Thomson, M. Toledo-Rodriguez, Y. Wang, D.C. West, and R. Yuste. Petilla terminology: Nomenclature of features of GABAergic interneurons of the cerebral cortex. *Nature Reviews Neuroscience*, 9(7):557–568, 2008. doi: 10.1038/nrn2402.

Frederico A. C. Azevedo, Ludmila R. B. Carvalho, Lea T. Grinberg, José Marcelo Farfel, Renata E. L. Ferretti, Renata E. P. Leite, Wilson Jacob Filho, Roberto Lent, and Suzana Herculano-Houzel. Equal numbers of neuronal and nonneuronal cells make the human brain an isometrically scaled-up primate brain. *Journal of Comparative Neurology*, 513(5):532–541, 2009. ISSN 1096-9861. doi: 10.1002/cne.21974. URL https://onlinelibrary.wiley.com/doi/abs/10.1002/cne.21974.

Mehdi Azimipour, Ryan Baumgartner, Yuming Liu, Steven L. Jacques, Kevin W. Eliceiri, and Ramin Pashaie. Extraction of optical properties and prediction of light distribution in rat brain tissue. *Journal of Biomedical Optics*, 19(7):075001, July 2014. ISSN 1083-3668, 1560-2281. doi: 10.1117/1.JBO.19.7.075001. URL https://www.spiedigitallibrary.org/journals/Journal-of-Biomedical-Optics/volume-19/issue-7/075001/Extraction-of-optical-properties-and-prediction-of-light-distribution-in/10.1117/1.JBO.19.7.075001.short.

Wesley B. Baker, Ashwin B. Parthasarathy, David R. Busch, Rickson C. Mesquita, Joel H. Greenberg, and A. G. Yodh. Modified Beer-Lambert law for blood flow. *Biomedical Optics Express*, 5(11):4053–4075, November 2014. ISSN 2156-7085. doi: 10.1364/BOE.5.004053. URL https://www.osapublishing.org/boe/abstract.cfm?uri=boe-5-11-4053.

Ernest Barreto and John R. Cressman. Ion concentration dynamics as a mechanism for neuronal bursting. *Journal of Biological Physics*, 37(3):361–373, June 2011. ISSN 1573-0689. doi: 10.1007/s10867-010-9212-6. URL https://doi.org/10.1007/s10867-010-9212-6.

E. Bartfeld and A. Grinvald. Relationships between orientation-preference pinwheels, cytochrome oxidase blobs, and ocular-dominance columns in primate striate cortex. *Proceed-*

ings of the National Academy of Sciences of the United States of America, 89(24):11905–11909, December 1992. ISSN 0027-8424. doi: 10.1073/pnas.89.24.11905.

Maxim Bazhenov, Igor Timofeev, Mircea Steriade, and Terrence J. Sejnowski. Model of Thalamocortical Slow-Wave Sleep Oscillations and Transitions to Activated States. *Journal of Neuroscience*, 22(19):8691–8704, October 2002. ISSN 0270-6474, 1529-2401. doi: 10.1523/JNEUROSCI.22-19-08691.2002. URL http://www.jneurosci.org/content/22/19/8691.

Charles B. Beaman, Sarah L. Eagleman, and Valentin Dragoi. Sensory coding accuracy and perceptual performance are improved during the desynchronized cortical state. *Nature Communications*, 8(1):1–14, November 2017. ISSN 2041-1723. doi: 10.1038/s41467-017-01030-4. URL https://www.nature.com/articles/s41467-017-01030-4.

M. Beierlein, J. R. Gibson, and B. W. Connors. A network of electrically coupled interneurons drives synchronized inhibition in neocortex. *Nature Neuroscience*, 3(9):904–910, September 2000. ISSN 1097-6256. doi: 10.1038/78809.

Thomas Berger, Aren Borgdorff, Sylvain Crochet, Florian B. Neubauer, Sandrine Lefort, Bruno Fauvet, Isabelle Ferezou, Alan Carleton, Hans-Rudolf Lüscher, and Carl C. H. Petersen. Combined Voltage and Calcium Epifluorescence Imaging In Vitro and In Vivo Reveals Subthreshold and Suprathreshold Dynamics of Mouse Barrel Cortex. *Journal of Neurophysiology*, 97(5):3751–3762, May 2007. ISSN 0022-3077, 1522-1598. doi: 10.1152/jn.01178.2006. URL http://jn.physiology.org/content/97/5/3751.

Manish Bhatt, Kaylan R. Ayyalasomayajula, and Phaneendra K. Yalavarthy. Generalized Beer–Lambert model for near-infrared light propagation in thick biological tissues. *Journal of Biomedical Optics*, 21(7):076012, July 2016. ISSN 1083-3668, 1560-2281. doi: 10.1117/1.JBO.21.7.076012. URL https://www.spiedigitallibrary.org/journals/Journal-of-Biomedical-Optics/volume-21/issue-7/076012/Generalized-BeerLambert-model-for-near-infrared-light-propagation-in-thick/10.1117/1.JBO.21.7.076012.short.

Jonas Binding, Juliette Ben Arous, Jean-François Léger, Sylvain Gigan, Claude Boccara, and Laurent Bourdieu. Brain refractive index measured in vivo with high-NA defocus-corrected full-field OCT and consequences for two-photon microscopy. *Optics Express*, 19(6):4833–4847, March 2011. ISSN 1094-4087. doi: 10.1364/OE.19.004833. URL https://www.osapublishing.org/oe/abstract.cfm?uri=oe-19-6-4833.

G. G. Blasdel. Differential imaging of ocular dominance and orientation selectivity in monkey striate cortex. *Journal of Neuroscience*, 12(8):3115–3138, August 1992a. ISSN 0270-6474, 1529-2401. doi: 10.1523/JNEUROSCI.12-08-03115.1992. URL https://www.jneurosci.org/content/12/8/3115.

G. G. Blasdel. Orientation selectivity, preference, and continuity in monkey striate cortex. *Journal of Neuroscience*, 12(8):3139–3161, August 1992b. ISSN 0270-6474, 1529-2401. doi: 10.1523/JNEUROSCI.12-08-03139.1992. URL https://www.jneurosci.org/content/12/8/3139.

Bibliography

Aren J. Borgdorff, James F. A. Poulet, and Carl C. H. Petersen. Facilitating Sensory Responses in Developing Mouse Somatosensory Barrel Cortex. *Journal of Neurophysiology*, 97(4): 2992–3003, April 2007. ISSN 0022-3077, 1522-1598. doi: 10.1152/jn.00013.2007. URL http://jn.physiology.org/content/97/4/2992.

Allen W. Chan, Majid H. Mohajerani, Jeffrey M. LeDue, Yu Tian Wang, and Timothy H. Murphy. Mesoscale infraslow spontaneous membrane potential fluctuations recapitulate high-frequency activity cortical motifs. *Nature Communications*, 6, July 2015. doi: 10.1038/ncomms8738. URL http://www.nature.com/ncomms/2015/150720/ncomms8738/full/ncomms8738.html.

Frédéric Chavane, Dahlia Sharon, Dirk Jancke, Olivier Marre, Yves Frégnac, and Amiram Grinvald. Lateral Spread of Orientation Selectivity in V1 is Controlled by Intracortical Cooperativity. *Frontiers in Systems Neuroscience*, 5:4, 2011. ISSN 1662-5137. doi: 10.3389/fnsys.2011.00004.

S. Chemla and F. Chavane. A biophysical cortical column model to study the multi-component origin of the VSDI signal. *NeuroImage*, 53(2):420–438, November 2010a. ISSN 1053-8119. doi: 10.1016/j.neuroimage.2010.06.026. URL http://www.sciencedirect.com/science/article/pii/S1053811910008700.

S. Chemla and F. Chavane. Voltage-sensitive dye imaging: Technique review and models. *Journal of Physiology-Paris*, 104(1–2):40–50, January 2010b. ISSN 0928-4257. doi: 10.1016/j.jphysparis.2009.11.009. URL http://www.sciencedirect.com/science/article/pii/S0928425709000916.

Yuzhi Chen, Chris R. Palmer, and Eyal Seidemann. The relationship between voltage-sensitive dye imaging signals and spiking activity of neural populations in primate V1. *J Neurophysiol*, 107(12):3281–3295, June 2012. ISSN 0022-3077. doi: 10.1152/jn.00977.2011. URL https://www.ncbi.nlm.nih.gov/pmc/articles/PMC3378408/.

W. F. Cheong, S. A. Prahl, and A. J. Welch. A review of the optical properties of biological tissues. *IEEE Journal of Quantum Electronics*, 26(12):2166–2185, December 1990. ISSN 0018-9197. doi: 10.1109/3.64354.

D. B. Chklovskii, B. W. Mel, and K. Svoboda. Cortical rewiring and information storage. *Nature*, 431(7010):782–788, October 2004. ISSN 1476-4687. doi: 10.1038/nature03012.

Yansong Chua and Abigail Morrison. Effects of Calcium Spikes in the Layer 5 Pyramidal Neuron on Coincidence Detection and Activity Propagation. *Frontiers in Computational Neuroscience*, 10, 2016. ISSN 1662-5188. doi: 10.3389/fncom.2016.00076. URL https://www.frontiersin.org/articles/10.3389/fncom.2016.00076/full.

E.F. Civillico and D. Contreras. Comparison of Responses to Electrical Stimulation and Whisker Deflection Using Two Different Voltage-sensitive Dyes in Mouse Barrel Cortex in Vivo. *The Journal of Membrane Biology*, 208(2):171–182, November 2005. ISSN 1432-1424. doi: 10.1007/s00232-005-0828-6. URL https://doi.org/10.1007/s00232-005-0828-6.

Eugene F. Civillico and Diego Contreras. Integration of Evoked Responses in Supragranular Cortex Studied With Optical Recordings In Vivo. *Journal of Neurophysiology*, 96(1):336–351, July 2006. ISSN 0022-3077, 1522-1598. doi: 10.1152/jn.00128.2006. URL http://jn.physiology.org/content/96/1/336.

Eugene F. Civillico and Diego Contreras. Spatiotemporal properties of sensory responses in vivo are strongly dependent on network context. *Frontiers in Systems Neuroscience*, 6, April 2012. ISSN 1662-5137. doi: 10.3389/fnsys.2012.00025. URL http://www.ncbi.nlm.nih.gov/pmc/articles/PMC3325540/.

L. B. Cohen, B. M. Salzberg, H. V. Davila, W. N. Ross, D. Landowne, A. S. Waggoner, and C. H. Wang. Changes in axon fluorescence during activity: Molecular probes of membrane potential. *The Journal of Membrane Biology*, 19(1):1–36, December 1974. ISSN 1432-1424. doi: 10.1007/BF01869968. URL https://doi.org/10.1007/BF01869968.

Cristina Colangelo, Polina Shichkova, Daniel Keller, Henry Markram, and Srikanth Ramaswamy. Cellular, Synaptic and Network Effects of Acetylcholine in the Neocortex. *Front Neural Circuits*, 13, April 2019. ISSN 1662-5110. doi: 10.3389/fncir.2019.00024. URL https://www.ncbi.nlm.nih.gov/pmc/articles/PMC6473068/.

C. M. Colbert. Back-propagating action potentials in pyramidal neurons: a putative signaling mechanism for the induction of Hebbian synaptic plasticity. *Restorative Neurology and Neuroscience*, 19(3-4):199–211, 2001. ISSN 0922-6028.

D Contreras and M Steriade. Synchronization of low-frequency rhythms in corticothalamic networks. *Neuroscience*, 76(1):11–24, December 1996. ISSN 0306-4522. doi: 10.1016/S0306-4522(96)00393-4. URL http://www.sciencedirect.com/science/article/pii/S0306452296003934.

Diego Contreras and Rodolfo Llinás. Voltage-Sensitive Dye Imaging of Neocortical Spatiotemporal Dynamics to Afferent Activation Frequency. *Journal of Neuroscience*, 21(23):9403–9413, December 2001. ISSN 0270-6474, 1529-2401. doi: 10.1523/JNEUROSCI.21-23-09403.2001. URL http://www.jneurosci.org/content/21/23/9403.

Diego Contreras, Alain Destexhe, Terrence J. Sejnowski, and Mircea Steriade. Spatiotemporal Patterns of Spindle Oscillations in Cortex and Thalamus. *Journal of Neuroscience*, 17(3):1179–1196, February 1997. ISSN 0270-6474, 1529-2401. doi: 10.1523/JNEUROSCI.17-03-01179.1997. URL https://www.jneurosci.org/content/17/3/1179.

Rosa Cossart, Dmitriy Aronov, and Rafael Yuste. Attractor dynamics of network UP states in the neocortex. *Nature*, 423(6937):283–288, May 2003. ISSN 1476-4687. doi: 10.1038/nature01614. URL https://www.nature.com/articles/nature01614.

H. V. Davila, B. M. Salzberg, L. B. Cohen, and A. S. Waggoner. A Large Change in Axon Fluorescence that Provides a Promising Method for Measuring Membrane Potential. *Nature New Biology*, 241(109):159–160, January 1973. ISSN 2058-1092. doi: 10.1038/newbio241159a0. URL https://www.nature.com/articles/newbio241159a0.

Bibliography

Javier DeFelipe, Lidia Alonso-Nanclares, and Jon I. Arellano. Microstructure of the neocortex: Comparative aspects. *Journal of Neurocytology*, 31(3):299–316, March 2002. ISSN 1573-7381. doi: 10.1023/A:1024130211265. URL https://doi.org/10.1023/A:1024130211265.

Nima Dehghani, Adrien Peyrache, Bartosz Telenczuk, Michel Le Van Quyen, Eric Halgren, Sydney S. Cash, Nicholas G. Hatsopoulos, and Alain Destexhe. Dynamic Balance of Excitation and Inhibition in Human and Monkey Neocortex. *Scientific Reports*, 6:23176, March 2016. ISSN 2045-2322. doi: 10.1038/srep23176. URL https://www.nature.com/articles/srep23176.

Sophie Denève and Christian K. Machens. Efficient codes and balanced networks. *Nature Neuroscience*, 19(3):375–382, March 2016. ISSN 1546-1726. doi: 10.1038/nn.4243. URL https://www.nature.com/articles/nn.4243.

Alain Destexhe. High-conductance state. *Scholarpedia*, 2(11):1341, November 2007. ISSN 1941-6016. doi: 10.4249/scholarpedia.1341. URL http://www.scholarpedia.org/article/High-conductance_state.

Alain Destexhe. Inhibitory "noise". *Frontiers in Cellular Neuroscience*, 4, 2010. ISSN 1662-5102. doi: 10.3389/fncel.2010.00009. URL https://www.frontiersin.org/articles/10.3389/fncel.2010.00009/full.

Alain Destexhe, Michael Rudolph, and Denis Paré. The high-conductance state of neocortical neurons in vivo. *Nature Reviews Neuroscience*, 4(9):739–751, September 2003. ISSN 1471-0048. doi: 10.1038/nrn1198. URL https://www.nature.com/articles/nrn1198.

J. Deuchars, D. C. West, and A. M. Thomson. Relationships between morphology and physiology of pyramid-pyramid single axon connections in rat neocortex in vitro. *The Journal of Physiology*, 478 Pt 3:423–435, August 1994. ISSN 0022-3751. doi: 10.1113/jphysiol.1994.sp020262.

Andreea Dimofte, Jarod C Finlay, and Timothy C Zhu. A method for determination of the absorption and scattering properties interstitially in turbid media. *Physics in medicine and biology*, 50(10):2291–2311, May 2005. ISSN 0031-9155. doi: 10.1088/0031-9155/50/10/008. URL https://www.ncbi.nlm.nih.gov/pmc/articles/PMC4467592/.

Fengfei Ding, John O'Donnell, Qiwu Xu, Ning Kang, Nanna Goldman, and Maiken Nedergaard. Changes in the composition of brain interstitial ions control the sleep - wake cycle. *Science (New York, N.Y.)*, 352(6285):550–555, April 2016. ISSN 0036-8075. doi: 10.1126/science.aad4821. URL https://www.ncbi.nlm.nih.gov/pmc/articles/PMC5441687/.

Jessy D. Dorn and Dario L. Ringach. Estimating Membrane Voltage Correlations From Extracellular Spike Trains. *Journal of Neurophysiology*, 89(4):2271–2278, April 2003. ISSN 0022-3077. doi: 10.1152/jn.000889.2002. URL https://www.physiology.org/doi/full/10.1152/jn.000889.2002.

Kenji Doya. Universality of Fully-Connected Recurrent Neural Networks. Technical report, IEEE Transactions on Neural, 1993.

Shaul Druckmann, Yoav Banitt, Albert Gidon, Felix Schürmann, Henry Markram, and Idan Segev. A Novel Multiple Objective Optimization Framework for Constraining Conductance-Based Neuron Models by Experimental Data. *Frontiers in Neuroscience*, 1(1):7–18, October 2007. ISSN 1662-4548. doi: 10.3389/neuro.01.1.1.001.2007. URL https://www.ncbi.nlm.nih.gov/pmc/articles/PMC2570085/.

Edmund Optics. Using tube lenses with infinity corrected objectives. URL https://www.edmundoptics.com/resources/application-notes/microscopy/using-tube-lenses-with-infinity-corrected-objectives/.

David Eriksson, Tamas Tompa, and Per E. Roland. Non-Linear Population Firing Rates and Voltage Sensitive Dye Signals in Visual Areas 17 and 18 to Short Duration Stimuli. *PLOS ONE*, 3(7):e2673, July 2008. ISSN 1932-6203. doi: 10.1371/journal.pone.0002673. URL https://journals.plos.org/plosone/article?id=10.1371/journal.pone.0002673.

Tamás Dávid Fehérvári, Yuka Okazaki, Hajime Sawai, and Tetsuya Yagi. In Vivo Voltage-Sensitive Dye Study of Lateral Spreading of Cortical Activity in Mouse Primary Visual Cortex Induced by a Current Impulse. *PLOS ONE*, 10(7):e0133853, July 2015. ISSN 1932-6203. doi: 10.1371/journal.pone.0133853. URL http://journals.plos.org/plosone/article?id=10.1371/journal.pone.0133853.

Isabelle Ferezou, Sonia Bolea, and Carl C. H. Petersen. Visualizing the Cortical Representation of Whisker Touch: Voltage-Sensitive Dye Imaging in Freely Moving Mice. *Neuron*, 50 (4):617–629, May 2006. ISSN 0896-6273. doi: 10.1016/j.neuron.2006.03.043. URL http://www.sciencedirect.com/science/article/pii/S0896627306002704.

Isabelle Ferezou, Florent Haiss, Luc J. Gentet, Rachel Aronoff, Bruno Weber, and Carl C. H. Petersen. Spatiotemporal Dynamics of Cortical Sensorimotor Integration in Behaving Mice. *Neuron*, 56(5):907–923, December 2007. ISSN 0896-6273. doi: 10.1016/j.neuron.2007.10.007. URL http://www.sciencedirect.com/science/article/pii/S0896627307007635.

Isabelle Ferezou, Ferenc Matyas, and Carl C. H. Petersen. Imaging the Brain in Action: Real-Time Voltage- Sensitive Dye Imaging of Sensorimotor Cortex of Awake Behaving Mice. In Ron D. Frostig, editor, *In Vivo Optical Imaging of Brain Function*, Frontiers in Neuroscience. CRC Press/Taylor & Francis, Boca Raton (FL), 2nd edition, 2009. ISBN 978-1-4200-7684-4. URL http://www.ncbi.nlm.nih.gov/books/NBK20229/.

Elodie Fino and Rafael Yuste. Dense Inhibitory Connectivity in Neocortex. *Neuron*, 69(6): 1188–1203, March 2011. ISSN 0896-6273. doi: 10.1016/j.neuron.2011.02.025. URL https://www.cell.com/neuron/abstract/S0896-6273(11)00123-1.

Andreas Frick, Dirk Feldmeyer, Moritz Helmstaedter, and Bert Sakmann. Monosynaptic connections between pairs of L5a pyramidal neurons in columns of juvenile rat somatosensory cortex. *Cerebral Cortex (New York, N.Y.: 1991)*, 18(2):397–406, February 2008. ISSN 1460-2199. doi: 10.1093/cercor/bhm074.

Bibliography

R. D. Frostig, E. E. Lieke, D. Y. Ts'o, and A. Grinvald. Cortical functional architecture and local coupling between neuronal activity and the microcirculation revealed by in vivo high-resolution optical imaging of intrinsic signals. *Proceedings of the National Academy of Sciences*, 87(16):6082–6086, August 1990. ISSN 0027-8424, 1091-6490. doi: 10.1073/pnas.87.16.6082. URL https://www.pnas.org/content/87/16/6082.

Wulfram Gerstner, Henning Sprekeler, and Gustavo Deco. Theory and Simulation in Neuroscience. *Science*, 338(6103):60–65, October 2012. ISSN 0036-8075, 1095-9203. doi: 10.1126/science.1227356. URL http://science.sciencemag.org/content/338/6103/60.

Ziv Gil, Barry W. Connors, and Yael Amitai. Efficacy of Thalamocortical and Intracortical Synaptic Connections: Quanta, Innervation, and Reliability. *Neuron*, 23(2):385–397, June 1999. ISSN 0896-6273. doi: 10.1016/S0896-6273(00)80788-6. URL http://www.sciencedirect.com/science/article/pii/S0896627300807886.

Marc Gleichmann and Mark P. Mattson. Neuronal Calcium Homeostasis and Dysregulation. *Antioxidants & Redox Signaling*, 14(7):1261–1273, July 2010. ISSN 1523-0864. doi: 10.1089/ars.2010.3386. URL https://www.liebertpub.com/doi/full/10.1089/ars.2010.3386.

Clare A. Gollnick, Daniel C. Millard, Alexander D. Ortiz, Ravi V. Bellamkonda, and Garrett B. Stanley. Response reliability observed with voltage-sensitive dye imaging of cortical layer 2/3: the probability of activation hypothesis. *Journal of Neurophysiology*, 115(5):2456–2469, May 2016. ISSN 0022-3077, 1522-1598. doi: 10.1152/jn.00547.2015. URL http://jn.physiology.org/content/115/5/2456.

Yuri Gonchar, Stephen Turney, Joseph L. Price, and Andreas Burkhalter. Axo-axonic synapses formed by somatostatin-expressing GABAergic neurons in rat and monkey visual cortex. *J. Comp. Neurol.*, 443(1):1–14, January 2002. ISSN 0021-9967. doi: 10.1002/cne.1425.

Guillermo González-Burgos, German Barrionuevo, and David A. Lewis. Horizontal Synaptic Connections in Monkey Prefrontal Cortex: An In Vitro Electrophysiological Study. *Cerebral Cortex*, 10(1):82–92, January 2000. ISSN 1047-3211. doi: 10.1093/cercor/10.1.82. URL https://academic.oup.com/cercor/article/10/1/82/377115.

David S. Greenberg, Arthur R. Houweling, and Jason N. D. Kerr. Population imaging of ongoing neuronal activity in the visual cortex of awake rats. *Nature Neuroscience*, 11(7):749–751, July 2008. ISSN 1546-1726. doi: 10.1038/nn.2140. URL https://www.nature.com/articles/nn.2140.

Michael D. Greicius, Gaurav Srivastava, Allan L. Reiss, and Vinod Menon. Default-mode network activity distinguishes Alzheimer's disease from healthy aging: Evidence from functional MRI. *Proceedings of the National Academy of Sciences*, 101(13):4637–4642, March 2004. ISSN 0027-8424, 1091-6490. doi: 10.1073/pnas.0308627101. URL https://www.pnas.org/content/101/13/4637.

Bram de Greve. Reflections and Refractions in Ray Tracing. 2004.

Benjamin F. Grewe, Audrey Bonnan, and Andreas Frick. Back-propagation of physiological action potential output in dendrites of slender-tufted L5a pyramidal neurons. *Frontiers in Cellular Neuroscience*, 4, 2010. ISSN 1662-5102. doi: 10.3389/fncel.2010.00013. URL https://www.frontiersin.org/articles/10.3389/fncel.2010.00013/full.

A. Grinvald, B. M. Salzberg, and L. B. Cohen. Simultaneous recording from several neurones in an invertebrate central nervous system. *Nature*, 268(5616):140–142, July 1977. ISSN 1476-4687. doi: 10.1038/268140a0. URL https://www.nature.com/articles/268140a0.

A. Grinvald, R. Hildesheim, I. C. Farber, and L. Anglister. Improved fluorescent probes for the measurement of rapid changes in membrane potential. *Biophysical Journal*, 39(3): 301–308, September 1982a. ISSN 0006-3495. doi: 10.1016/S0006-3495(82)84520-7. URL http://www.sciencedirect.com/science/article/pii/S0006349582845207.

A. Grinvald, A. Manker, and M. Segal. Visualization of the spread of electrical activity in rat hippocampal slices by voltage-sensitive optical probes. *The Journal of Physiology*, 333(1): 269–291, December 1982b. ISSN 0022-3751. doi: 10.1113/jphysiol.1982.sp014453. URL https://physoc.onlinelibrary.wiley.com/doi/abs/10.1113/jphysiol.1982.sp014453.

A. Grinvald, L. Anglister, J. A. Freeman, R. Hildesheim, and A. Manker. Real-time optical imaging of naturally evoked electrical activity in intact frog brain. *Nature*, 308(5962):848–850, April 1984. ISSN 1476-4687. doi: 10.1038/308848a0. URL https://www.nature.com/articles/308848a0.

A. Grinvald, E. E. Lieke, R. D. Frostig, and R. Hildesheim. Cortical point-spread function and long-range lateral interactions revealed by real-time optical imaging of macaque monkey primary visual cortex. *Journal of Neuroscience*, 14(5):2545–2568, May 1994. ISSN 0270-6474, 1529-2401. doi: 10.1523/JNEUROSCI.14-05-02545.1994. URL https://www.jneurosci.org/content/14/5/2545.

Amiram Grinvald and Rina Hildesheim. VSDI: a new era in functional imaging of cortical dynamics. *Nature Reviews Neuroscience*, 5(11):874–885, November 2004. ISSN 1471-003X. doi: 10.1038/nrn1536. URL http://www.nature.com/nrn/journal/v5/n11/abs/nrn1536.html.

Amiram Grinvald and Carl C. H. Petersen. Imaging the Dynamics of Neocortical Population Activity in Behaving and Freely Moving Mammals. In Marco Canepari, Dejan Zecevic, and Olivier Bernus, editors, *Membrane Potential Imaging in the Nervous System and Heart*, Advances in Experimental Medicine and Biology, pages 273–296. Springer International Publishing, Cham, 2015. ISBN 978-3-319-17641-3. doi: 10.1007/978-3-319-17641-3_11. URL https://doi.org/10.1007/978-3-319-17641-3_11.

Amiram Grinvald, Edmund Lieke, Ron D. Frostig, Charles D. Gilbert, and Torsten N. Wiesel. Functional architecture of cortex revealed by optical imaging of intrinsic signals. *Nature*, 324(6095):361, November 1986. ISSN 1476-4687. doi: 10.1038/324361a0. URL https://www.nature.com/articles/324361a0.

Bibliography

Amiram Grinvald, D. Shoham, A. Shmuel, D. Glaser, I. Vanzetta, E. Shtoyerman, H. Slovin, C. Wijnbergen, R. Hildesheim, and A. Arieli. In-vivo Optical Imaging of Cortical Architecture and Dynamics. In Uwe Windhorst and Håkan Johansson, editors, *Modern Techniques in Neuroscience Research*, pages 893–969. Springer Berlin Heidelberg, Berlin, Heidelberg, 1999. ISBN 978-3-642-58552-4. doi: 10.1007/978-3-642-58552-4_34. URL https://doi.org/10.1007/978-3-642-58552-4_34.

Amiram Grinvald, David B. Omer, Dahlia Sharon, Ivo Vanzetta, and Rina Hildesheim. Voltage-Sensitive Dye Imaging of Neocortical Activity. *Cold Spring Harbor Protocols*, 2016(1): pdb.top089367, January 2016. ISSN 1940-3402, 1559-6095. doi: 10.1101/pdb.top089367. URL http://cshprotocols.cshlp.org/content/2016/1/pdb.top089367.

Allan T. Gulledge, Björn M. Kampa, and Greg J. Stuart. Synaptic integration in dendritic trees. *Journal of Neurobiology*, 64(1):75–90, 2005. ISSN 1097-4695. doi: 10.1002/neu.20144. URL https://onlinelibrary.wiley.com/doi/abs/10.1002/neu.20144.

A. Gupta, Y. Wang, and H. Markram. Organizing principles for a diversity of GABAergic interneurons and synapses in the neocortex. *Science (New York, N.Y.)*, 287(5451):273–278, January 2000. ISSN 0036-8075. doi: 10.1126/science.287.5451.273.

Barbara Gysbrechts, Nghia Nguyen Do Trong, Ling Wang, Henrique Cabral, Zaneta Navratilova, Francesco P. Battaglia, Wouter Saeys, and Carmen Bartic. Measurement of the optical properties of rat brain tissue using contact spatially resolved spectroscopy. volume 9129, pages 912936–912936–7, 2014. doi: 10.1117/12.2052367. URL http://dx.doi.org/10.1117/12.2052367.

Fritz A. Henn, Hengo Haljama¨e, and Anders Hamberger. Glial cell function: Active control of extracellular K+ concentration. *Brain Research*, 43(2):437–443, August 1972. ISSN 0006-8993. doi: 10.1016/0006-8993(72)90399-X. URL http://www.sciencedirect.com/science/article/pii/000689937290399X.

M. L. Hines and N. T. Carnevale. The NEURON Simulation Environment. *Neural Computation*, 9(6):1179–1209, August 1997. ISSN 0899-7667. doi: 10.1162/neco.1997.9.6.1179. URL https://doi.org/10.1162/neco.1997.9.6.1179.

Stuart W. Hughes, David W. Cope, Kate L. Blethyn, and Vincenzo Crunelli. Cellular Mechanisms of the Slow (<1 Hz) Oscillation in Thalamocortical Neurons In Vitro. *Neuron*, 33(6):947–958, March 2002. ISSN 0896-6273. doi: 10.1016/S0896-6273(02)00623-2. URL http://www.sciencedirect.com/science/article/pii/S0896627302006232.

Raoul Huys, Viktor K. Jirsa, Ziauddin Darokhan, Sonata Valentiniene, and Per E. Roland. Visually Evoked Spiking Evolves While Spontaneous Ongoing Dynamics Persist. *Front Syst Neurosci*, 9, January 2016. ISSN 1662-5137. doi: 10.3389/fnsys.2015.00183. URL https://www.ncbi.nlm.nih.gov/pmc/articles/PMC4705305/.

Jeffry S. Isaacson and Massimo Scanziani. How Inhibition Shapes Cortical Activity. *Neuron*, 72(2):231–243, October 2011. ISSN 0896-6273. doi: 10.1016/j.neuron.2011.09.027. URL https://www.cell.com/neuron/abstract/S0896-6273(11)00879-8.

Dirk Jancke, Frédéric Chavane, Shmuel Naaman, and Amiram Grinvald. Imaging cortical correlates of illusion in early visual cortex. *Nature*, 428(6981):423, March 2004. ISSN 1476-4687. doi: 10.1038/nature02396. URL https://www.nature.com/articles/nature02396.

Wenjun Jin, Ren-Ji Zhang, and Jian-young Wu. Voltage-sensitive dye imaging of population neuronal activity in cortical tissue. *Journal of Neuroscience Methods*, 115(1):13–27, March 2002. ISSN 0165-0270. doi: 10.1016/S0165-0270(01)00511-8. URL http://www.sciencedirect.com/science/article/pii/S0165027001005118.

Johannes D. Johansson. Spectroscopic method for determination of the absorption coefficient in brain tissue. *Journal of Biomedical Optics*, 15(5):057005–057005–9, 2010. ISSN 1083-3668. doi: 10.1117/1.3495719. URL http://dx.doi.org/10.1117/1.3495719.

Eric Jonas and Konrad Paul Kording. Could a Neuroscientist Understand a Microprocessor? *PLOS Computational Biology*, 13(1):e1005268, January 2017. ISSN 1553-7358. doi: 10.1371/journal.pcbi.1005268. URL https://journals.plos.org/ploscompbiol/article?id=10.1371/journal.pcbi.1005268.

H. C. Jones and R. F. Keep. Brain fluid calcium concentration and response to acute hypercalcaemia during development in the rat. *The Journal of Physiology*, 402:579–593, August 1988. ISSN 0022-3751. doi: 10.1113/jphysiol.1988.sp017223.

Yoshinao Kajikawa and Charles E. Schroeder. How local is the local field potential? *Neuron*, 72(5):847–858, December 2011. ISSN 0896-6273. doi: 10.1016/j.neuron.2011.09.029. URL https://www.ncbi.nlm.nih.gov/pmc/articles/PMC3240862/.

Karthik Kambatla, Giorgos Kollias, Vipin Kumar, and Ananth Grama. Trends in big data analytics. *Journal of Parallel and Distributed Computing*, 74(7):2561–2573, July 2014. ISSN 0743-7315. doi: 10.1016/j.jpdc.2014.01.003. URL http://www.sciencedirect.com/science/article/pii/S0743731514000057.

Christoph Kapfer, Lindsey L. Glickfeld, Bassam V. Atallah, and Massimo Scanziani. Supralinear increase of recurrent inhibition during sparse activity in the somatosensory cortex. *Nature Neuroscience*, 10(6):743–753, June 2007. ISSN 1097-6256. doi: 10.1038/nn1909.

Mahesh M Karnani, Masakazu Agetsuma, and Rafael Yuste. A blanket of inhibition: functional inferences from dense inhibitory connectivity. *Current Opinion in Neurobiology*, 26:96–102, June 2014. ISSN 0959-4388. doi: 10.1016/j.conb.2013.12.015. URL http://www.sciencedirect.com/science/article/pii/S0959438813002390.

Yasuo Kawaguchi. Pyramidal Cell Subtypes and Their Synaptic Connections in Layer 5 of Rat Frontal Cortex. *Cerebral Cortex*, 27(12):5755–5771, December 2017. ISSN 1047-3211. doi: 10.1093/cercor/bhx252. URL https://academic.oup.com/cercor/article/27/12/5755/4259744.

Bibliography

J. P. Kelly and D. C. Van Essen. Cell structure and function in the visual cortex of the cat. *The Journal of Physiology*, 238(3):515–547, May 1974. ISSN 1469-7793. doi: 10.1113/jphysiol. 1974.sp010541. URL https://physoc.onlinelibrary.wiley.com/doi/abs/10.1113/jphysiol.1974. sp010541.

D. Kleinfeld and K.r. Delaney. Distributed representation of vibrissa movement in the upper layers of somatosensory cortex revealed with voltage-sensitive dyes. *The Journal of Comparative Neurology*, 375(1):89–108, November 1996. ISSN 1096-9861. doi: 10.1002/(SICI) 1096-9861(19961104)375:1<89::AID-CNE6>3.0.CO;2-K. URL http://onlinelibrary.wiley. com/doi/10.1002/(SICI)1096-9861(19961104)375:1<89::AID-CNE6>3.0.CO;2-K/abstract.

C. P. J. De Kock, R. M. Bruno, H. Spors, and B. Sakmann. Layer- and cell-type-specific suprathreshold stimulus representation in rat primary somatosensory cortex. *The Journal of Physiology*, 581(1):139–154, May 2007. ISSN 1469-7793. doi: 10.1113/jphysiol.2006.124321. URL https://physoc.onlinelibrary.wiley.com/doi/abs/10.1113/jphysiol.2006.124321.

Helmut J. Koester and Bert Sakmann. Calcium dynamics in single spines during coincident pre- and postsynaptic activity depend on relative timing of back-propagating action potentials and subthreshold excitatory postsynaptic potentials. *Proceedings of the National Academy of Sciences*, 95(16):9596–9601, August 1998. ISSN 0027-8424, 1091-6490. doi: 10.1073/pnas. 95.16.9596. URL https://www.pnas.org/content/95/16/9596.

J. Koomey, S. Berard, M. Sanchez, and H. Wong. Implications of Historical Trends in the Electrical Efficiency of Computing. *IEEE Annals of the History of Computing*, 33(3):46–54, March 2011. ISSN 1058-6180. doi: 10.1109/MAHC.2010.28.

R. P. Kraio and C. Nicholson. Extracellular ionic variations during spreading depression. *Neuroscience*, 3(11):1045–1059, November 1978. ISSN 0306-4522. doi: 10.1016/0306-4522(78) 90122-7. URL http://www.sciencedirect.com/science/article/pii/0306452278901227.

Matthias Kreuzer, Harald Hentschke, Bernd Antkowiak, Cornelius Schwarz, Eberhard F. Kochs, and Gerhard Schneider. Cross-approximate entropy of cortical local field potentials quantifies effects of anesthesia - a pilot study in rats. *BMC Neuroscience*, 11 (1):122, September 2010. ISSN 1471-2202. doi: 10.1186/1471-2202-11-122. URL https: //doi.org/10.1186/1471-2202-11-122.

Nicola Kuczewski, Christophe Porcher, Nadine Ferrand, Hervé Fiorentino, Christophe Pellegrino, Richard Kolarow, Volkmar Lessmann, Igor Medina, and Jean-Luc Gaiarsa. Back-propagating Action Potentials Trigger Dendritic Release of BDNF during Spontaneous Network Activity. *The Journal of Neuroscience*, 28(27):7013–7023, July 2008. ISSN 0270-6474. doi: 10.1523/JNEUROSCI.1673-08.2008. URL https://www.ncbi.nlm.nih.gov/pmc/articles/ PMC6670985/.

Alexandre Kuhn, Ad Aertsen, and Stefan Rotter. Neuronal Integration of Synaptic Input in the Fluctuation-Driven Regime. *Journal of Neuroscience*, 24(10):2345–2356, March 2004. ISSN

0270-6474, 1529-2401. doi: 10.1523/JNEUROSCI.3349-03.2004. URL https://www.jneurosci.org/content/24/10/2345.

Alexandros Kyriakatos, Vijay Sadashivaiah, Yifei Zhang, Alessandro Motta, Matthieu Auffret, and Carl C. H. Petersen. Voltage-sensitive dye imaging of mouse neocortex during a whisker detection task. *Neurophotonics*, 4(3), July 2017. ISSN 2329-423X. doi: 10.1117/1.NPh.4.3.031204. URL https://www.ncbi.nlm.nih.gov/pmc/articles/PMC5120151/.

Raphael Lamprecht and Joseph LeDoux. Structural plasticity and memory. *Nature Reviews. Neuroscience*, 5(1):45–54, January 2004. ISSN 1471-003X. doi: 10.1038/nrn1301.

Matthew E. Larkum, J. Julius Zhu, and Bert Sakmann. A new cellular mechanism for coupling inputs arriving at different cortical layers. *Nature*, 398(6725):338–341, March 1999. ISSN 1476-4687. doi: 10.1038/18686. URL https://www.nature.com/articles/18686.

Jean-Vincent Le Bé and Henry Markram. Spontaneous and evoked synaptic rewiring in the neonatal neocortex. *Proceedings of the National Academy of Sciences of the United States of America*, 103(35):13214–13219, August 2006. ISSN 0027-8424. doi: 10.1073/pnas.0604691103.

Nuo Li, Tsai-Wen Chen, Zengcai V. Guo, Charles R. Gerfen, and Karel Svoboda. A motor cortex circuit for motor planning and movement. *Nature*, 519(7541):51–56, March 2015. ISSN 1476-4687. doi: 10.1038/nature14178. URL https://www.nature.com/articles/nature14178.

D. S. Ling and L. S. Benardo. Restrictions on inhibitory circuits contribute to limited recruitment of fast inhibition in rat neocortical pyramidal cells. *Journal of Neurophysiology*, 82(4):1793–1807, October 1999. ISSN 0022-3077. doi: 10.1152/jn.1999.82.4.1793.

Michael Lippert, Kentaroh Takagaki, Weifeng Xu, Xiaoying Huang, and Jian-Young Wu. Methods for voltage-sensitive dye imaging of rat cortical activity with high signal-to-noise ratio. *Journal of neurophysiology*, 98(1):502–512, July 2007. ISSN 0022-3077. doi: 10.1152/jn.01169.2006. URL https://www.ncbi.nlm.nih.gov/pmc/articles/PMC2855339/.

Artur Luczak, Peter Barthó, Stephan L. Marguet, György Buzsáki, and Kenneth D. Harris. Sequential structure of neocortical spontaneous activity in vivo. *Proceedings of the National Academy of Sciences*, 104(1):347–352, January 2007. ISSN 0027-8424, 1091-6490. doi: 10.1073/pnas.0605643104. URL https://www.pnas.org/content/104/1/347.

Brian R. Lustig, Robert M. Friedman, Jeremy E. Winberry, Ford F. Ebner, and Anna W. Roe. Voltage-sensitive dye imaging reveals shifting spatiotemporal spread of whisker-induced activity in rat barrel cortex. *Journal of Neurophysiology*, 109(9):2382–2392, May 2013. ISSN 0022-3077, 1522-1598. doi: 10.1152/jn.00430.2012. URL http://jn.physiology.org/content/109/9/2382.

Jason N. MacLean, Brendon O. Watson, Gloster B. Aaron, and Rafael Yuste. Internal Dynamics Determine the Cortical Response to Thalamic Stimulation. *Neuron*, 48(5):811–

Bibliography

823, December 2005. ISSN 0896-6273. doi: 10.1016/j.neuron.2005.09.035. URL http://www.sciencedirect.com/science/article/pii/S0896627305010019.

Bu-Qing Mao, Farid Hamzei-Sichani, Dmitriy Aronov, Robert C Froemke, and Rafael Yuste. Dynamics of Spontaneous Activity in Neocortical Slices. *Neuron*, 32(5):883–898, December 2001. ISSN 0896-6273. doi: 10.1016/S0896-6273(01)00518-9. URL http://www.sciencedirect.com/science/article/pii/S0896627301005189.

Valentin Markounikau, Christian Igel, Amiram Grinvald, and Dirk Jancke. A Dynamic Neural Field Model of Mesoscopic Cortical Activity Captured with Voltage-Sensitive Dye Imaging. *PLoS Computational Biology*, 6(9), September 2010. ISSN 1553-734X. doi: 10.1371/journal.pcbi.1000919. URL https://www.ncbi.nlm.nih.gov/pmc/articles/PMC2936513/.

H. Markram, J. Lübke, M. Frotscher, A. Roth, and B. Sakmann. Physiology and anatomy of synaptic connections between thick tufted pyramidal neurones in the developing rat neocortex. *The Journal of Physiology*, 500 (Pt 2):409–440, April 1997. ISSN 0022-3751. doi: 10.1113/jphysiol.1997.sp022031.

Henry Markram. The Blue Brain Project. *Nature Reviews Neuroscience*, 7(2):153–160, February 2006. ISSN 1471-0048. doi: 10.1038/nrn1848. URL https://www.nature.com/articles/nrn1848.

Henry Markram, Eilif Muller, Srikanth Ramaswamy, Michael W. Reimann, Marwan Abdellah, Carlos Aguado Sanchez, Anastasia Ailamaki, Lidia Alonso-Nanclares, Nicolas Antille, Selim Arsever, Guy Antoine Atenekeng Kahou, Thomas K. Berger, Ahmet Bilgili, Nenad Buncic, Athanassia Chalimourda, Giuseppe Chindemi, Jean-Denis Courcol, Fabien Delalondre, Vincent Delattre, Shaul Druckmann, Raphael Dumusc, James Dynes, Stefan Eilemann, Eyal Gal, Michael Emiel Gevaert, Jean-Pierre Ghobril, Albert Gidon, Joe W. Graham, Anirudh Gupta, Valentin Haenel, Etay Hay, Thomas Heinis, Juan B. Hernando, Michael Hines, Lida Kanari, Daniel Keller, John Kenyon, Georges Khazen, Yihwa Kim, James G. King, Zoltan Kisvarday, Pramod Kumbhar, Sébastien Lasserre, Jean-Vincent Le Bé, Bruno R. C. Magalhães, Angel Merchán-Pérez, Julie Meystre, Benjamin Roy Morrice, Jeffrey Muller, Alberto Muñoz-Céspedes, Shruti Muralidhar, Keerthan Muthurasa, Daniel Nachbaur, Taylor H. Newton, Max Nolte, Aleksandr Ovcharenko, Juan Palacios, Luis Pastor, Rodrigo Perin, Rajnish Ranjan, Imad Riachi, José-Rodrigo Rodríguez, Juan Luis Riquelme, Christian Rössert, Konstantinos Sfyrakis, Ying Shi, Julian C. Shillcock, Gilad Silberberg, Ricardo Silva, Farhan Tauheed, Martin Telefont, Maria Toledo-Rodriguez, Thomas Tränkler, Werner Van Geit, Jafet Villafranca Díaz, Richard Walker, Yun Wang, Stefano M. Zaninetta, Javier DeFelipe, Sean L. Hill, Idan Segev, and Felix Schürmann. Reconstruction and Simulation of Neocortical Microcircuitry. *Cell*, 163(2):456–492, October 2015. ISSN 0092-8674, 1097-4172. doi: 10.1016/j.cell.2015.09.029. URL https://www.cell.com/cell/abstract/S0092-8674(15)01191-5.

C. T. McDonald and A. Burkhalter. Organization of long-range inhibitory connections with rat visual cortex. *The Journal of Neuroscience: The Official Journal of the Society for Neuroscience*, 13(2):768–781, February 1993. ISSN 0270-6474.

David A. McVea, Majid H. Mohajerani, and Timothy H. Murphy. Voltage-Sensitive Dye Imaging Reveals Dynamic Spatiotemporal Properties of Cortical Activity after Spontaneous Muscle Twitches in the Newborn Rat. *Journal of Neuroscience*, 32(32):10982–10994, August 2012. ISSN 0270-6474, 1529-2401. doi: 10.1523/JNEUROSCI.1322-12.2012. URL http://www.jneurosci.org/content/32/32/10982.

Juan Mena-Segovia, Hana M. Sims, Peter J. Magill, and J. Paul Bolam. Cholinergic brainstem neurons modulate cortical gamma activity during slow oscillations. *The Journal of Physiology*, 586(12):2947–2960, 2008. ISSN 1469-7793. doi: 10.1113/jphysiol.2008.153874. URL https://physoc.onlinelibrary.wiley.com/doi/abs/10.1113/jphysiol.2008.153874.

Steven Mennerick, Mariangela Chisari, Hong-Jin Shu, Amanda Taylor, Michael Vasek, Lawrence N. Eisenman, and Charles F. Zorumski. Diverse voltage-sensitive dyes modulate GABAA receptor function. *J. Neurosci.*, 30(8):2871–2879, February 2010. ISSN 1529-2401. doi: 10.1523/JNEUROSCI.5607-09.2010.

Mohammed Mesradi, Aurelie Genoux, Vesna Cuplov, Darine Abi Haidar, Sebastien Jan, Irene Buvat, and Frederic Pain. Experimental and analytical comparative study of optical coefficient of fresh and frozen rat tissues. *Journal of Biomedical Optics*, 18(11):117010, November 2013. ISSN 1560-2281. doi: 10.1117/1.JBO.18.11.117010.

Hanno S. Meyer, Verena C. Wimmer, Mike Hemberger, Randy M. Bruno, Christiaan P. J. de Kock, Andreas Frick, Bert Sakmann, and Moritz Helmstaedter. Cell Type–Specific Thalamic Innervation in a Column of Rat Vibrissal Cortex. *Cerebral Cortex*, 20(10):2287–2303, October 2010. ISSN 1047-3211. doi: 10.1093/cercor/bhq069. URL https://academic.oup.com/cercor/article/20/10/2287/320324.

Kristina D Micheva, Dylan Wolman, Brett D Mensh, Elizabeth Pax, JoAnn Buchanan, Stephen J Smith, and Davi D Bock. A large fraction of neocortical myelin ensheathes axons of local inhibitory neurons. *eLife*, 5. ISSN 2050-084X. doi: 10.7554/eLife.15784. URL https://www.ncbi.nlm.nih.gov/pmc/articles/PMC4972537/.

Victor Minces, Lucas Pinto, Yang Dan, and Andrea A. Chiba. Cholinergic shaping of neural correlations. *Proceedings of the National Academy of Sciences of the United States of America*, 114(22):5725–5730, May 2017. ISSN 0027-8424. doi: 10.1073/pnas.1621493114. URL https://www.ncbi.nlm.nih.gov/pmc/articles/PMC5465883/.

Majid H. Mohajerani, David A. McVea, Matthew Fingas, and Timothy H. Murphy. Mirrored Bilateral Slow-Wave Cortical Activity within Local Circuits Revealed by Fast Bihemispheric Voltage-Sensitive Dye Imaging in Anesthetized and Awake Mice. *The Journal of Neuroscience*, 30(10):3745–3751, March 2010. ISSN 0270-6474, 1529-2401. doi: 10.1523/JNEUROSCI.6437-09.2010. URL http://www.jneurosci.org/content/30/10/3745.

Majid H. Mohajerani, Allen W. Chan, Mostafa Mohsenvand, Jeffrey LeDue, Rui Liu, David A. McVea, Jamie D. Boyd, Yu Tian Wang, Mark Reimers, and Timothy H. Murphy. Spontaneous cortical activity alternates between motifs defined by regional axonal projections. *Nature*

Neuroscience, 16(10):1426–1435, October 2013. ISSN 1097-6256. doi: 10.1038/nn.3499. URL http://www.nature.com/neuro/journal/v16/n10/abs/nn.3499.html.

Paul Muir, Shantao Li, Shaoke Lou, Daifeng Wang, Daniel J. Spakowicz, Leonidas Salichos, Jing Zhang, George M. Weinstock, Farren Isaacs, Joel Rozowsky, and Mark Gerstein. The real cost of sequencing: scaling computation to keep pace with data generation. *Genome Biology*, 17(1):53, March 2016. ISSN 1474-760X. doi: 10.1186/s13059-016-0917-0. URL https://doi.org/10.1186/s13059-016-0917-0.

Eilif Muller, Lars Buesing, Johannes Schemmel, and Karlheinz Meier. Spike-frequency adapting neural ensembles: beyond mean adaptation and renewal theories. *Neural Computation*, 19 (11):2958–3010, November 2007. ISSN 0899-7667. doi: 10.1162/neco.2007.19.11.2958.

Michael Murphy, Marie-Aurélie Bruno, Brady A. Riedner, Pierre Boveroux, Quentin Noirhomme, Eric C. Landsness, Jean-Francois Brichant, Christophe Phillips, Marcello Massimini, Steven Laureys, Giulio Tononi, and Mélanie Boly. Propofol Anesthesia and Sleep: A High-Density EEG Study. *Sleep*, 34(3):283–291, March 2011. ISSN 0161-8105. doi: 10.1093/sleep/34.3.283. URL https://academic.oup.com/sleep/article/34/3/283/2433788.

Hiroki Mutoh, Yukiko Mishina, Yasir Gallero-Salas, and Thomas Knöpfel. Comparative performance of a genetically-encoded voltage indicator and a blue voltage sensitive dye for large scale cortical voltage imaging. *Frontiers in Cellular Neuroscience*, 9, 2015. ISSN 1662-5102. doi: 10.3389/fncel.2015.00147. URL https://www.frontiersin.org/articles/10.3389/fncel.2015.00147/full.

Thai Nguyen. Total Number of Synapses in the Adult Human Neocortex. *Undergraduate Journal of Mathematical Modeling: One Two*, 3(1), January 2010. ISSN 2326-3652. doi: http://dx.doi.org/10.5038/2326-3652.3.1.26. URL https://scholarcommons.usf.edu/ujmm/vol3/iss1/26.

Michael Okun and Ilan Lampl. Instantaneous correlation of excitation and inhibition during ongoing and sensory-evoked activities. *Nature Neuroscience*, 11(5):535–537, May 2008. ISSN 1097-6256. doi: 10.1038/nn.2105.

Michael Okun, Nicholas A. Steinmetz, Lee Cossell, M. Florencia Iacaruso, Ho Ko, Péter Barthó, Tirin Moore, Sonja B. Hofer, Thomas D. Mrsic-Flogel, Matteo Carandini, and Kenneth D. Harris. Diverse coupling of neurons to populations in sensory cortex. *Nature*, 521(7553): 511–515, May 2015. ISSN 0028-0836. doi: 10.1038/nature14273. URL http://www.nature.com/nature/journal/v521/n7553/abs/nature14273.html.

Brett G. Olivier, Maciej J. Swat, and Martijn J. Moné. Modeling and Simulation Tools: From Systems Biology to Systems Medicine. In Ulf Schmitz and Olaf Wolkenhauer, editors, *Systems Medicine*, Methods in Molecular Biology, pages 441–463. Springer New York, New York, NY, 2016. ISBN 978-1-4939-3283-2. doi: 10.1007/978-1-4939-3283-2_19. URL https://doi.org/10.1007/978-1-4939-3283-2_19.

H. S. Orbach and L. B. Cohen. Optical monitoring of activity from many areas of the in vitro and in vivo salamander olfactory bulb: a new method for studying functional organization in the vertebrate central nervous system. *Journal of Neuroscience*, 3(11):2251–2262, November 1983. ISSN 0270-6474, 1529-2401. doi: 10.1523/JNEUROSCI.03-11-02251.1983. URL https://www.jneurosci.org/content/3/11/2251.

H. S. Orbach, L. B. Cohen, and A. Grinvald. Optical mapping of electrical activity in rat somatosensory and visual cortex. *Journal of Neuroscience*, 5(7):1886–1895, July 1985. ISSN 0270-6474, 1529-2401. doi: 10.1523/JNEUROSCI.05-07-01886.1985. URL http://www.jneurosci.org/content/5/7/1886.

Carl C. H. Petersen. The Functional Organization of the Barrel Cortex. *Neuron*, 56(2):339–355, October 2007. ISSN 0896-6273. doi: 10.1016/j.neuron.2007.09.017. URL http://www.sciencedirect.com/science/article/pii/S0896627307007155.

Carl C. H. Petersen and Bert Sakmann. Functionally Independent Columns of Rat Somatosensory Barrel Cortex Revealed with Voltage-Sensitive Dye Imaging. *Journal of Neuroscience*, 21(21):8435–8446, November 2001. ISSN 0270-6474, 1529-2401. URL http://www.jneurosci.org/content/21/21/8435.

Carl C. H. Petersen, Amiram Grinvald, and Bert Sakmann. Spatiotemporal Dynamics of Sensory Responses in Layer 2/3 of Rat Barrel Cortex Measured In Vivo by Voltage-Sensitive Dye Imaging Combined with Whole-Cell Voltage Recordings and Neuron Reconstructions. *The Journal of Neuroscience*, 23(4):1298–1309, February 2003a. ISSN 0270-6474, 1529-2401. URL http://www.jneurosci.org/content/23/4/1298.

Carl C. H. Petersen, Thomas T. G. Hahn, Mayank Mehta, Amiram Grinvald, and Bert Sakmann. Interaction of sensory responses with spontaneous depolarization in layer 2/3 barrel cortex. *Proceedings of the National Academy of Sciences*, 100(23):13638–13643, November 2003b. ISSN 0027-8424, 1091-6490. doi: 10.1073/pnas.2235811100. URL http://www.pnas.org/content/100/23/13638.

Carl C. H. Petersen and Sylvain Crochet. Synaptic Computation and Sensory Processing in Neocortical Layer 2/3. *Neuron*, 78(1):28–48, April 2013. ISSN 0896-6273. doi: 10.1016/j.neuron.2013.03.020. URL http://www.sciencedirect.com/science/article/pii/S0896627313002675.

Matt Pharr, Wenzel Jakob, and Greg Humphreys. *Physically Based Rendering: From Theory to Implementation*. Morgan Kaufmann Publishers Inc., San Francisco, CA, USA, 3rd edition, 2016. ISBN 978-0-12-800645-0.

Pasko Rakic. Evolution of the neocortex: Perspective from developmental biology. *Nature reviews. Neuroscience*, 10(10):724–735, October 2009. ISSN 1471-003X. doi: 10.1038/nrn2719. URL https://www.ncbi.nlm.nih.gov/pmc/articles/PMC2913577/.

Rune Rasmussen, Mogens H. Jensen, and Mathias L. Heltberg. Chaotic Dynamics Mediate Brain State Transitions, Driven by Changes in Extracellular Ion Concentrations. *Cell Systems*,

Bibliography

5(6):591–603.e4, December 2017. ISSN 2405-4712. doi: 10.1016/j.cels.2017.11.011. URL https://www.cell.com/cell-systems/abstract/S2405-4712(17)30539-2.

Eugene H. Ratzlaff and Amiram Grinvald. A tandem-lens epifluorescence macroscope: Hundred-fold brightness advantage for wide-field imaging. *Journal of Neuroscience Methods*, 36(2):127–137, February 1991. ISSN 0165-0270. doi: 10.1016/0165-0270(91)90038-2. URL http://www.sciencedirect.com/science/article/pii/0165027091900382.

Michael W. Reimann, Costas A. Anastassiou, Rodrigo Perin, Sean L. Hill, Henry Markram, and Christof Koch. A Biophysically Detailed Model of Neocortical Local Field Potentials Predicts the Critical Role of Active Membrane Currents. *Neuron*, 79(2):375–390, July 2013. ISSN 0896-6273. doi: 10.1016/j.neuron.2013.05.023. URL http://www.cell.com/neuron/abstract/S0896-6273(13)00443-1.

Michael W. Reimann, James G. King, Eilif B. Muller, Srikanth Ramaswamy, and Henry Markram. An algorithm to predict the connectome of neural microcircuits. *Frontiers in Computational Neuroscience*, 9, October 2015. ISSN 1662-5188. doi: 10.3389/fncom.2015.00120. URL https://www.ncbi.nlm.nih.gov/pmc/articles/PMC4597796/.

Michael W. Reimann, Michael Gevaert, Ying Shi, Huanxiang Lu, Henry Markram, and Eilif Muller. A null model of the mouse whole-neocortex micro-connectome. *Nat Commun*, 10(1):1–16, August 2019. ISSN 2041-1723. doi: 10.1038/s41467-019-11630-x. URL https://www.nature.com/articles/s41467-019-11630-x.

Vicente Reyes-Puerta, Jyh-Jang Sun, Suam Kim, Werner Kilb, and Heiko J. Luhmann. Laminar and Columnar Structure of Sensory-Evoked Multineuronal Spike Sequences in Adult Rat Barrel Cortex In Vivo. *Cerebral Cortex (New York, N.Y.: 1991)*, 25(8):2001–2021, August 2015. ISSN 1460-2199. doi: 10.1093/cercor/bhu007.

Mengia-S. Rioult-Pedotti, Daniel Friedman, and John P. Donoghue. Learning-Induced LTP in Neocortex. *Science*, 290(5491):533–536, October 2000. ISSN 0036-8075, 1095-9203. doi: 10.1126/science.290.5491.533. URL https://science.sciencemag.org/content/290/5491/533.

Per E. Roland. Space-Time Dynamics of Membrane Currents Evolve to Shape Excitation, Spiking, and Inhibition in the Cortex at Small and Large Scales. *Neuron*, 94(5):934–942, June 2017. ISSN 1097-4199. doi: 10.1016/j.neuron.2017.04.038.

Per E. Roland, Akitoshi Hanazawa, Calle Undeman, David Eriksson, Tamas Tompa, Hiroyuki Nakamura, Sonata Valentiniene, and Bashir Ahmed. Cortical feedback depolarization waves: A mechanism of top-down influence on early visual areas. *Proceedings of the National Academy of Sciences*, 103(33):12586–12591, August 2006. ISSN 0027-8424, 1091-6490. doi: 10.1073/pnas.0604925103. URL https://www.pnas.org/content/103/33/12586.

Per E. Roland, Claus C. Hilgetag, and Gustavo Deco. Cortico-cortical communication dynamics. *Front. Syst. Neurosci.*, 8, 2014. ISSN 1662-5137. doi: 10.3389/fnsys.2014.00019. URL https://www.frontiersin.org/articles/10.3389/fnsys.2014.00019/full.

Sandrine Romand, Yun Wang, Maria Toledo-Rodriguez, and Henry Markram. Morphological development of thick-tufted layer v pyramidal cells in the rat somatosensory cortex. *Frontiers in Neuroanatomy*, 5:5, 2011. ISSN 1662-5129. doi: 10.3389/fnana.2011.00005.

W. N. Ross, B. M. Salzberg, L. B. Cohen, A. Grinvald, H. V. Davila, A. S. Waggoner, and C. H. Wang. Changes in absorption, fluorescence, dichroism, and birefringence in stained giant axons: Optical measurement of membrane potential. *The Journal of Membrane Biology*, 33 (1):141–183, December 1977. ISSN 0022-2631, 1432-1424. doi: 10.1007/BF01869514. URL https://link.springer.com/article/10.1007/BF01869514.

A. Rozov, N. Burnashev, B. Sakmann, and E. Neher. Transmitter release modulation by intracellular Ca2+ buffers in facilitating and depressing nerve terminals of pyramidal cells in layer 2/3 of the rat neocortex indicates a target cell-specific difference in presynaptic calcium dynamics. *The Journal of Physiology*, 531(Pt 3):807–826, March 2001. ISSN 0022-3751. doi: 10.1111/j.1469-7793.2001.0807h.x.

Michael Rudolph, Zuzanna Piwkowska, Mathilde Badoual, Thierry Bal, and Alain Destexhe. A Method to Estimate Synaptic Conductances From Membrane Potential Fluctuations. *Journal of Neurophysiology*, 91(6):2884–2896, June 2004. ISSN 0022-3077. doi: 10.1152/jn. 01223.2003. URL https://www.physiology.org/doi/full/10.1152/jn.01223.2003.

Michael Rudolph, Joe Guillaume Pelletier, Denis Paré, and Alain Destexhe. Characterization of Synaptic Conductances and Integrative Properties During Electrically Induced EEG-Activated States in Neocortical Neurons In Vivo. *Journal of Neurophysiology*, 94(4):2805–2821, October 2005. ISSN 0022-3077. doi: 10.1152/jn.01313.2004. URL https://www.physiology.org/doi/full/10.1152/jn.01313.2004.

Matthew D. Sacchet, Roan A. LaPlante, Qian Wan, Dominique L. Pritchett, Adrian K. C. Lee, Matti Hämäläinen, Christopher I. Moore, Catherine E. Kerr, and Stephanie R. Jones. Attention Drives Synchronization of Alpha and Beta Rhythms between Right Inferior Frontal and Primary Sensory Neocortex. *Journal of Neuroscience*, 35(5):2074–2082, February 2015. ISSN 0270-6474, 1529-2401. doi: 10.1523/JNEUROSCI.1292-14.2015. URL https://www.jneurosci.org/content/35/5/2074.

Bradley L. Schlaggar and Dennis D. M. O'Leary. Early development of the somatotopic map and barrel patterning in rat somatosensory cortex. *Journal of Comparative Neurology*, 346 (1):80–96, 1994. ISSN 1096-9861. doi: 10.1002/cne.903460106. URL https://onlinelibrary. wiley.com/doi/abs/10.1002/cne.903460106.

Indra Schroeder. How to resolve microsecond current fluctuations in single ion channels: The power of beta distributions. *Channels*, 9(5):262–280, September 2015. ISSN 1933-6950. doi: 10.1080/19336950.2015.1083660. URL https://www.ncbi.nlm.nih.gov/pmc/articles/PMC4826091/.

James Schummers, Hongbo Yu, and Mriganka Sur. Tuned Responses of Astrocytes and Their Influence on Hemodynamic Signals in the Visual Cortex. *Science*, 320(5883):1638–1643,

Bibliography

June 2008. ISSN 0036-8075, 1095-9203. doi: 10.1126/science.1156120. URL https://science.sciencemag.org/content/320/5883/1638.

Biswa Sengupta, Simon B. Laughlin, and Jeremy E. Niven. Balanced Excitatory and Inhibitory Synaptic Currents Promote Efficient Coding and Metabolic Efficiency. *PLOS Computational Biology*, 9(10):e1003263, October 2013. ISSN 1553-7358. doi: 10.1371/journal.pcbi.1003263. URL https://journals.plos.org/ploscompbiol/article?id=10.1371/journal.pcbi.1003263.

Dahlia Sharon and Amiram Grinvald. Dynamics and Constancy in Cortical Spatiotemporal Patterns of Orientation Processing. *Science*, 295(5554):512–515, January 2002. ISSN 0036-8075, 1095-9203. doi: 10.1126/science.1065916. URL https://science.sciencemag.org/content/295/5554/512.

Doron Shoham, Daniel E. Glaser, Amos Arieli, Tal Kenet, Chaipi Wijnbergen, Yuval Toledo, Rina Hildesheim, and Amiram Grinvald. Imaging Cortical Dynamics at High Spatial and Temporal Resolution with Novel Blue Voltage-Sensitive Dyes. *Neuron*, 24(4):791–802, December 1999. ISSN 0896-6273. doi: 10.1016/S0896-6273(00)81027-2. URL http://www.cell.com/neuron/abstract/S0896-6273(00)81027-2.

Gilad Silberberg and Henry Markram. Disynaptic inhibition between neocortical pyramidal cells mediated by Martinotti cells. *Neuron*, 53(5):735–746, March 2007. ISSN 0896-6273. doi: 10.1016/j.neuron.2007.02.012.

R. Angus Silver, Joachim Lubke, Bert Sakmann, and Dirk Feldmeyer. High-probability uniquantal transmission at excitatory synapses in barrel cortex. *Science (New York, N.Y.)*, 302(5652):1981–1984, December 2003. ISSN 1095-9203. doi: 10.1126/science.1087160.

Christopher R L Simkus and Christian Stricker. Properties of mEPSCs recorded in layer II neurones of rat barrel cortex. *The Journal of Physiology*, 545(Pt 2):509–520, December 2002. ISSN 0022-3751. doi: 10.1113/jphysiol.2002.022095. URL https://www.ncbi.nlm.nih.gov/pmc/articles/PMC2290708/.

Daniel J. Simons, Dianne Durham, and Thomas A. Woolsey. Functional Organization of Mouse and Rat SmI Barrel Cortex following Vibrissal Damage on Different Postnatal Days. *Somatosensory Research*, 1(3):207–245, January 1984. ISSN 0736-7244. doi: 10.3109/07367228409144548. URL https://doi.org/10.3109/07367228409144548.

Joseph Sirosh and Risto Miikkulainen. Cooperative self-organization of afferent and lateral connections in cortical maps. *Biological Cybernetics*, 71(1):65–78, May 1994. ISSN 1432-0770. doi: 10.1007/BF00198912. URL https://doi.org/10.1007/BF00198912.

Anton Sirota, Jozsef Csicsvari, Derek Buhl, and György Buzsáki. Communication between neocortex and hippocampus during sleep in rodents. *Proceedings of the National Academy of Sciences*, 100(4):2065–2069, February 2003. ISSN 0027-8424, 1091-6490. doi: 10.1073/pnas.0437938100. URL https://www.pnas.org/content/100/4/2065.

Yiu Fai Sit and Risto Miikkulainen. A computational model of the signals in optical imaging with voltage-sensitive dyes. *Neurocomputing*, 70(10):1853–1857, June 2007. ISSN 0925-2312. doi: 10.1016/j.neucom.2006.10.089. URL http://www.sciencedirect.com/science/article/pii/S0925231206003833.

P. Somogyi. A specific 'axo-axonal' interneuron in the visual cortex of the rat. *Brain Research*, 136(2):345–350, November 1977. ISSN 0006-8993. doi: 10.1016/0006-8993(77)90808-3. URL http://www.sciencedirect.com/science/article/pii/0006899377908083.

M Steriade. Corticothalamic resonance, states of vigilance and mentation. *Neuroscience*, 101 (2):243–276, November 2000. ISSN 0306-4522. doi: 10.1016/S0306-4522(00)00353-5. URL http://www.sciencedirect.com/science/article/pii/S0306452200003535.

M. Steriade, D. A. McCormick, and T. J. Sejnowski. Thalamocortical oscillations in the sleeping and aroused brain. *Science*, 262(5134):679–685, October 1993a. ISSN 0036-8075, 1095-9203. doi: 10.1126/science.8235588. URL http://science.sciencemag.org/content/262/5134/679.

M. Steriade, A. Nunez, and F. Amzica. A novel slow (< 1 Hz) oscillation of neocortical neurons in vivo: depolarizing and hyperpolarizing components. *Journal of Neuroscience*, 13(8):3252–3265, August 1993b. ISSN 0270-6474, 1529-2401. doi: 10.1523/JNEUROSCI.13-08-03252. 1993. URL https://www.jneurosci.org/content/13/8/3252.

Greg J. Stuart and Bert Sakmann. Active propagation of somatic action potentials into neocortical pyramidal cell dendrites. *Nature*, 367(6458):69–72, January 1994. ISSN 1476-4687. doi: 10.1038/367069a0. URL https://www.nature.com/articles/367069a0.

Adriana Taddeucci, Fabrizio Martelli, Marco Barilli, Marco Ferrari, and Giovanni Zaccanti. Optical properties of brain tissue. *Journal of Biomedical Optics*, 1(1):117–123, 1996. ISSN 1083-3668. doi: 10.1117/12.227816. URL http://dx.doi.org/10.1117/12.227816.

I. Tasaki, A. Watanabe, R. Sandlin, and L. Carnay. Changes in fluorescence, turbidity, and birefringence associated with nerve excitation. *Proceedings of the National Academy of Sciences of the United States of America*, 61(3):883, November 1968. doi: 10.1073/pnas.61.3. 883. URL https://www.ncbi.nlm.nih.gov/pmc/articles/PMC305410/.

Kate Teffer and Katerina Semendeferi. Chapter 9 - Human prefrontal cortex: Evolution, development, and pathology. In Michel A. Hofman and Dean Falk, editors, *Progress in Brain Research*, volume 195 of *Evolution of the Primate Brain*, pages 191–218. Elsevier, January 2012. doi: 10.1016/B978-0-444-53860-4.00009-X. URL http://www.sciencedirect.com/science/article/pii/B978044453860400009X.

I. Timofeev, F. Grenier, M. Bazhenov, T. J. Sejnowski, and M. Steriade. Origin of Slow Cortical Oscillations in Deafferented Cortical Slabs. *Cerebral Cortex*, 10(12):1185–1199, December 2000. ISSN 1047-3211. doi: 10.1093/cercor/10.12.1185. URL https://academic.oup.com/cercor/article/10/12/1185/314379.

Bibliography

Giulio Srubek Tomassy, Daniel R. Berger, Hsu-Hsin Chen, Narayanan Kasthuri, Kenneth J. Hayworth, Alessandro Vercelli, H. Sebastian Seung, Jeff W. Lichtman, and Paola Arlotta. Distinct profiles of myelin distribution along single axons of pyramidal neurons in the neocortex. *Science (New York, N.Y.)*, 344(6181):319–324, April 2014. ISSN 0036-8075. doi: 10.1126/science.1249766. URL https://www.ncbi.nlm.nih.gov/pmc/articles/PMC4122120/.

Ryohei Tomioka, Keiko Okamoto, Takahiro Furuta, Fumino Fujiyama, Takuji Iwasato, Yuchio Yanagawa, Kunihiko Obata, Takeshi Kaneko, and Nobuaki Tamamaki. Demonstration of long-range GABAergic connections distributed throughout the mouse neocortex. *European Journal of Neuroscience*, 21(6):1587–1600, 2005. ISSN 1460-9568. doi: 10.1111/j.1460-9568.2005.03989.x. URL https://onlinelibrary.wiley.com/doi/abs/10.1111/j.1460-9568.2005.03989.x.

Alexandra Tran-Van-Minh, Romain D. Cazé, Therése Abrahamsson, Laurence Cathala, Boris S. Gutkin, and David A. DiGregorio. Contribution of sublinear and supralinear dendritic integration to neuronal computations. *Frontiers in Cellular Neuroscience*, 9, 2015. ISSN 1662-5102. doi: 10.3389/fncel.2015.00067. URL https://www.frontiersin.org/articles/10.3389/fncel.2015.00067/full.

Yang Tsau, Peter Wenner, Michael J. O'Donovan, Lawrence B. Cohen, Leslie M. Loew, and Joseph P. Wuskell. Dye screening and signal-to-noise ratio for retrogradely transported voltage-sensitive dyes. *Journal of Neuroscience Methods*, 70(2):121–129, December 1996. ISSN 0165-0270. doi: 10.1016/S0165-0270(96)00109-4. URL http://www.sciencedirect.com/science/article/pii/S0165027096001094.

D. Y. Ts'o, R. D. Frostig, E. E. Lieke, and A. Grinvald. Functional organization of primate visual cortex revealed by high resolution optical imaging. *Science*, 249(4967):417–420, July 1990. ISSN 0036-8075, 1095-9203. doi: 10.1126/science.2165630. URL https://science.sciencemag.org/content/249/4967/417.

M. Tsodyks, T. Kenet, A. Grinvald, and A. Arieli. Linking Spontaneous Activity of Single Cortical Neurons and the Underlying Functional Architecture. *Science*, 286(5446):1943–1946, December 1999. ISSN 0036-8075, 1095-9203. doi: 10.1126/science.286.5446.1943. URL https://science.sciencemag.org/content/286/5446/1943.

M. V. Tsodyks and H. Markram. The neural code between neocortical pyramidal neurons depends on neurotransmitter release probability. *Proceedings of the National Academy of Sciences of the United States of America*, 94(2):719–723, January 1997. ISSN 0027-8424. doi: 10.1073/pnas.94.2.719.

Yun Wang, Anirudh Gupta, Maria Toledo-Rodriguez, Cai Zhi Wu, and Henry Markram. Anatomical, physiological, molecular and circuit properties of nest basket cells in the developing somatosensory cortex. *Cerebral Cortex (New York, N.Y.: 1991)*, 12(4):395–410, April 2002. ISSN 1047-3211. doi: 10.1093/cercor/12.4.395.

Anne E. West and Michael E. Greenberg. Neuronal Activity–Regulated Gene Transcription in Synapse Development and Cognitive Function. *Cold Spring Harbor Perspectives in Biology*, 3(6), June 2011. ISSN 1943-0264. doi: 10.1101/cshperspect.a005744. URL https://www.ncbi.nlm.nih.gov/pmc/articles/PMC3098681/.

Martin Wilson. Microscope Resolution: Concepts, Factors and Calculation. December 2016. URL https://www.leica-microsystems.com/science-lab/microscope-resolution-concepts-factors-and-calculation/.

Alan R. Woodruff, Stewart A. Anderson, and Rafael Yuste. The Enigmatic Function of Chandelier Cells. *Front. Neurosci.*, 4, 2010. ISSN 1662-453X. doi: 10.3389/fnins.2010.00201. URL https://www.frontiersin.org/articles/10.3389/fnins.2010.00201/full.

Dajun Xing, Chun-I. Yeh, and Robert M. Shapley. Spatial Spread of the Local Field Potential and its Laminar Variation in Visual Cortex. *Journal of Neuroscience*, 29(37):11540–11549, September 2009. ISSN 0270-6474, 1529-2401. doi: 10.1523/JNEUROSCI.2573-09.2009. URL http://www.jneurosci.org/content/29/37/11540.

A. N. Yaroslavsky, P. C. Schulze, I. V. Yaroslavsky, R. Schober, F. Ulrich, and H. J. Schwarzmaier. Optical properties of selected native and coagulated human brain tissues in vitro in the visible and near infrared spectral range. *Physics in Medicine and Biology*, 47(12):2059–2073, June 2002. ISSN 0031-9155.

Yann Zerlaut, Sandrine Chemla, Frederic Chavane, and Alain Destexhe. Modeling mesoscopic cortical dynamics using a mean-field model of conductance-based networks of adaptive exponential integrate-and-fire neurons. *Journal of Computational Neuroscience*, 44(1): 45–61, February 2018. ISSN 1573-6873. doi: 10.1007/s10827-017-0668-2. URL https://doi.org/10.1007/s10827-017-0668-2.

Shanglin Zhou and Yuguo Yu. Synaptic E-I Balance Underlies Efficient Neural Coding. *Frontiers in Neuroscience*, 12, 2018. ISSN 1662-453X. doi: 10.3389/fnins.2018.00046. URL https://www.frontiersin.org/articles/10.3389/fnins.2018.00046/full.

Wen-Liang Zhou, Ping Yan, Joseph P. Wuskell, Leslie M. Loew, and Srdjan D. Antic. Intracellular long-wavelength voltage-sensitive dyes for studying the dynamics of action potentials in axons and thin dendrites. *Journal of Neuroscience Methods*, 164(2):225–239, August 2007. ISSN 0165-0270. doi: 10.1016/j.jneumeth.2007.05.002. URL http://www.sciencedirect.com/science/article/pii/S0165027007002105.

Taylor H. **Newton**

Doctoral Student

Address Campus Biotech, Chemin Des Mines 9, Geneva

1202, Switzerland

Phone 41216937119

E-mail taylor.newton@epfl.ch

Seeking to understand the organizing principles of cortical information processing through any means possible.

Skills

Large-scale Simulation
Experiment Design
Statistics & Data Analysis
Scientific Programming
Unix Based Systems
Scientific Writing

Work History

2014-11 - 2019-11

Doctoral Student

Blue Brain Project | EPFL, Geneva, GE, Switzerland
- Ran and analyzed large-scale biophysically detailed simulations of voltage-sensitive dye imaging in a model of neocortical microcircuitry to interrogate the spatiotemporal dynamics of neural computations.
- Supervised master's student project on mean field modeling of cortical populations.
- Teaching assistant: "Analyse Numérique", "Pattern Classification and Machine Learning".

2012-09 - 2014-08

Doctoral Student

Multi-Scale Robotics Lab | ETHZ, Zürich, ZH, Switzerland
- Investigated hybrid magnetic and mechanical systems for the automated guidance of intravascular cerebral catheters with visual feedback.
- Designed and performed experiments demonstrating control of a catheter in a vascular phantom using a remotely controlled magnetic manipulation system and motorized catheter advancer.
- Teaching assistant: "Theory of Robotics & Mechatronics".

2012-06 - 2012-08

Web Development Intern

MuleSoft, San Francisco, CA, USA
- Created scripts for automating the process of launching Amazon Elastic Compute cloud (EC2) instances into a Virtual Private Cloud (VPC) network (Python).

97

2011-09 - 2012-06

Research Assistant

CHARM Lab | Stanford University, Stanford, CA, USA

- Optimized morphology of slip detection sensors in a robotic grasping system using evolutionary algorithms (MATLAB).

2011-06 - 2011-08	**Mechanical Engineering Intern**

Lam Research Center, Fremont, CA, USA

- Designed and constructed a portable plasma ignition chamber for use in wafer etching, including detailed CAD models of chamber, RF matching network and vacuum pump assembly (NX Siemens PLM Software).

2011-02 - 2011-06	**Research Assistant**

Artificial Intelligence Lab | Stanford University, Stanford, CA, USA

- Performed dynamic parameter identification of a KUKA industrial serial manipulator (MATLAB).
- Implemented Kalman filter for estimation of mass matrix inertial parameters in a robotic arm (MATLAB).

2008-08 - 2010-08	**Assistant Language Teacher**

Sendai City Board Of Education, Sendai, Japan

- Assisted the instruction of English as a second language (ESL) at middle and elementary schools.
- Helped to develop age-specific ESL syllabi tailored to Japanese foreign language proficiency requirements.
- Organized extracurricular events promoting cultural exchange.

Education

2014-11 - 2019-11	**PhD: Neuroscience (with distinction)**

Swiss Federal Institute of Technology Lausanne (EPFL) - Lausanne, Switzerland

2012-09 - 2014-08	**PhD: Mechanical Engineering (unfinished)**

Swiss Federal Institute of Technology Zurich - Zürich, Switzerland

2010-09 - 2012-06	**Master of Science: Mechanical Engineering**

Stanford University - Stanford, CA

2004-09 - 2008-05	**Bachelor of Science: Physics/Mathematics**

Brown University - Providence, RI

Software

Python, MATLAB, C++

Languages

English, Japanese, German, French

Awards & Honors

98

Invited speaker: Donders Discussions, Nijmegen, Netherlands | *2018*
Best Poster: CNS, Seattle, WA, USA | *2018*
Best Speaker: ENCODS, Berlin, Germany | *2018*

Conferences & Events

Society for Neuroscience (SfN) Annual Meeting, San Diego, CA, USA | *2018*

The Donders Discussions, Nijmegen, Netherlands | *2018*

Computational Neuroscience (CNS) Meeting, Seattle, WA, USA | *2018*

European Neuroscience Conference by Doctoral Students (ENCODS), Berlin, Germany | *2018*

Society for Neuroscience (SfN) Annual Meeting, San Diego, CA, USA | *2016*

Novartis International Biotechnology Leadership Camp, Basel, Swizterland | *2016*
- Worked on a team to develop a business plan and marketing strategy for a pharmaceutical industry case study.

Lemanic Neuroscience Annual Meeting, Les Diablerets, Switzerland | *2016*
- Helped to organize and host conference.
- Gave talk on modeling voltage-sensitive dye imaging.

Summer Workshop on the Dynamic Brain, Friday Harbor, Washington, USA | *2015*
- Worked on a team to create software for analyzing correlations in *in vivo* two-photon calcium imaging datasets (Python).

Publications

Newton, T. H., Abdellah, M., Chevtchenko, G., Muller, E. B. & Markram, H. Voltage-sensitive dye imaging reveals inhibitory modulation of ongoing cortical activity. bioRxiv 812008 (2019) doi:10.1101/812008.

Walker, R., Eriksson, A., Ruiz, C., Newton, T. H. & Casalegno, F. Epidemiology of human culture: parietal rock art requires high population density. bioRxiv 705137 (2019) doi:10.1101/705137.

Casalegno, F. et al. Caries Detection with Near-Infrared Transillumination Using Deep Learning. J Dent Res 98, 1227–1233 (2019).

Rössert, C. et al. Automated point-neuron simplification of data-driven microcircuit models. arXiv:1604.00087 [q-bio] (2016).

Markram, H. et al. Reconstruction and Simulation of Neocortical Microcircuitry. Cell 163, 456–492 (2015).

Jang, B. et al. Undulatory Locomotion of Magnetic Multilink Nanoswimmers. Nano Lett. 15, 4829–4833 (2015).

Damian, D. D., Newton, T. H., Pfeifer, R. & Okamura, A. M. Artificial Tactile Sensing of Position and Slip Speed by Exploiting Geometrical Features. IEEE/ASME Transactions on Mechatronics 20, 263–274 (2015).

Newton, T. H. & Spradlin, M. Quite a character: The spectrum of Yang–Mills on. Physics Letters B 672, 382–385 (2009).